

**OPTICAL INVESTIGATIONS OF NANOSTRUCTURED
OXIDES AND SEMICONDUCTORS**

by

Patrick Richard Irvin

M.S., University of Pittsburgh, 2005

B.S., University of Pittsburgh, 2003

Submitted to the Graduate Faculty of
the School of Arts and Sciences in partial fulfillment
of the requirements for the degree of
Doctor of Philosophy

University of Pittsburgh

2009

UNIVERSITY OF PITTSBURGH
SCHOOL OF ARTS AND SCIENCES

This dissertation was presented

by

Patrick Richard Irvin

It was defended on

November 16, 2009

and approved by

Jeremy Levy, Professor, Department of Physics and Astronomy

D. John Hillier, Professor, Department of Physics and Astronomy

Hrvoje Petek, Professor, Department of Physics and Astronomy

Chandralekha Singh, Associate Professor, Department of Physics and Astronomy

Kevin Chen, Associate Professor, Department of Electrical and Computer Engineering

Dissertation Director: Jeremy Levy, Professor, Department of Physics and Astronomy

Copyright © by Patrick Richard Irvin
2009

OPTICAL INVESTIGATIONS OF NANOSTRUCTURED OXIDES AND SEMICONDUCTORS

Patrick R. Irvin, PhD

University of Pittsburgh, 2009

This work is motivated by the prospect of building a quantum computer: a device that would allow physicists to explore quantum mechanics more deeply, and allow everyone else to keep their credit card numbers safe on the internet. In this thesis we explore two classes of materials that are relevant to a proposed quantum computer architecture: oxides and semiconductors.

Systems with a ferroelectric to paraelectric transition in the vicinity of room temperature are useful for devices. We investigate strained-SrTiO₃, which is ferroelectric at room-temperature, and a composite material of (Ba,Sr)TiO₃ and MgO.

We present optical techniques to measure electron spin dynamics with GHz dynamical bandwidth, transform-limited spectral selectivity, and phase-sensitive detection. We demonstrate this technique by measuring GHz-spin precession in *n*-GaAs. We also describe our efforts to optically probe InAs/GaAs and GaAs/AlGaAs quantum dots.

Nanoscale devices with photonic properties have been the subject of intense research over the past decade. Potential nanophotonic applications include communications, polarization-sensitive detectors, and solar power generation. Here we show photosensitivity of a nanoscale detector written at the interface between two oxides.

TABLE OF CONTENTS

PREFACE	xii
1.0 INTRODUCTION	1
1.1 Quantum Information Processing and Quantum Computing	1
1.2 Physical Realization of a Quantum Computer	6
1.2.1 Ions	6
1.2.2 NMR	9
1.3 COSMQC	10
1.4 Materials	12
1.4.1 Ferroelectrics	13
1.4.2 Oxide Heterostructures	17
1.4.3 Quantum Dots	18
1.5 Content Summary	20
2.0 EXPERIMENTAL METHODS	22
2.1 Electro-Optic Effect	22
2.1.1 Confocal Scanning Optical Microscopy	24
2.1.2 Time-Resolved CSOM	26
2.1.3 Spectroscopic Time-Resolved CSOM	27
2.2 Second Harmonic Generation	27
2.2.1 Second-Harmonic CSOM	30
2.3 Optical Selection Rules	30
2.4 Faraday Rotation	34
2.4.1 GHz Optical Spin Transceiver	38

2.5	Photoluminescence	40
2.6	Photoconductivity	41
3.0	ROOM TEMPERATURE FERROELECTRICITY IN STRAINED STO	43
3.1	Introduction	43
3.2	Sample Growth and Characterization	46
3.3	CSOM measurements	50
3.4	Conclusions	52
4.0	LOCALIZED MICROWAVE RESONANCES IN STRAINED STO	53
4.1	Introduction	53
4.2	Spectroscopic Microwave CSOM	54
4.3	Data Analysis	56
4.4	Conclusions	58
5.0	THREE-DIMENSIONAL POLARIZATION IMAGING OF BST:MGO	62
5.1	Introduction	62
5.2	Second-harmonic CSOM	63
5.3	Conclusions	68
6.0	GIGAHERTZ OPTICAL SPIN TRANSCEIVER (GHOST)	71
6.1	Introduction	71
6.2	Experimental set-up	73
6.3	Digital signal processing	75
6.4	Experimental results	77
6.5	Discussion	80
6.6	Conclusions	82
7.0	TOWARDS SINGLE SPIN DETECTION IN SEMICONDUCTORS	83
7.1	Indium Arsenide quantum dots	83
7.2	Gallium Arsenide quantum dots	88
7.3	Conclusions	97
8.0	A REWRITABLE NANOSCALE OXIDE PHOTODETECTOR	99
8.1	Introduction	99
8.2	Characterization	102

8.3 Conclusion	107
9.0 SUMMARY AND FUTURE OUTLOOK	109
9.1 Ferroelectrics	109
9.2 Quantum Dots	110
9.3 Oxide Interfaces	111
APPENDIX A. IMAGE ALIGNMENT	112
A.1 Image Alignment Source Code	112
A.1.1 ImageAlignment_with_ImageJ.vi	112
APPENDIX B. GHOST SOFTWARE	116
B.1 GHOST LabVIEW Source Code	116
B.1.1 _GHOST2.0__.vi	116
B.1.2 Multiply in Sine in Steps 2.0.vi	117
APPENDIX C. CRYOSTATS	120
C.1 Janis Magneto-Optical Cryostat	120
C.1.1 Cooldown	123
C.1.2 Sample exchange	123
C.2 Janis Continuous Flow Cryostat	125
BIBLIOGRAPHY	128

LIST OF TABLES

1.1 Quantum computing road map	7
6.1 Kerr rotation noise summary	81

LIST OF FIGURES

1.1	COSMQC architecture	10
1.2	COSMQC materials	11
1.3	Perovskite structure and Gibbs free energy	14
1.4	Types of quantum dots	19
2.1	Confocal scanning optical microscopy	24
2.2	Stop-motion photography	26
2.3	Second harmonic microscope	29
2.4	GaAs lattice	31
2.5	GaAs band diagram	31
2.6	Optical orientation	34
3.1	Shift of T_C with biaxial in-plane strain of strained SrTiO ₃	45
3.2	Contrast of in-plane ϵ_r and $\tan \delta$ of strained SrTiO ₃	48
3.3	In-plane dielectric constant versus bias voltage of strained SrTiO ₃	49
3.4	STO/DSC thickness dependence	50
3.5	Optical studies of strained SrTiO ₃	51
4.1	Diagram of TR-CSOM experiment	55
4.2	Phase of ferroelectric response	57
4.3	Vector plots of magnitude and phase	59
4.4	In- and out-of-phase components of ferroelectric response	60
5.1	SEM and EDS of (Ba,Sr)TiO ₃ :MgO composite	65
5.2	Diagram of SH-CSOM	66
5.3	SH-CSOM of (Ba,Sr)TiO ₃ :MgO composite	67

5.4	Diagram of TR-CSOM	68
5.5	TR-CSOM of (Ba,Sr)TiO ₃ :MgO composite	69
6.1	Simulation of GHOST noise reduction	73
6.2	Schematic drawing of GHOST experiment	74
6.3	GHOST data processing	76
6.4	KR versus time and magnetic field	79
6.5	KR showing RSA	80
6.6	Kerr rotation versus number of spins	82
7.1	InAs quantum dots in cavity sample	85
7.2	Photoluminescence and transmission of InAs quantum dots in cavity	85
7.3	Anneal InAs quantum dots	87
7.4	InAs quantum dots with apertures	87
7.5	InAs quantum dots photocurrent	88
7.6	GaAs quantum dot sample	89
7.7	GaAs quantum dot with apertures	90
7.8	Quantum dot search	91
7.9	Photoluminescence versus V_{DC}	93
7.10	Photoluminescence versus V_{AC}	94
7.11	Stark shift modulation absorption	95
7.12	Stark shift modulation absorption images	96
7.13	Solid immersion lens	96
8.1	LaAlO ₃ /SrTiO ₃ : diagram and demonstration of optical sensitivity	100
8.2	Tuning of photoconductivity	103
8.3	Wavelength and power dependence	104
8.4	Wire width	107
8.5	Photocurrent response versus time	108
8.6	Tuning the photoconductivity in the near-infrared	108
A1	TRCSOM analysis	113
A2	CSOM to Tiff	114
A3	ImageJ	114

A4	CSOM alignment	115
B1	GHOST code	118
B2	Multiply by Sine in Steps 2.0.vi	119
C1	Cryostats photo	121
C2	Magneto-optical cryostat	122
C3	Continuous flow cryostat	126

PREFACE

This dissertation is the culmination of many years of work and results from the efforts of a number of people. I wouldn't have made it this far without a great deal of support from my colleagues, friends, and family.

First of all, my advisor, Jeremy, has been nothing but supportive during my time here. I want to thank him for giving me a chance to work in his lab and for giving me the opportunity to work on such a diverse set of projects. His tireless enthusiasm has made the lab what it is today. I would also like to express my gratitude to my committee, Kevin Chen, John Hillier, Hrvoje Petek, and Chandralekha Singh, whose commitment and guidance have helped me to improve this dissertation.

Present and former labmates, of which there are many, have all contributed either directly or indirectly to this work and to my growth as a scientist. Chris Butler, Nitin Patil, and Henry Zhu were always available to help when I started in the lab, even pausing to help me distinguish my samples from the dirt on the floor. Vanita Srinivasa has deepened my understanding of quantum computing. Guanglei Cheng has always been kind to watch over my experiments when needed. Cheng Cen and Daniela Bogorin have done a fantastic job of creating oxide nanodevices for us. Hounghzhou Ma never tired of my questions about Chinese cuisine and Sang-Kee Eah made sure everything was labeled. My work on ferroelectrics was built upon the foundation laid down by Charlie Hubert. I worked closely with Peti Fodor on the spins in semiconductor measurements; from him I learned much about cryogenics, patience, and the finer points of Le Tour. More recently, Yan Ma has contributed to the work on the FPGA GHOST, quantum dots, and oxide photodetectors.

We don't grow samples, and therefore we rely on the expertise of our collaborators: Darrell Schlom, Amar Bhalla, David Awschalom, Gilberto Medeiros Ribeiro, and Chang-Beom Eom have all contributed samples on which we obtained the results presented here. Obrigado aos meus

colegas do Brasil, Thiago Alegre e Gilberto Medeiros Ribeiro. Eles me ajudaram com os meus experimentos em Pittsburgh e no Brasil, e para não mencionar com o meu Português. Thanks also to my gracious hosts at UCSB: David Awschalom, Jesse Berezovsky, and Maiken Mikkelsen.

The staff in the physics office has helped me in countless ways. Thanks to Bob Giles, Ken Petrocelli, and Kevin Kotek for running and maintaining the machine shop, without which many of these experiments would not have been possible. Carl Weisdack has always made sure to keep the vendors in line and get us what we needed on time. And thanks to Jim Stango for never being afraid to lend us some obscure piece of equipment and then allowing us to keep it long after we've forgotten where it even came from.

I've been blessed with many friends, both old and new, who have been a source of distraction, commiseration, encouragement, and inspiration. A very special thanks to mom and dad and the rest of my family for their constant love, support, and encouragement from the very beginning. My son, Nathan, provided countless hours of fun at the end of a long day at the lab and *he* was always excited to hear when I rode the bus home. Finally, but certainly not least, my wife, Julie, has encouraged and supported me throughout my academic journey, which began with me getting serious about my studies in high school. While I'm not sure she understands what I do now, she was a source of inspiration for me to pursue a career in science in the first place.

Financial support has been generously provided by the National Science Foundation with grants DMR-0103354, DMR-0333192, DMR-0602846, and DMR-0704022; the Department of Energy; DARPA QuIST through contract DAAD19-01-1-0650; and by the University of Pittsburgh through a one-year fellowship.

1.0 INTRODUCTION

The motivation for this thesis, in other words, the glue that holds it together, is quantum information processing. Quantum information processing, and its more specific incarnations as quantum communication and quantum computing, date to proposals by Feynman [1] and Deutsch [2] in the early-1980s. Just as quantum mechanics provides a more complete description of the world than Newtonian mechanics does, they believed that a quantum system could become a more complete (and more powerful) computer.

1.1 QUANTUM INFORMATION PROCESSING AND QUANTUM COMPUTING

The fundamental unit of classical information is the bit, which can take on two values: 0 or 1. A quantum bit (qubit¹), on the other hand, is a vector with basis elements $|0\rangle$ or $|1\rangle$. A qubit can then be expressed as a superposition of $|0\rangle$ and $|1\rangle$:

$$|\psi\rangle = a|0\rangle + b|1\rangle, \quad (1.1)$$

where a and b are complex numbers such that

$$|a|^2 + |b|^2 = 1. \quad (1.2)$$

A measurement of $|\psi\rangle$ will yield $|0\rangle$ with probability $|a|^2$ and $|1\rangle$ with probability $|b|^2$.

¹Qubit is a homophone of cubit. For a discussion of alternate spelling, see N. David Mermin's articles in *Physics Today* (April 2007, p. 8; October 2007, p. 10)

If we have N qubits then they will exist in a Hilbert space of 2^N dimensions. For two qubits we have a 2^2 -dimensional vector,

$$|\psi\rangle = a_0 |00\rangle + a_1 |01\rangle + a_2 |10\rangle + a_3 |11\rangle. \quad (1.3)$$

More generally in N dimensions we have the superposition state

$$|\psi\rangle = \sum_{i=0}^{2^N-1} a_i |i\rangle. \quad (1.4)$$

Here $|i\rangle$ represents a state of N qubits given by a binary number corresponding to i .² We also have the normalization condition

$$\sum_{i=0}^{2^N-1} |a_i|^2 = 1. \quad (1.5)$$

The probability of measuring $|i\rangle$ is $|a_i|^2$ if we measure all N qubits.

In order to realize a quantum computer, DiVincenzo describes five requirements that must be fulfilled [3]. We must have:

1. “well-characterized” qubits in a scalable physical system,
2. the ability to initialize to a known state (such as $|\psi_0\rangle = |00 \cdots 0\rangle$),
3. a decoherence time of the qubit that is much longer than the gate time,
4. a universal set of quantum gates, and
5. the ability to measure the state of specific qubits.

Having well-characterized qubits means understanding the environment in which they reside. We must know how a qubit couples to external fields and how it interacts with its neighboring qubits, all of which is important to know in order to manipulate the qubits during initialization and for constructing quantum gates. Not all physical systems possess the same interactions: in each proposed physical system one must specify how the interactions are used to construct the quantum gates. For example, in quantum dots the only two-body interaction available is exchange between neighboring spins, and in NMR there are interactions which cannot be turned off. The decoherence time of a qubit is an indication of how it interacts with its environment. DiVincenzo points out that we need to only worry about the relevant decoherence times. For example, we can ignore orbital decoherence if we encode the qubit using spin angular momentum. Analysis in the context

²For example, in 2^2 dimensions $|i = 2\rangle = |10\rangle$.

of quantum error correction (discussed later) has shown that the execution time for a single gate should be 10^{-5} to 10^{-4} times the decoherence time [4]. In order to create a *universal* quantum gate it has been shown that all that is needed are single-qubit operations combined with a two-qubit operation such as controlled-NOT (“CNOT”) [5] or square-root swap (“ $\sqrt{\text{SWAP}}$ ”) [6, 7].

While giving the experimentalist specific goals to keep in mind, DiVincenzo’s five requirements also suggest how a quantum computation would proceed. First, we gather our qubits (all N of them) and initialize to $|\psi_0\rangle$. Next we apply a unitary transformation $U(t)$ to put the system into the state $|\psi_1\rangle = U(t)|\psi_0\rangle$. Finally, we perform a measurement to project each qubit into the $\{|0\rangle, |1\rangle\}$ basis. Because of the quantum mechanical nature of the system, this is called a probabilistic algorithm, meaning we only get the “right” answer with probability $|a_i|^2$. In many cases this is OK because it is typically easy to run the computation again or to verify the result classically (as in Shor’s algorithm).

A classical computer can simulate a quantum system (after all we do have Schrödinger’s equation), but the size of the phase space grows beyond the capacity of a classical computer for even a moderate number of qubits (for $N = 100$, $2^N = 2^{100} \sim 10^{30}$). What makes a quantum computer so powerful is known as “quantum parallelism.” That is, as a result of superposition in the Hilbert space, a quantum computer acts simultaneously on the $|0\rangle$ and $|1\rangle$ states. This is the feature that made a quantum computer desirable to Feynman and Deutsch: the idea that quantum parallelism could be used to simulate a quantum system.

Up to this point, a physicist might have the idea that quantum computation is *interesting* because it is a means to learn more about quantum mechanics. Other people began to find it *useful* in 1994 when Peter Shor demonstrated an efficient quantum algorithm for factoring large numbers [8]. The assumption that to factor the product (n) of two primes (p and q) is hard is the underlying principle of the RSA cryptography system [9]. RSA is used worldwide for secure exchange of information between two parties; the information can be financial transactions between large banks or state secrets by the CIA. The mere potential of a quantum computer to break RSA encryption threatens the security backbone of the internet. Quantum computation is therefore of great interest to the Department of Defense and the National Security Agency, regardless of whether efforts to create a working quantum computer are successful or not.

A second major development that helped to show that a quantum computer is *possible* was the discovery of quantum error correction [10]. The difficulty in constructing a quantum computer is perhaps best embodied in the following quote from Asher Peres [11]: “Quantum phenomena do not occur in Hilbert space; they occur in a laboratory.” Our carefully prepared qubit state will always be in contact with its environment and it may wander away from the state that we think it is in. The interaction of a quantum system with its environment is known as decoherence and is an important concept for understanding the transition from a quantum to classical world.

A classical computer is also subject to decoherence and also requires that error correction be implemented (at least in the early days of computers). The simplest classical error correction scheme is the repetition code [12], meaning we simply make several copies of the bit:

$$\begin{aligned} 0 &\rightarrow 000 \\ 1 &\rightarrow 111 \end{aligned} \quad (1.6)$$

A single bit flip would look like the following:

$$\begin{aligned} 000 &\rightarrow 001 \\ 111 &\rightarrow 110 \end{aligned} \quad (1.7)$$

which is easily corrected by a simple majority voting. In summary

$$\begin{aligned} 0 &\rightarrow 000 \rightarrow 001 \rightarrow 0 \\ 1 &\rightarrow 111 \rightarrow 110 \rightarrow 1 \end{aligned} \quad (1.8)$$

It turns out that as long as the probability that each bit has the correct value is greater than 0.5, simple majority voting will work. This so called N -bit repetition code is far from the most efficient algorithm.

A quantum computer can also have bit-flip errors ($|0\rangle \rightarrow |1\rangle$), but it may accumulate other types of errors as well. A quantum computer can also have phase errors,

$$a|0\rangle + b|1\rangle \rightarrow a|0\rangle - b|1\rangle, \quad (1.9)$$

resulting in a state orthogonal to what we started with (for $|a| = |b|$). A third type of error that changes the normalization coefficients is known as a small-error:

$$a|0\rangle + b|1\rangle \rightarrow (a + \epsilon)|0\rangle + b|1\rangle, \quad (1.10)$$

which can become a large, significant error over time. Classical error correction has no provisions for small errors or phase errors (only large bit-flip errors). There are also fundamental reasons to prevent us from using classical error correction schemes such as the repetition scheme. The first is the need to perform a measurement without destroying the quantum information. The second is the fact that we cannot copy an unknown quantum state with perfect fidelity (due to the no-cloning theorem).

Fortunately, once again Peter Shor had been thinking very hard about quantum computation. Quantum error correction (QEC) [13] relies on quantum entanglement and measurement of specific qubits during the computation to detect and correct errors. In Shor's QEC scheme [14], encoding a qubit in a three-qubit space,

$$\begin{aligned} |\bar{0}\rangle &= |0\rangle \otimes |0\rangle \otimes |0\rangle \equiv |000\rangle \\ |\bar{1}\rangle &= |1\rangle \otimes |1\rangle \otimes |1\rangle \equiv |111\rangle \end{aligned}, \quad (1.11)$$

is sufficient to protect against bit flip errors, small errors, and furthermore avoids the measurement problem by measuring two-qubit observables. For example, by measuring the product observables $\sigma_z^{(1)} \otimes \sigma_z^{(2)}$ and $\sigma_z^{(2)} \otimes \sigma_z^{(3)}$ we can determine which of the three qubits has flipped without revealing the individual qubit values, thereby preserving the entanglement of the encoded state. The answer is readout from an introduced ancilla qubit. As we have accomplished this through qubit redundancy, we can also protect ourselves from phase errors by encoding the phase redundantly as three clusters,

$$\begin{aligned} |\bar{0}\rangle &= 2^{-3/2} ((|000\rangle + |111\rangle)(|000\rangle + |111\rangle)(|000\rangle + |111\rangle)) \\ |\bar{1}\rangle &= 2^{-3/2} ((|000\rangle - |111\rangle)(|000\rangle - |111\rangle)(|000\rangle - |111\rangle)) \end{aligned}. \quad (1.12)$$

Each cluster also has qubit redundancy. Phase errors can be corrected by measurement of the six-qubit observable $\sigma_x^{(1)} \otimes \sigma_x^{(2)} \otimes \sigma_x^{(3)} \otimes \sigma_x^{(4)} \otimes \sigma_x^{(5)} \otimes \sigma_x^{(6)}$. These sorts of multi-qubit observables can be realized through the application of a sequence of two-qubit entanglement operations [15]. Encoding quantum information plus the use of quantum entanglement can in fact achieve the goals of quantum error correction.

To be useful for factoring meaningfully large numbers (as presently used in the RSA encryption algorithm), we need on the order of *ten thousand* qubits. While this might seem like an overly difficult and unattainable goal to be able to scale to this number of qubits, the research is still in the early stages (thus it is research and not technology). On the other hand, quantum computing

research can have other ancillary benefits as well. Quantum computing has served to unite research groups across many academic disciplines including computer science, physics, and materials engineering. In 2004 [16] there were nearly 150 research groups investigating dozens of approaches to quantum computing, some of which will be discussed in §1.2.

One can also form an analogy with the space race that began in the 1960s. That also was an extremely ambitious goal (to send a person over 200,000 miles to the Moon, and back), and even if we hadn't achieved that goal we still would have benefited from the associated technological advancements. In experimental condensed matter physics we benefit quite directly from well-developed vacuum equipment and cryogenic liquids³ industries. The general public now readily uses satellite communications and navigation.⁴ Quantum computation research also has the potential to spin-off similar technological advances. Already now materials inspired by quantum computing have been created that can be used in other devices and physicists have benefited from unprecedented control over quantum systems.

1.2 PHYSICAL REALIZATION OF A QUANTUM COMPUTER

There have been many proposals and attempts at building the components of a quantum computer. These include (but are certainly not limited to) using nuclear magnetic resonance (NMR) [17], trapped ions [18], superconductors [19], nuclear spins in semiconductors [20], electron spins in semiconductors [21, 22, 23], and nitrogen vacancies in diamond [24]. Table 1.1 summarizes the achievements of several quantum computing approaches in meeting these requirements. This section will introduce what some consider to be the two most successful implementations thus far, using trapped ions and liquid NMR.

1.2.1 Ions

In an ion trap quantum computer, ions are confined in a Paul trap [25] using static and oscillating electric fields. A qubit is encoded in the ground state ($|g\rangle$) and in a long-lived excited state ($|e\rangle$) of

³Condensed gases are necessary for rocket propellant and life support in space.

⁴I will leave it to a footnote to mention the clichéd Velcro and freeze-dried ice cream.

Table 1.1: Quantum computation road map: achievements as of 2004. (Adapted from Ref. 16.)

QC approach	DiVincenzo Requirement				
	#1	#2	#3	#4	#5
NMR					
Trapped Ion					
Neutral Atom					
Cavity QED					
Optical					
Solid State					
Superconductor					

an approach has achieved proof of principle
 Legend viable approach has been proposed, but no proof of principle
 no known approach

Requirement #1 scalable physical qubits
 #2 initialization ability
 #3 qubit decoherence time > gate time
 #4 universal quantum gates
 #5 measurement capability

the ion such that we can create the superposition

$$|\psi\rangle = a|g\rangle + be^{-i\omega t}|e\rangle. \quad (1.13)$$

The excited state $|e\rangle$ is either an excited state of the ion⁵ or in a hyperfine-split ground state. The remainder of this section will focus on hyperfine qubits.

Because the hyperfine splitting is so small ($E < 1$ meV and $\lambda \sim 1$ cm) a single laser cannot be used to drive a transition. Instead, a pair of laser beams are focused on each ion. By properly tuning the energy of each laser they will excite the ion from $|g\rangle$ to a virtual state before stimulating a transition to $|e\rangle$. This procedure is essentially a stimulated Raman transition between the internal hyperfine states of the ion. By pulsing the laser and controlling its duration, we can leave the ion in a particular state, resulting in a one-qubit gate operation.

There is no direct interaction between ions to implement a two-qubit gate so the vibrational motion of the ion chain provides the basis for two-qubit gate operations [18]. Because of the Coulomb repulsion between the ions, at low enough temperatures they will vibrate in a coherent, quantized motion. We will call the ground state $|0\rangle_{cm}$ and the first excited “phonon” $|1\rangle_{cm}$. Now the state of the n^{th} ion can be described by the states

$$\begin{aligned} &|g\rangle_n |0\rangle_{cm}, \\ &|g\rangle_n |1\rangle_{cm}, \\ &|e\rangle_n |0\rangle_{cm}, \\ &|e\rangle_n |1\rangle_{cm}. \end{aligned} \quad (1.14)$$

A properly tuned laser focused on the n^{th} ion will exchange momentum with the ion and excite a “phonon” mode $|0\rangle_{cm} \rightarrow |1\rangle_{cm}$. While this laser pulse obviously did not change the internal state of the m^{th} ion, it still affected it by changing the collective motion of the ions.

Readout is performed by tuning the laser to excite from $|g\rangle$ to a short-lived excited state $|e'\rangle$, which will then emit a photon (fluoresces) before relaxing back to $|g\rangle$. Qubits initially in the $|e\rangle$ state remain dark.

The trapping of ions is a complicated experiment and the ions must be cooled to sub-microKelvin temperatures. Because of the ultralow temperatures, the main source of decoherence is heating due

⁵Known as an optical qubit, in reference to the way a laser couples to the ion.

to the trapping electrodes. The use of a vibrational state provides an additional channel for coupling to the environment. A recent experiment uses ${}^9\text{Be}^+$ ions as qubits and simultaneously trapped ${}^{24}\text{Mg}^+$ ions (for sympathetically cooling) to demonstrate all of the fundamental elements of a quantum computer [26]. In addition to using the Paul trap, ion quantum computers are being considered that trap the ions on a monolithic semiconductor chip [27, 28].

1.2.2 NMR

A nuclear magnetic resonance (NMR) quantum computer [17, 29] uses a designer molecule that contains on the order of ten “backbone” atoms, such as five ${}^{19}\text{F}$ and two ${}^{13}\text{C}$ atoms. It is on the nuclear spin of these atoms that qubits are encoded, such that

$$\begin{aligned} |\uparrow\rangle &= |0\rangle, \\ |\downarrow\rangle &= |1\rangle. \end{aligned} \tag{1.15}$$

The qubits are initialized by thermalization in an applied, constant magnetic field. A pulsed, rotating field can induce Rabi oscillations, thus providing a single qubit gate. Two-qubit operations are possible through dipole-dipole interactions between the spins and by taking advantage of the refocusing techniques available in NMR.

One cannot perform NMR on a single spin,⁶ but the sample actually contains on the order of 10^{23} molecules, each a tiny quantum computer. Because we have all of these different computers what actually gets measured is the *average* spin state. The good news is, because of this massive averaging, an NMR computer can actually operate at room-temperature. However, this also leads to serious scaling problems. Although an NMR quantum computer was the first to factor 15 into its primes ($p = 3$ and $q = 5$) using 7 qubits [31] it will be a great challenge to perform a computation with more than order 10 qubits. One reason for this is that the way in which the computer is initialized is essentially random. The number of spins that end up in the state $|0\rangle$ is proportional to 2^{-N} . Furthermore, because we are unable to measure the state of a single qubit (only the average) implementation of quantum error correction is restricted. And regarding the ~ 10 qubit limit, recall that Shor’s QEC algorithm uses 9 qubits to encode a single logical qubit.

⁶The minimum number is on the order of 10^{12} [30].

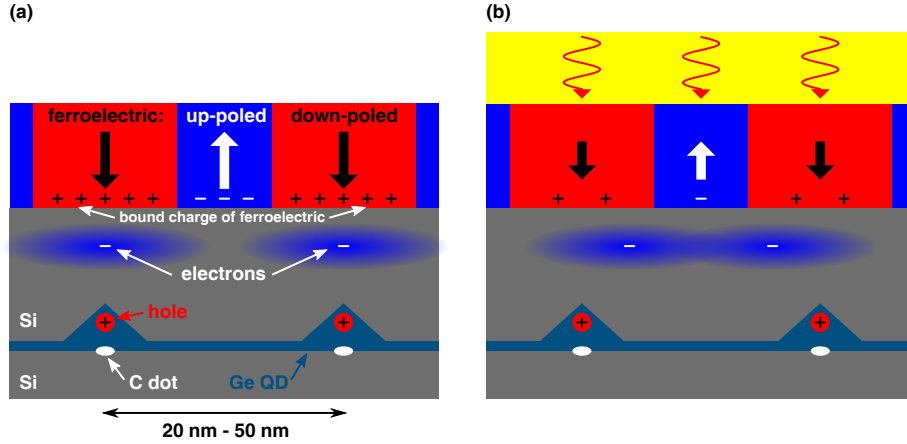


Figure 1.1: (a) Ge/Si quantum dots (QD) grown on top of a SiC nucleation site overlaid with poled-ferroelectric film. (b) a light field modulates the ferroelectric polarization which in turn controls the exchange interaction of neighboring electrons.

1.3 COSMQC

The motivation for this work is the device structure proposed by my advisor [23] and is the focus of research here at the Center for Oxide Semiconductor Materials for Quantum Computation (COSMQC). In the COSMQC architecture, shown in Figure 1.1a, a qubit is encoded by an electron spin confined in a quantum dot. A ferroelectric capping layer provides static confinement of the dots along with a means to perform gate operations between adjacent spins.

The COSMQC proposal uses Ge/Si quantum dots to confine electrons. Beginning with a Si substrate, an electron beam lithography tool can be used to deposit a carbon dot array template [32]. Figure 1.2a shows an AFM image of C dots. The substrate is annealed to form SiC dots, which then act as nucleation sites for Ge growth [33, 34]. Finally, a Si capping layer is deposited over the Ge dots. Because of the Type-II band alignment between Si and Ge, the hole is strongly confined in the Ge and the electron is spatially separate and remains in the Si. This is particularly advantageous for quantum computing because of the very long spin lifetime found in Si [35]. Si has an indirect bandgap and it is therefore difficult to couple the spin-degree of freedom to optical

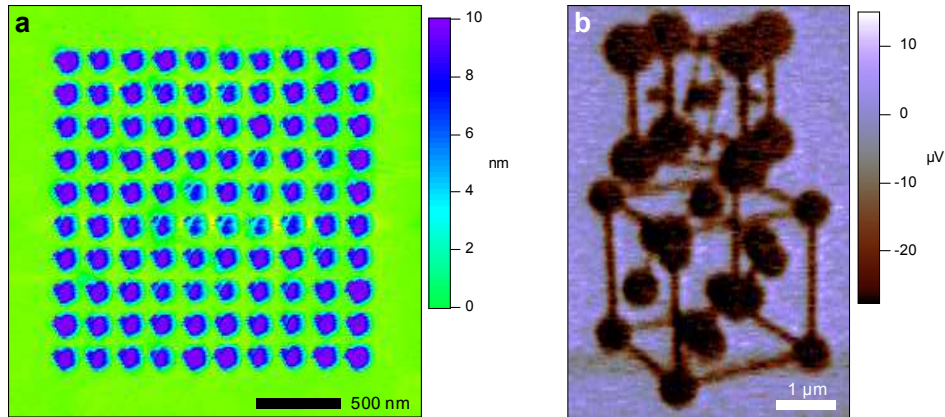


Figure 1.2: Materials important for a COSMQC quantum computer. (a) Atomic force microscope (AFM) image of C-dots patterned on Si. (b) Piezoforce microscope (PFM) image of 6 ML SrTiO₃/Si. The PFM image shows the structure of the material in which it is written. Data originally published in Reference 37.

fields. However, it has been predicted that as the size of the Ge/Si dot goes below 10 nm the quantum dots will develop a direct bandgap [36]. Ge growth on Si naturally forms dots greater than 20 nm, but the C precursor (in addition to providing templated growth) changes the growth mode such that quantum dots with size less than 10 nm form. Because of this engineered direct bandgap, a qubit can be initialized by optical pumping with a circularly polarized laser.

On top of the Si capping layer is deposited a ferroelectric film with out-of-plane (c -axis) polarization. c -axis BaTiO₃ has been grown on Si using a (Ba,Sr)TiO₃ buffer layer [38] and ferroelectric SrTiO₃ can be grown directly on Si [37]. Domains are written in the ferroelectric using an atomic force microscope (AFM) tip as shown in Figure 1.2b. The qubit electron in Si is only weakly bound to the Ge dot by the exciton binding energy and the static polarization of the ferroelectric helps to confine the electrons laterally.

Gate operations are performed by controlling the exchange interaction between neighboring spins, which is mediated by electro-optic modulation of the ferroelectric polarization. Optical rectification is a phenomenon where a non-linear polarization $P^{(2)}(t)$ is induced in a material by a

strong optical field $I_{opt}(t)$:

$$P^{(2)}(t) = \frac{rn^3}{2c}I_{opt}(t), \quad (1.16)$$

where r is the electro-optic coefficient, n is the refractive index, and c is the speed of light. When a laser pulse is focused onto the ferroelectric layer, optical rectification serves to modulate the polarization on the same time scale as the laser pulse. It is important to note that the laser modulates the polarization on the spatial scale of the patterned domains, which is much smaller than the focal spot of the laser. In this way a diffraction limited laser spot (~ 500 nm) can control the interaction between 10 nm quantum dots. Figure 1.1b shows how an appropriate ferroelectric domain poling pattern can be used to control the electrons' spacing and therefore their exchange interaction.

The Heisenberg exchange interaction between two spins, given by

$$H(t) = J(t)S_1 \cdot S_2, \quad (1.17)$$

provides the basis for two qubit operations. In the adiabatic approximation this can induce a unitary transformation of the form

$$U(t) = \exp\left(-i \int_0^T H(t)dt/\hbar\right). \quad (1.18)$$

We can define an angle ϑ such that $\vartheta = \int_0^T J(t)dt$. By varying the laser duration and intensity (see Equation 1.16) we can control the interaction strength of the qubits. For example if $\vartheta = \pi/2$ then two qubits can be entangled, which is a “ $\sqrt{\text{SWAP}}$.” $\vartheta = \pi$ is a “SWAP” operation.

The original COSMQC proposal does not specify a specific read-out scheme. It suggested an electronic method such as a single electron transistor (SET) most likely would have to be used. Recently, single spins have been measured optically with Faraday rotation [39] and this also has been a focus of our research, as described in Chapters 6 and 7. All of the optical methods mentioned have been performed on III-V semiconductors

1.4 MATERIALS

Oxides and semiconductors are integral components of our digital world. An oxide is a material with at least one oxygen atom. Oxides have many diverse properties and there are technological applications that make use of their ability to function both as insulators (SiO_2 and HfO_2 are

extremely important to the microelectronics industry for making field effect transistors) and conductors ($\text{In}_2\text{O}_3:\text{SnO}_2$ (ITO) is a *transparent* conductor used in LCD monitors and toy light sabres). In this thesis we will study oxides that are ferroelectric and oxides that are used to form a two-dimensional electron gas.

Semiconductors are materials with conductivity intermediate between insulators and conductors. Semiconductors have a bandgap in range the range of 0.5 eV to 4 eV. At absolute zero temperatures all degenerate or intrinsic semiconductors are essentially insulators. As the temperature is increased electrons may be thermally excited to partially occupy the conduction band. An important characteristic of a semiconductor is that it may be doped to have either positive or negative charge carriers. This feature is used to construct *n*- and *p*-type transistors that are then combined to form a complementary metal-oxide-semiconductor (CMOS), a fundamental component of logic gates. Semiconductors couple readily to light and are used as both photodetectors and light-emitting diodes. In this thesis we will study spins in a bulk semiconductor and study the properties of semiconductor nanostructures, known as quantum dots.

1.4.1 Ferroelectrics

Ferroelectrics are a class of materials that have a permanent electric polarization. The polarization spontaneously appears below a transition temperature known as the Curie temperature, T_C . Above T_C the material is paraelectric, meaning it only has a polarization in the presence of an electric field. In the ferroelectric phase an applied electric field can reverse the polarization direction, and in the absence of an applied electric field a remnant polarization will remain. The polarization versus electric field curve is typically hysteretic. The origin of the hysteresis is due to ferroelectric domains growing or shrinking as the electric field is swept. The paraelectric to ferroelectric phase transition is typically classified as one of two types: order-disorder or displacive. An order-disorder ferroelectric has a unit cell with a permanent, field-reversible dipole, but above T_C the dipoles become randomly oriented. In a displacive ferroelectric an ion will be displaced such that the local electric fields (due to the other ions) will be stronger than the elastic restoring forces.

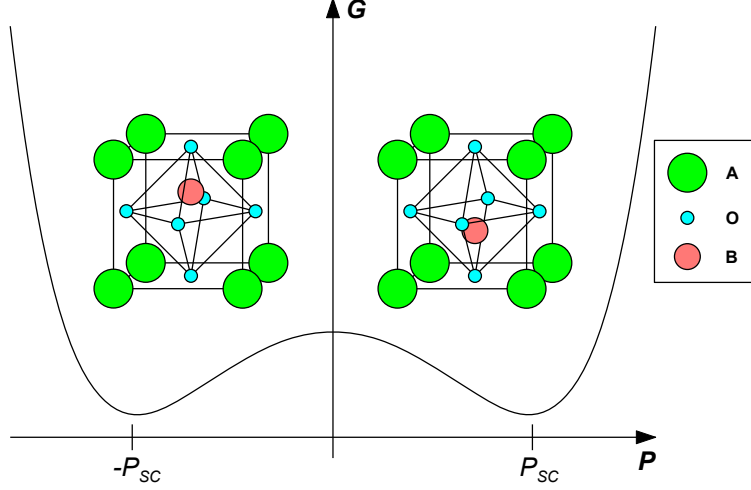


Figure 1.3: Diagram showing perovskite ABO_3 in the cubic phase. The “B” cation is schematically displaced to represent the two polarization orientations at $\pm P_{sc}$. The Gibbs free energy G is plotted as a function of polarization (See Equation 1.21).

The ferroelectrics studied in this thesis ($BaTiO_3$ and $SrTiO_3$) have the perovskite structure,⁷ which has the general chemical formula ABO_3 . The perovskite structure is cubic in the high-temperature phase, with type “A” cations on the corners, oxygen anions on the faces, and a type “B” cation at the center of the cube, as shown in Figure 1.3. $BaTiO_3$ is a displacive ferroelectric and undergoes a structural phase transition from cubic to tetragonal at ~ 393 K. In the tetragonal phase the symmetry of the crystal is lifted and the Ti^{4+} ion will find a more energetically favorable state if it is displaced from the center of the unit cell.

The ferroelectric phase transition is associated with a softening of the transverse optical mode. In the long-wavelength limit,⁸ the Lyddane-Sachs-Teller (LST) relationship [40],

$$\frac{\omega_T^2}{\omega_L^2} = \frac{\epsilon_\infty}{\epsilon_0}, \quad (1.19)$$

relates the frequencies of the transverse and longitudinal optical phonons, ω_T and ω_L , to the static dielectric constant and the dielectric constant at optical frequencies, ϵ_0 and ϵ_∞ . This relationship

⁷ named after the crystal perovskite ($CaTiO_3$)

⁸ $k \rightarrow 0$, where k is the wave vector of the phonon.

is a consequence of the nature of each type of phonon: a longitudinal optical phonon will have a polarization in the same direction as the wavevector while a transverse optical phonon will have a polarization perpendicular to the wavevector. The need for the polarizations of each type of phonon to satisfy Maxwell's equations results in the LST relation [41]. As the temperature is lowered the transverse mode softens (meaning $\omega_T \rightarrow 0$). From Equation 1.19 we see that as $\omega_T \rightarrow 0$, $\epsilon_0 \rightarrow \infty$, resulting in an instability and the crystal undergoing a structural phase transition. In a perovskite ferroelectric, this phonon mode represents the relative motion of the Ti^{4+} ion and its surrounding octahedron of O^{2-} ions [42]. As the mode softens it becomes "frozen," resulting in the transition to the ferroelectric phase.

Ginzburg-Landau theory (first developed for superconductivity) can provide a phenomenological model of the phase transition by applying principles of thermodynamic. The differential form of the Gibbs free energy of a material with cubic symmetry, subjected to stresses and electric fields, is given by [43]

$$dG = -S dT + \sum_{i=1}^3 x_i dX_i + E dP, \quad (1.20)$$

where S is entropy, T is temperature, x_i is strain, X_i is stress, and E and P are the electric field and polarization in one dimension. For zero stress and strain, we can expand G in terms of the polarization P ,

$$G = G_0 + \frac{1}{2}\alpha P^2 + \frac{1}{4}\gamma P^4 + \frac{1}{6}\delta P^6, \quad (1.21)$$

where any temperature dependence is contained in the coefficients α , γ , and δ . In the unpolarized state the crystal is centrosymmetric and therefore there are no odd powers of P .

Devonshire theory assumes that α is a linear function of temperature near T_C : $\alpha = \beta(T - T_0)$, where T_0 is known as the Curie-Weiss temperature [44]. From Equation 1.20 we can see that the electric field is equal to the differential of G with respect to P . Therefore, differentiating Equation 1.21, we find

$$\frac{\partial G}{\partial P} = E = \beta(T - T_0)P + \gamma P^3 + \delta P^5. \quad (1.22)$$

Because $P = \chi E$, we can recognize that the first coefficient is the inverse of the low-field electric susceptibility χ :

$$\chi = \frac{1}{\beta(T - T_0)}. \quad (1.23)$$

We can find the spontaneous polarization P_S by setting $E = 0$ in Equation 1.22:

$$P_S = \mp \left\{ -\frac{\gamma}{2\beta} \left[1 + \left(\frac{4\beta\delta}{\delta^2} (T - T_0) \right)^{1/2} \right] \right\}^{1/2}. \quad (1.24)$$

Finally, we can calculate the transition temperature T_C . The ferroelectric phase is stable at the minima of the Gibbs free energy. From Equation 1.21:

$$\frac{1}{2}\beta(T_C - T_0)P_{SC}^2 + \frac{1}{4}\gamma P_{SC}^4 + \frac{1}{6}\delta P_{SC}^6 = 0. \quad (1.25)$$

P_{SC} is the spontaneous polarization at T_C , which exists at $E = 0$, and therefore from Equation 1.22:

$$\beta(T - T_0)P_{SC} + \gamma P_{SC}^3 + \delta P_{SC}^5 = 0. \quad (1.26)$$

Equations 1.25 and 1.26 can then be solved for P_{SC}^2 and T_C , from which we find

$$P_{SC}^2 = -\frac{3\gamma}{4\delta}, \quad (1.27)$$

$$T_C = T_0 + \frac{3\gamma^2}{16\beta\delta}. \quad (1.28)$$

1.4.2 Oxide Heterostructures

SrTiO_3 was studied extensively in the 1950s and '60s as a potential artificial diamond substitute. The properties of SrTiO_3 are so diverse that it has been said that “if SrTiO_3 had magnetic properties, a complete study of this material would require a thorough knowledge of all of solid state physics.”⁹ In other words, it is an insulator, semiconductor, and superconductor. SrTiO_3 is a quantum paraelectric, meaning the ferroelectric phase transition would be 4 K were it not for quantum fluctuations [46]. There are ways to have it undergo a phase transition, including chemical substitution of Ba for Sr to form $\text{Ba}_x\text{Sr}_{1-x}\text{TiO}_3$, however, this method broadens the phase transition and degrades the device tunability. The ferroelectric phase transition of SrTiO_3 can be shifted to room-temperature through strain engineering by growth on a lattice-mismatched substrate such as Si [37] or DyScO_3 [47], which is the subject of Chapter 3.

SrTiO_3 , a non-polar oxide, can itself be used as a substrate for growth of LaAlO_3 , a polar oxide. As was discovered by Ohtomo and Hwang in 2004 [48], a high mobility two-dimensional electron gas (2DEG) forms at the interface of these materials. When the LaAlO_3 thickness exceeds a critical value (~ 3 unit cells) there is “polarization catastrophe” in which an electronic restructuring occurs, transferring $e/2$ charge per unit cell to the interface, resulting in the 2DEG formation. An alternative model is the creation of oxygen vacancies in the SrTiO_3 substrate during LaAlO_3 growth. This in effect dopes the SrTiO_3 near the interface and creates the high-mobility region. Atomic force microscopy has been used to probe the cross sectional resistance near the interface and has shown that the carrier density profile away from the interface (and thus the dominant mode of 2DEG formation) can vary depending on the growth conditions [49].

Thiel *et al.* [50] have demonstrated that an electric field can be used to reversibly induce the 2DEG. Also by masking the sample and selectively growing epitaxial and amorphous LaAlO_3 , the 2DEG can be laterally patterned [51]. Cheng Cen in our group has used a conducting AFM probe to pattern nanoscale devices in the interface [52, 53]. Wires with width as small as 2.1 nm have been drawn by applying a positive bias to an AFM tip in contact with the sample. By varying the magnitude of the tip bias the potential profile can be modulated. Experiments performed in vacuum demonstrate the switching performance of a transistor is not degraded after nine days. These wires

⁹Originally quoted by Marvin L. Cohen in Ref. 45.

are used as building blocks for more complicated structures like diodes and transistors. We use these patterned devices to make nanoscale photodetectors, which will be discussed in Chapter 8.

One explanation for why the AFM is able to pattern the 2DEG is that the AFM tip creates oxygen vacancies (positively charged regions) on the LaAlO_3 surface by the electrostatic removal of polar molecules (i.e. water). This results in “lateral modulation doping” and can simultaneously produce a nanoscale wire and a micrometer-wide potential profile. This picture is supported by an experiment with parallel wires in which the conductance saturates as the number of wires increases.

1.4.3 Quantum Dots

A semiconductor heterostructure can be grown such that a semiconductor with a small bandgap is sandwiched between semiconductors with a large bandgap to form a two-dimensional object known as a quantum well (see Figure 1.4a). An electron is confined, by energy, normal to the layers (z), but is free to move in the xy -plane. Further confinement in the x and y dimensions produces a quantum dot. A semiconductor quantum dot [54] is a quasi-zero-dimensional material, meaning electrons are confined in all three spatial directions.

Quantum dots can be realized in several ways. First are colloidal quantum dots that are chemically synthesized in solution [55], as shown in Figure 1.4b. These are typically formed by controllably heating and cooling a solution of nanocrystals (for example, Cd and Se or Pb and S) such that semiconductor nanocrystals (CdSe or PbS) of a desired size nucleate out of solution. While a nearly continuous energy spectrum can be created by precisely controlling the size of the nanocrystals, one disadvantage of this system is that it is challenging to make electrical contact to them.¹⁰

A second type of quantum dot is formed from a high quality GaAs/AlGaAs quantum well (Figures 1.4c and d). A 2D electron gas is formed by doping the AlGaAs layer with Si. Lateral confinement is then accomplished by etching a mesa structure [56] or by forming lateral electrodes [57] using electron beam lithography. By applying a bias to the lateral contacts, the electrons in the 2DEG are depleted, thus forming a region with a potential minimum defined by the electrodes.

¹⁰Although we did perform experiments with infrared PbS quantum dots (bought from Evident Technologies, Inc.), none of the results are presented in this thesis.

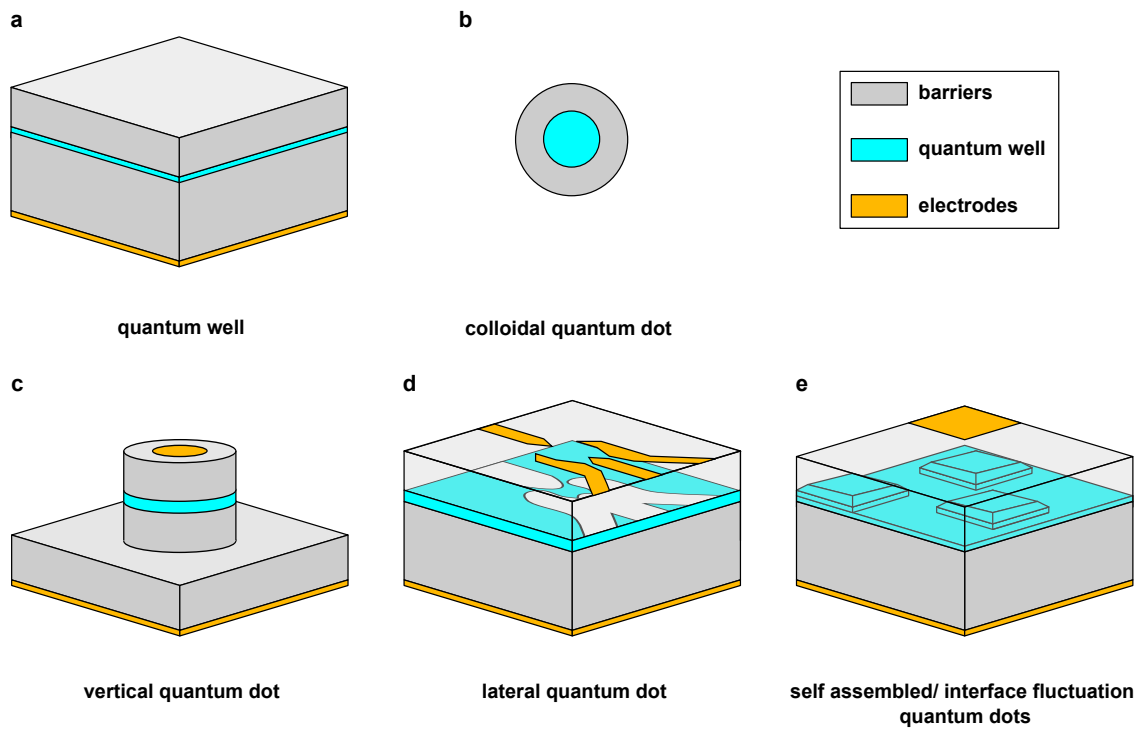


Figure 1.4: Types of quantum dots.

These types of quantum dots allow extraordinary control over the carriers and have been used to measure single spins [58] electrically.

A third type of quantum dot, represented in Figure 1.4e and which are the type studied in this thesis, are formed during growth and provide confinement based on the material structure, either (1) by interface roughness in a quantum well structure or (2) by the epitaxial layer forming islands on the substrate. The first type are known as interface fluctuation quantum dots [59, 60] and are made by pausing the growth of the quantum well material, during which time the atoms migrate to form large monolayer islands. The second type are self-assembled quantum dots, which form because of strain between the substrate and epitaxial layer. The different growth modes of self-assembled quantum dots are classified as Stranski-Krastanow (SK) or Volmer-Weber (VW). SK growth is characterized by the initial formation of a few monolayers of the epitaxial material on the substrate, which is known as the wetting layer. At some point layer growth becomes unfavorable because of strain and islands begin to form. This is considered the “normal” growth mode for hetero-epitaxial growth and is what occurs for growth of Ge on Si and InAs on GaAs. VW growth is the direct formation of islands of the epitaxial material on the substrate. This occurs because the epitaxial molecules bond more strongly to each other than the substrate. As alluded to in §1.3, SK growth of Ge on Si will produce ~20 nm dots, however if a nucleation layer of C is first deposited, Ge will grow in the VW growth mode and form dots with size <10 nm.

1.5 CONTENT SUMMARY

This chapter has described a unifying motivation for this thesis, namely quantum computation. In addition, I have discussed a specific solid state quantum computer architecture, known as COS-MQC, along with the relevant material systems. In Chapter 2 I will cover the experimental techniques used in this thesis as well as their physical origins.

As discussed previously, an oxide ferroelectric is proposed as a building block for constructing quantum gates, however, ferroelectrics can have additional applications as well. The experiments in this thesis focus on the properties of ferroelectric materials that would make them useful as components of microwave frequency devices. Chapter 3 presents the use of strain engineering to make

SrTiO₃ ferroelectric at room-temperature and Chapter 4 discusses microwave measurements on the same material. In Chapter 5 we use second harmonic generation to study a (Ba,Sr)TiO₃/MgO composite, a material that attempts to lower the dielectric constant by mixing in MgO yet still retaining the microwave properties of the ferroelectric.

In addition to using oxide ferroelectrics, the COSMQC architecture proposes to use single spins confined in Si/Ge quantum dots as qubits. We wish to characterize the materials using the optical technique of Kerr rotation microscopy. In order to get to the single spin level we have developed a continuous wave laser measurement technique that we hope can resonantly enhance the Kerr rotation spectrum from a single spin. The development of this instrument is presented in Chapter 6. The creation of Si/Ge quantum dots is an ongoing research project, and we have therefore focused our optical measurements on other more well-developed quantum dot systems made from group III and V atomic elements. Our efforts to optically measure single electrons in these materials are described in Chapter 7.

While not part of the original COSMQC proposal, the high-mobility interface of LaAlO₃ and SrTiO₃ is an exciting new material system in which to explore physics. This system has been informally proposed as a method to construct lateral confining gates for quantum dots in a Si 2DEG, a system which could potentially be used to construct a Si-based quantum computer [61]. Recent low-temperature experiments indicate that this material (along with its ability to form nanostructures) may be suitable as the foundation of a topological quantum computer [62, 63]. I have focused on exploring the optical properties of the LaAlO₃/SrTiO₃ interface, and the creation of rewritable, nanoscale photodetectors is shown in Chapter 8.

Chapter 9 will summarize this work and provides some future directions in which it can taken.

2.0 EXPERIMENTAL METHODS

This chapter will explain the physical origin of the experimental methods we use to investigate oxides and semiconductors. After a discussion of optical methods used in the study of ferroelectric materials, I will present optical experiments for semiconductors and techniques used to characterize semiconductor quantum dots. Finally, this section will conclude with a discussion of photoconductivity measurements that are used to characterize oxide nanostructures.

2.1 ELECTRO-OPTIC EFFECT

The electro-optic effect occurs in a medium that possesses an electric field-dependent index of refraction, $n(E)$ (Ref. 64). We will first consider an isotropic material, one in which n is the same for light traveling in all directions. If n varies slightly with E we can perform a Maclaurin series expansion,

$$n(E) = n_0 + a_1E + \frac{1}{2}a_2E^2 + \dots, \quad (2.1)$$

where $n_0 = n(0)$, $a_1 = dn/dE$, and $a_2 = d^2n/dE^2$. It is convenient to rewrite Equation 2.1 in terms of new coefficients $r = -2a_1/n^3$ and $s = -a_2/n^3$:

$$\Delta n = n(E) - n_0 = \frac{1}{2}rn^3E - \frac{1}{2}sn^3E^2 + \dots. \quad (2.2)$$

If a materials only has a linear dependence on the electric field then we have the equation

$$\Delta n_P \approx -\frac{1}{2}rn^3E. \quad (2.3)$$

This is known as the Pockels effect. r is the Pockels coefficient, which is also known as the linear electro-optic coefficient.

In many materials the index of refraction must be a symmetric function of the electric field such that under the transformation $\mathbf{r} \rightarrow -\mathbf{r}$ the material retains the same index of refraction. This notably occurs in gases, liquids, and even some semiconductors such as Si and Ge. This also means the first derivative of the electric field must vanish and in this case we encounter the Kerr effect:

$$\Delta n_K \approx -\frac{1}{2}sn^3E^2, \quad (2.4)$$

where s is the Kerr coefficient or quadratic electro-optic coefficient.

To consider the anisotropic case, it is useful to consider the electric impermeability $\eta = \epsilon_0/\epsilon = 1/n^2$. The change in impermeability is $\Delta\eta = (d\eta/dn)\Delta n$ such that

$$\Delta\eta = (-2/n^3)(-\frac{1}{2}rn^3E - \frac{1}{2}sn^3E^2) = rE + sE^2, \quad (2.5)$$

and therefore

$$\eta(E) \approx \eta_0 + rE + sE^2. \quad (2.6)$$

An anisotropic material will have an index ellipsoid, such that

$$\sum \eta_{ij}x_ix_j = 1, \quad (2.7)$$

where $\eta_{ij} = \eta_{ji} = \epsilon_{ij}^{-1}$ are elements of the impermeability tensor. Now, equation 2.6 becomes

$$\eta_{ij}(E) = \eta_{ij} + \sum r_{ijk}E_k + \sum s_{ijkl}E_kE_l, \quad (2.8)$$

where $\eta_{ij} = \eta_{ij}(0)$, $r_{ijk} = \partial\eta_{ij}/\partial E_k$, and $s_{ijkl} = \frac{1}{2}\partial^2\eta_{ij}/\partial E_k\partial E_l$.

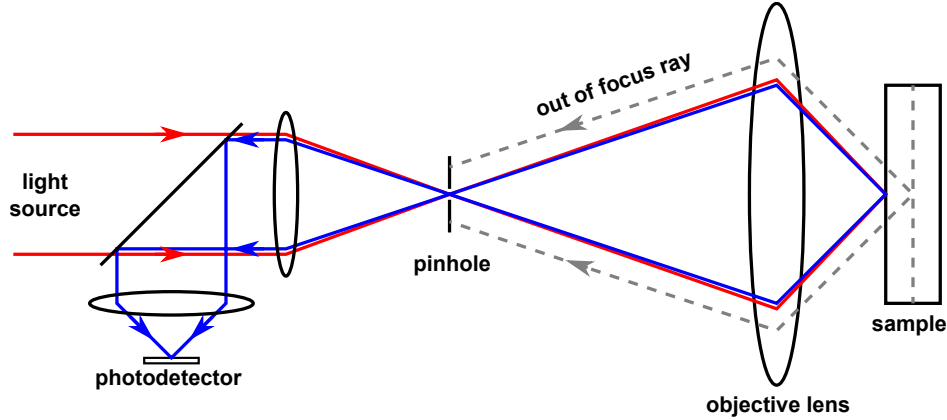


Figure 2.1: Principle of Confocal Scanning Optical Microscopy (CSOM). Light is focused through a pinhole then collected and focused onto the sample of interest. The reflected light is collected through the same pinhole, and out of focus light is rejected by the pinhole.

2.1.1 Confocal Scanning Optical Microscopy

Confocal scanning optical microscopy (CSOM) is a technique used to increase optical resolution. Figure 2.1 shows the principle of CSOM. Light is passed through a pinhole before being focused onto the sample surface by a microscope objective. The reflected light is then collected through the same pinhole. The pinhole serves two purposes: (1) initially, the pinhole acts as a spatial filter to remove modes other than Gaussian, and (2) after reflection from the sample, the pinhole rejects scattered light that does not originate from the focal plane. In this way both lateral *and* axial spatial resolution can be improved.

The diffraction limited lateral resolution is given by

$$\delta x = 0.82 \frac{\lambda}{NA}, \quad (2.9)$$

where λ is the wavelength and NA is the numerical aperture of the focusing lens. The axial resolution is

$$\delta z = \frac{\lambda}{2(NA)^2}. \quad (2.10)$$

If one uses polarized light, CSOM can be used as a sensitive detector of small changes in refractive index ($\Delta n/n \sim 10^{-7}$). In a ferroelectric material, an electric field can be used to modulate the electric field-dependent index of refraction, dn/dE , and a lock-in amplifier can be used to measure this small signal. The Fresnel expression for reflection at normal incidence is

$$R = (n - 1)^2 / (n + 1)^2. \quad (2.11)$$

The CSOM measurement is sensitive to dR/dE using a lock-in amplifier:

$$\frac{dR}{dE} = \frac{dR}{dn} \frac{dn}{dE} = \left(\frac{2(n-1)}{(n+1)^2} - \frac{2(n-1)^2}{(n+1)^3} \right) \frac{dn}{dE}. \quad (2.12)$$

Normalization by R (which is straightforward experimentally) will compensate for topography-induced changes in the signal:

$$\frac{1}{R} \frac{dR}{dE} = \frac{(n+1)^2}{(n-1)^2} \left(\frac{2(n-1)}{(n+1)^2} - \frac{2(n-1)^2}{(n+1)^3} \right) \frac{dn}{dE}, \quad (2.13)$$

$$\frac{1}{R} \frac{dR}{dE} = \frac{4}{n^2 - 1} \frac{dn}{dE}. \quad (2.14)$$

Now consider Equation 2.8. If we rewrite the polarization as a sum $P_i = P_i^s + P_i'$ and expand about P_i' , one finds that

$$r'_{ijk} = 2s'_{ijkl} P_l^s. \quad (2.15)$$

Next express $P'_k = \chi_k \Delta E_k$ (because electric and optical fields point along crystallographic axes). Use $\eta = 1/n^2$ and $\Delta\eta = \frac{d\eta}{dn} \Delta n$, and Equation 2.8 to find that

$$\Delta\eta_i = \frac{-2}{n_i^3} \Delta n_i = 2s'_{ijkl} \chi_k P_l^s, \quad (2.16)$$

and therefore

$$\frac{\Delta n_i}{\Delta E_k} = -n^3 s'_{ijkl} \chi_k P_l^s. \quad (2.17)$$

Experimentally, the electrical and optical fields are parallel and point along a principal axis:

$$\frac{1}{R} \frac{dR}{dE} = -\frac{4}{n_x^2 - 1} n_x^3 s'_{xxxx} \chi_x P_x^s. \quad (2.18)$$

Therefore, the quantity that CSOM is sensitive to is the product of the linear susceptibility χ_x and polarization along the direction of the applied field E .

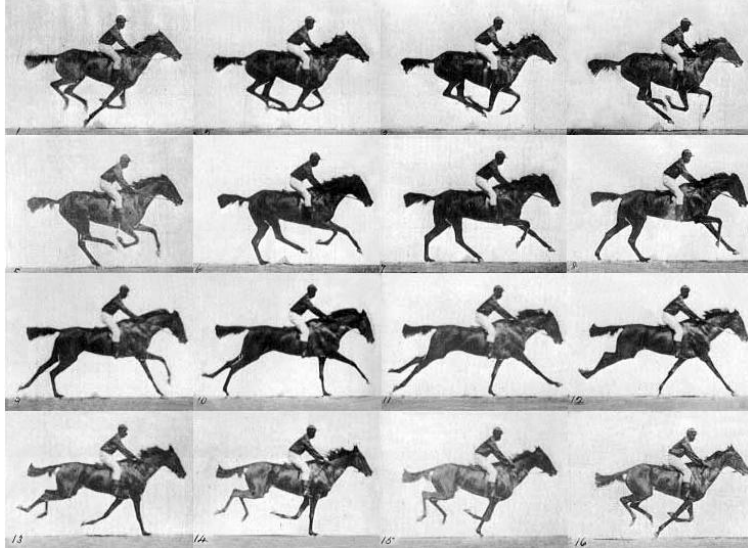


Figure 2.2: Photographs of a galloping horse by Eadweard J. Muybridge. (*These images are in the public domain.*)

2.1.2 Time-Resolved CSOM

We can collect time-resolved information about the ferroelectric polarization by performing a stroboscopic measurement. As this technique to gather time-resolved information is distinct from the non-sampling method that we will discuss in §2.4.1, I will describe it in some detail.

A stroboscopic measurement is in principle the same as the stop-motion photography techniques pioneered by Eadweard J. Muybridge to film a galloping horse in motion (Fig. 2.2). The subject with a time dependence, be it a galloping horse or changing ferroelectric polarization, is measured at different times of its motion. As discussed previously, we can interrogate the ferroelectric polarization with a linear-polarized laser and to measure its time dependence we can use a pulsed laser.

To perform a time-resolved CSOM (TR-CSOM) measurement we derive a microwave-frequency electrical signal that is phase-locked to a harmonic of the pulsed laser repetition rate. For a typical repetition rate of 76 MHz the phase-locked microwaves will be in the range 2 – 4 GHz. The microwave signal is applied in-plane to the sample. The microwaves are delayed relative to the laser

pulses using an electrical delay line. By probing the sample at different time delays we can map out the changing ferroelectric polarization for a full cycle of the microwave signal. TR-CSOM has been used to measure the local dynamic response in (Ba,Sr)TiO₃ thin films, revealing a mesoscopic dispersion at microwave frequencies [65]. Hongzhou Ma has combined this time-resolved technique with a sub-diffraction limit probe (ANSOM) to measure the dynamics of ferroelectrics on sub-100 nm spatial scales [66].

2.1.3 Spectroscopic Time-Resolved CSOM

We also investigate the spectral response of the ferroelectric to different applied microwave frequencies. We can programmatically adjust the frequency multiplier to study the full range of harmonics we are able to produce from the PLO. This experiment then produces a 4-dimensional data set: two spatial (x and y), time (t), and frequency (f). A full experiment takes on the order of 12 hours to complete, so careful control of temperature to minimize sample drift is employed.

Even though we are able to control the temperature to ~ 0.02 K, it is still necessary to perform image alignment before data analysis. Scripts using LabVIEW and ImageJ are used to align image stacks using reflectivity images as references. The reflectivity image stack is shifted and aligned, and the images containing the time and frequency dependence are shifted by the same amount. The image alignment and data processing procedures are described in more detail in Appendix A.

2.2 SECOND HARMONIC GENERATION

Not until the invention of the laser in 1960 was light with a sufficiently high intensity available to observe nonlinear optical effects. Second harmonic generation (SHG) is a nonlinear optical phenomenon where incident light with frequency ω is doubled so that $\omega' = 2\omega$ and, equivalently, $\lambda' = \lambda/2$. This effect was first observed in 1961 [67] by shining light from a pulsed Ruby laser ($\lambda \sim 694$ nm) onto a quartz plate. The second harmonic light ($\lambda' \sim 347$ nm) was separated from the fundamental using a prism spectrometer. Infamously, the journal editors mistakenly thought the faint second harmonic line was an error and blanked it before publication.

We can expand the polarization P in a material in powers of the electric field E . In scalar form we can write this as

$$P(t) = \chi E(t) + \chi a_1 E(t)^2 + \chi a_2 E(t)^3 + \dots . \quad (2.19)$$

Second harmonic generation will result from the second term. For an incident optical field with frequency ω , we can write its electric field as

$$E(t) = E_0 \sin(\omega t) . \quad (2.20)$$

By inserting Equation 2.20 into the second term of Equation 2.19, we find the quadratic field contribution to the polarization, $P^{(2)}(t)$,

$$P^{(2)}(t) = \chi a_1 E_0^2 \sin^2(\omega t) . \quad (2.21)$$

Apply an elementary trig function ($\sin^2 \theta = (1 - \cos 2\theta) / 2$) and one finds two components of the quadratic polarization:

$$P^{(2)}(t) = \frac{1}{2} \chi a_1 E_0^2 - \frac{1}{2} \chi a_1 E_0^2 \cos(2\omega t) . \quad (2.22)$$

The first term is the polarization that contributes to the Kerr effect (Eq. 2.4). The second term, with a $\cos(2\omega t)$ dependence, results in the generation of light with frequency 2ω from the material.

While the above analysis was performed for an isotropic material (for mathematical simplicity), it is actually the case that an isotropic material (or one with a center of inversion symmetry) will not have a second harmonic response. In these materials the polarization must reverse sign if the electric field reverses sign. This means there can be no terms in Equation 2.19 with even powers of E . Materials with a ferroelectric phase generally lack a center of inversion symmetry. This, along with their relatively large susceptibility, allow ferroelectrics to have a second harmonic response.

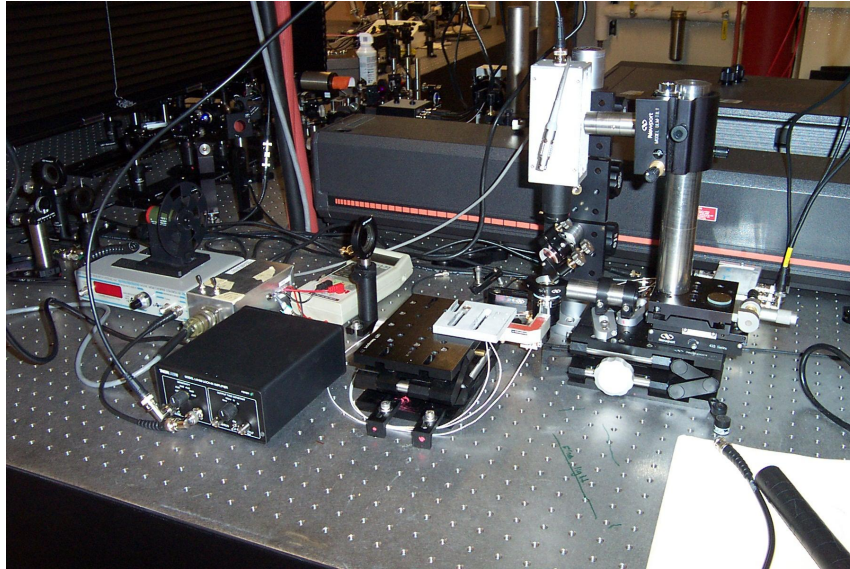


Figure 2.3: Photograph of second harmonic detection experiment. The sample is mounted on a three-axis stage, the red “L” in the center of the photo. Above the sample is a white box, which is the APD. For a time-resolved measurement, the reflected infrared light is directed back through the beam path to a balanced photodiode. The Ar^+ pump laser is the black box in the background with the red stripe, behind which is the Ti:sapphire pulsed laser.

2.2.1 Second-Harmonic CSOM

We use second harmonic generation, in conjunction with CSOM, to study ferroelectricity in a ferroelectric/dielectric composite material (See Chapter 5). A photograph of our second-harmonic detection experiment is shown in Figure 2.3. Light from a Ti:sapphire laser is focused onto the sample after reflection from an ultrafast mirror. The ultrafast mirror acts as a dichroic mirror and passes any frequency-doubled light generated by the sample. The SH light is then collected by a thermoelectrically-cooled, ultraviolet-enhanced avalanche photodetector.

2.3 OPTICAL SELECTION RULES

Although we are motivated to use group IV materials such as Ge/Si quantum dots for quantum computing, the experiments done in this thesis are performed on III-V materials: bulk n -GaAs, GaAs/AlGaAs quantum dots, and InAs/GaAs quantum dots. These experiments will be described in more detail in Chapters 6 and 7, as well as our reasons for studying these systems. This section will describe optical orientation (the control of carrier spin with light) [68] in GaAs and related structures.

GaAs has a zinc-blende lattice structure, as shown in Figure 2.4. This lattice can be thought of as two overlapping face-center cubic (fcc) lattices, one of atomic species Ga and the other As. The origin of one lattice is located at $(0, 0, 0)$ and the other at $(a/4)(1, 1, 1)$, where $a = 5.65 \text{ \AA}$ for GaAs.

The band structure of GaAs is shown schematically in Figure 2.5. GaAs is a direct-bandgap semiconductor, meaning the bottom of the conduction band and the top of the valence band are located at the same point in k -space. The direct bandgap of GaAs is 1.424 eV at room temperature and is located at the Γ -point, the center of the Brillouin zone. The conduction band results from s -orbitals and the states are “ s -like,” meaning the orbital angular momentum is zero ($l = 0$). The valence band states are “ p -like,” meaning $l = 1$. The valence band consists of three sub-bands: the heavy-hole band, the light-hole band, and the split-off band. Each band, including the conduction band, is twice degenerate in spin.

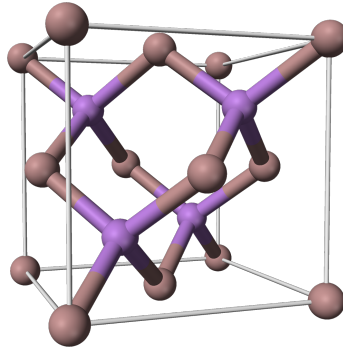


Figure 2.4: Unit cell of GaAs showing the zinc-blende crystal structure. Brown and purple spheres represent Ga and As, respectively. (This image, by Ben Mills, has been released into the public domain.)

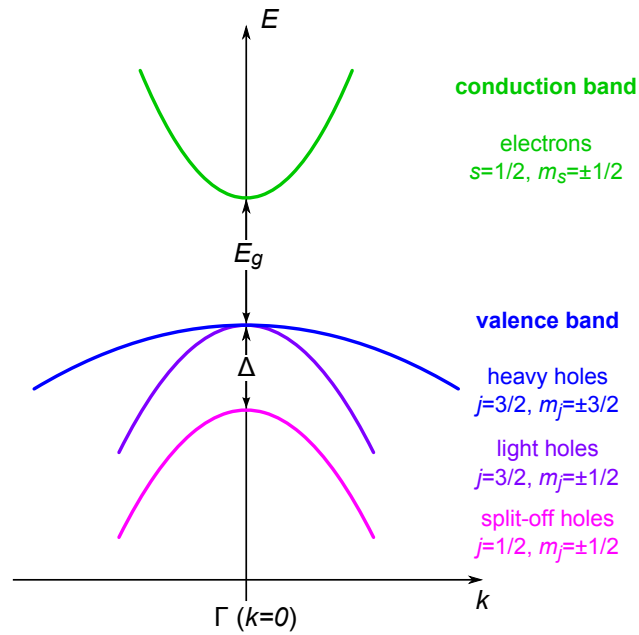


Figure 2.5: GaAs band diagram. Near the Γ -point the energy spectrum is parabolic with the general form $E(k) = \hbar^2 k^2 / 2m^*$, where m^* is the effective mass of the particle in the relevant band. E_g is the band gap and Δ is the spin-orbit coupling energy.

Because $l = 1$, the eigenstates of the valence band are described by eigenvalues of J and J_z . Near the zone-center the bands are nearly parabolic. The energy spectrum of the conduction band and heavy- and light- hole bands are given by

$$\epsilon_i = \hbar^2 k^2 / 2m^*$$

where m^* is the effective mass of the carriers in their respective bands. The mass of an electron in the conduction band is $m_c = 0.154m_0$, where m_0 is the free electron mass. The mass of a heavy hole ($j = 3/2$, $m_j = \pm 3/2$) is $m_h = m_0 / (\gamma_1 - 2\gamma) = 0.45m_0$. The mass of a light hole ($j = 3/2$, $m_j = \pm 1/2$) is $m_l = m_0 / (\gamma_1 + 2\gamma) = 0.082m_0$. $\gamma = (2\gamma_2 + 3\gamma_3) / 5$, where $\gamma_1 \sim 7$, $\gamma_2 \sim 2$, $\gamma_3 \sim 3$ are Luttinger's parameters. Mixing of states in the light-hole and the split-off bands result in the spectrum developing nonparabolicity, although near the zone-center we can typically ignore this.

A circularly polarized photon will have spin angular momentum parallel or antiparallel to its propagation vector for right and left circularly polarized light, respectively. This momentum will be transferred to the electron as it is excited from the valence band to the conduction band. If it is unable to be transferred, then this transition is considered “dark” or “forbidden.”

We can calculate which transitions are allowed and their probability using Fermi's golden rule:

$$T_{b \leftarrow a} = \frac{2\pi}{\hbar} |\langle b | V | a \rangle|^2 \delta(E_g - \hbar\omega), \quad (2.23)$$

where $T_{b \leftarrow a}$ is the transition rate for going from state a to b . For light exciting a quantum transition we can use the dipole approximation and thus we are interested in the matrix elements of the dipole operator: $V = e\vec{r} \cdot \vec{E}$. To calculate the transition probabilities we need to calculate the matrix elements $V_{b \leftarrow a} = \langle b | e\vec{r} \cdot \vec{E} | a \rangle$. Light with left- and right-circular polarization has the electric field oriented along $\vec{r} = -(\hat{x} \pm i\hat{y}) / \sqrt{2}$. Making this substitution gives us

$$V_{b \leftarrow a} = \langle b | \hat{x} \pm i\hat{y} | a \rangle. \quad (2.24)$$

An operator of the form $\hat{x} \pm i\hat{y}$ acts like a spherical tensor of rank 1: $\hat{x} \pm i\hat{y} \rightarrow T_{\pm 1}^{(1)}$ [69], thus we need to calculate

$$V_{b \leftarrow a} = \langle b | T_{\pm 1}^{(1)} | a \rangle. \quad (2.25)$$

As an example, we will calculate the transition probability for exciting a spin-up electron from a spin-up heavy hole with left-circular (σ_+) polarized light. The initial state is $|a\rangle = |j, m_j\rangle = |\frac{3}{2}, -\frac{3}{2}\rangle$ and the final state is $|b\rangle = |\frac{1}{2}, -\frac{1}{2}\rangle$. Therefore the relevant matrix element is

$$V_{c\leftarrow hh} = \left\langle \frac{1}{2}, -\frac{1}{2} \left| \hat{x} + i\hat{y} \right| \frac{3}{2}, -\frac{3}{2} \right\rangle. \quad (2.26)$$

Transforming to the spherical tensor representation,

$$V_{c\leftarrow hh} = \left\langle \frac{1}{2}, -\frac{1}{2} \left| T_{+1}^{(1)} \right| \frac{3}{2}, -\frac{3}{2} \right\rangle, \quad (2.27)$$

allows us to apply the Wigner-Eckart Theorem, which tells us that the matrix element of a tensor operation on angular momentum eigenstates is the product of a Clebsch-Gordan coefficient $\langle j, k; m_j, q | j, k; j', m_j' \rangle$ with a number, A , that is independent of j , where k and q are the order and value of the tensor (respectively) [69]. Thus for our example:

$$\left\langle \frac{1}{2}, -\frac{1}{2} \left| T_{+1}^{(1)} \right| \frac{3}{2}, -\frac{3}{2} \right\rangle = A \left\langle \frac{3}{2}, 1; -\frac{3}{2}, +1 \left| \frac{3}{2}, 1; \frac{1}{2}, -\frac{1}{2} \right\rangle = \frac{1}{2}A. \quad (2.28)$$

Similarly for an excitation from a spin-up light hole to a spin down electron with σ_+ light:

$$\left\langle \frac{1}{2}, +\frac{1}{2} \left| T_{+1}^{(1)} \right| \frac{3}{2}, -\frac{1}{2} \right\rangle = A \left\langle \frac{3}{2}, 1; -\frac{1}{2}, +1 \left| \frac{3}{2}, 1; \frac{1}{2}, +\frac{1}{2} \right\rangle = \frac{1}{6}A. \quad (2.29)$$

If we perform the calculation for the same two initial and final states with σ_- polarized light, we would find the transition probability is zero, indicating these are forbidden transitions. These results are summarized in Figure 2.6, which shows the *relative* transition probabilities (i.e., $\frac{1/2}{1/6} = 3$) for transitions from the heavy- and light-hole sub-bands to the conduction band.

We can thus use circularly polarized light to create a population of electrons in the conduction band that has a majority spin population oriented along one direction. The previous analysis, which is relevant for *bulk* GaAs, tells us that if we pump the system with σ_+ light, for every four photons we would create 3 spin up electrons and 1 spin down electron, resulting in a maximum $P = (3 - 1) / (3 + 1) = 50\%$ spin polarization. Experimentally, one typically pumps with alternating σ_+ and σ_- light and then take the difference, thus having the additional effect of canceling any signals that are not related to spin.

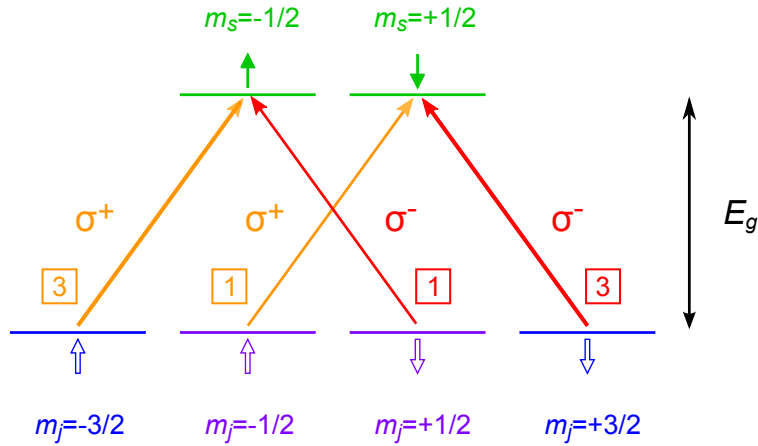


Figure 2.6: Selection rules near the zone-center.. Numbers in boxes and width of lines indicate the relative strength of the transition.

2.4 FARADAY ROTATION

The Faraday effect is the rotation of the polarization axis of linearly polarized light as it passes through a material with a non-zero magnetization. It is also known as Faraday rotation and, in a reflection geometry, Kerr rotation. This effect was first observed by Michael Faraday in 1845 [70]. His experiment consisted of first creating linearly polarized light from an oil lamp. He then oriented a polarizer such that it extinguished the polarized light. By placing “silicated borate of lead” glass in the beam path, and turning on a magnetic field in the direction of the beam propagation direction, he could restore the extinguished light “at pleasure.”

Faraday rotation has found technological applications as an optical isolator¹ to prevent scattered light from reentering a laser cavity. Faraday (and Kerr) rotation can also be used as a very sensitive optical magnetometer in a variety of materials. It has been used to measure a single monolayer of Fe [71], to image the spin Hall effect in a semiconductor [72], and the hard drive industry uses it to verify the magnetic properties of thin-film hard drive disks.

¹Essentially an optical diode for a specific polarization orientation.

The magnetization in a material may arise spontaneously (ferromagnetism), by application of an external field H such that $M = \chi H$ (as done by Faraday), or optically in a semiconductor (as discussed in §2.3). The last situation is what we will be concerned with.

The rotary power of a material, ρ (an angle per unit length), is a product of magnetic flux B and the Verdet constant V such that the Faraday rotation angle (after transmission through a material of length L) is given by

$$\vartheta_F = \rho L = VBL. \quad (2.30)$$

We can re-express this in terms of the frequency of light, ω , and the index of refraction of left- and right-circularly polarized light, n_{\pm} :

$$\vartheta_F(\omega) = \frac{\omega L}{2c} (n_+(\omega) - n_-(\omega)). \quad (2.31)$$

In other words, Faraday rotation results because of a circular birefringence in the material.

To see how a *circular* birefringence can rotate the polarization of *linearly* polarized light, consider the electric field of monochromatic light polarized in the \hat{x} -direction:

$$E(0, t) = E_0 \cos(\omega t) \hat{x}. \quad (2.32)$$

This can be written as a superposition of left- and right-circularly polarized light:

$$E(0, t) = \frac{E_0}{2} \{(\cos(\omega t) \hat{x} + \sin(\omega t) \hat{y}) + (\cos(\omega t) \hat{x} - \sin(\omega t) \hat{y})\}. \quad (2.33)$$

Rewriting this in complex notation, one finds:

$$E(0, t) = \frac{E_0}{2} \Re \{(\hat{x} + i\hat{y}) e^{-i\omega t} + (\hat{x} - i\hat{y}) e^{-i\omega t}\}. \quad (2.34)$$

$$E(0, t) = \frac{E_0}{2} \Re \{[(\hat{x} + i\hat{y}) + (\hat{x} - i\hat{y})] e^{-i\omega t}\}.$$

Now consider propagation in the z -direction. Light with σ_{\pm} polarization will propagate with wavevectors $k_{\pm} = n_{\pm} \omega / c$, such that

$$E(z, t) = \frac{E_0}{2} \Re \{[(\hat{x} + i\hat{y}) e^{ik_+z} + (\hat{x} - i\hat{y}) e^{ik_-z}] e^{-i\omega t}\}. \quad (2.35)$$

Propagate the beam a distance L , and substitute $\varphi_{\pm} = k_{\pm} L$:

$$E(L, t) = \frac{E_0}{2} \Re \{[(\hat{x} + i\hat{y}) e^{i\varphi_+} + (\hat{x} - i\hat{y}) e^{i\varphi_-}] e^{-i\omega t}\}. \quad (2.36)$$

Now rewrite the term in square brackets:

$$\Omega = (\hat{x} + i\hat{y}) e^{i\varphi_+} + (\hat{x} - i\hat{y}) e^{i\varphi_-}. \quad (2.37)$$

$$\Omega = (\hat{x} + i\hat{y})(\cos \varphi_+ + i \sin \varphi_+) + (\hat{x} - i\hat{y})(\cos \varphi_- + i \sin \varphi_-). \quad (2.38)$$

Expand and collect terms

$$\Omega = (\cos \varphi_+ + \cos \varphi_-) \hat{x} + i(\sin \varphi_+ + \sin \varphi_-) \hat{x} - (\sin \varphi_+ - \sin \varphi_-) \hat{y} + i(\cos \varphi_+ - \cos \varphi_-) \hat{y}. \quad (2.39)$$

Apply the sum-to-product trigonometric identity and collect terms:

$$\Omega = 2 \left(\cos \left(\frac{\varphi_+ + \varphi_-}{2} \right) + i \sin \left(\frac{\varphi_+ + \varphi_-}{2} \right) \right) \left(\cos \left(\frac{\varphi_+ - \varphi_-}{2} \right) \hat{x} + \sin \left(\frac{\varphi_+ - \varphi_-}{2} \right) \hat{y} \right). \quad (2.40)$$

$$\Omega = 2e^{i(\varphi_+ + \varphi_-)/2} \left(\cos \left(\frac{\varphi_+ - \varphi_-}{2} \right) \hat{x} + \sin \left(\frac{\varphi_+ - \varphi_-}{2} \right) \hat{y} \right). \quad (2.41)$$

Therefore,

$$E(L, t) = E_0 \Re \left\{ \left[\cos \left(\frac{\varphi_+ - \varphi_-}{2} \right) \hat{x} + \sin \left(\frac{\varphi_+ - \varphi_-}{2} \right) \hat{y} \right] e^{i(\varphi_+ + \varphi_-)/2} e^{-i\omega t} \right\}, \quad (2.42)$$

which is a rotation of the polarization axis by an angle

$$\vartheta_F = \frac{1}{2} (\varphi_+ - \varphi_-) = \frac{\omega L}{2c} (n_+ - n_-). \quad (2.43)$$

It is noted that Faraday or Kerr rotation is only sensitive to magnetization (spin orientation) along the light propagation direction. By adjusting the incident angle of the light on the sample one can measure spins oriented normal to the sample (polar geometry) or in the sample plane (longitudinal or transversal geometry).

To think about the origin of the Faraday effect, consider a material with majority spin-up carriers that occupy the lowest energy states in the conduction band. For more carriers to absorb σ_+ photons the light would need enough energy to excite spin-up carriers into the unoccupied states. In other words, the lowest occupied states are Pauli-blocked. Thus the absorption edge for σ_+ light is shifted to higher energy relative to σ_- . One can then use the Kramers-Kronig dispersion relations to see that the indices of refraction are likewise shifted.

To measure Kerr rotation experimentally linearly polarized light is focused onto the sample. The reflected light is directed to an optical polarization bridge consisting of a polarizing beamsplitter and two detectors. The beamsplitter sends vertically and horizontally polarized light to the two detectors, V and H . If the light enters the bridge at 45° the difference signal from the detectors, $V - H$, will be zero, in other words, the detector is balanced. However, if the sample develops an unbalanced spin population, the light will be rotated and the detector will become unbalanced. By applying a small angle approximation, it is straightforward to show how the signals from the detector relate to the Faraday rotation angle [73]:

$$\vartheta_F \approx \frac{1}{2} \frac{V - H}{V + H}. \quad (2.44)$$

While being sensitive to optical rotation, an added benefit (that is perhaps equally important) is that noise from the laser (manifested as intensity fluctuations) will be sent to each arm of the detector equally and therefore will be canceled.

To measure time-resolved Faraday rotation one can use a stroboscopic technique, as was discussed in §2.1.2. Although in contrast to measuring the dynamics of ferroelectrics, Faraday rotation is an all-optical experiment and therefore uses a pulsed laser as both pump and probe. Light from a mode-locked laser is split into two beams. One beam, the pump, is made to be circularly polarized and will create spin polarized electrons in the conduction band due to optical selection rules (discussed in §2.3). The second beam, the probe, is linearly polarized and goes through an optical delay line (a retroreflecting mirror mounted on a sliding car) before going to the sample. The delay line retards the probe pulse a time δt relative to the pump pulse. The rotation angle ϑ_F is measured as a function of δt by scanning the delay line and measuring the reflected probe light with the same polarization bridge described above. Although this measurement scheme can probe spin dynamics on picosecond time scales, because it is a sampling technique the detector needs to only have a bandwidth high enough to detect any modulation used for lock-in detection (typically $f_R < 100$ kHz).

2.4.1 GHz Optical Spin Transceiver

In order to measure the single spin dynamics in a single quantum dot, we have pursued a different type of time-resolved experiment than the stroboscopic measurement presented in §2.1.2. In this case, we have replaced the pulsed probe laser with a continuous wave (CW) laser, in other words, one that is always on. Time resolution is then achieved by using fast detectors and electronics to digitize the signal in real time. There are several advantages to this approach, as discussed below.

We call our measurement technique a GHz Optical Spin Transceiver (GHOST). Although we have developed this technique to measure the dynamics of single spins (hence the name) it is applicable to other physical systems as well. We still retain a pulsed laser to pump the spins, which creates our “zero” time delay. The CW probe laser is then focused to the same spot as the pump, where its polarization angle is rotated by the out-of plane spin population. The reflected probe laser is collected and its polarization angle is analyzed by a polarization bridge with fast photodetectors. The output of the bridge is sent to a high-bandwidth oscilloscope where it digitizes 1.6 ms of data in real time. This data goes into the on-board fast SiGe memory. From there it is transferred to conventional “slow” Si memory so that our LabVIEW software can access it for processing.

Our original motivation for pursuing this measurement technique was to resonantly enhance the signal from a single quantum dot. The linewidth of a single exciton transitions of less than 40 μeV , as measured by photoluminescence [60]. The spectrum of a pulsed laser is limited by the time-energy uncertainty principle,

$$\Delta E \geq \hbar/(2\Delta t),$$

where ΔE is the spectral width, \hbar is Plank’s constant, and Δt is the temporal width of the laser pulse. As the pulse width narrows, the spectrum necessarily broadens. Pulses from a Ti:Sapphire laser with 150 fs pulsewidth at $\lambda = 750$ nm will have a transform-limited spectral width of $\Delta E \sim 12$ meV. However for a CW laser, the energy bandwidth can become extremely narrow: a laser with bandwidth of 1 MHz has a transform-limited spectrum of less than 1 neV. It should be noted that our ~ 1 GHz detection bandwidth limits us to ~ 1 μeV energy resolution. This works to our advantage because the Faraday rotation signal is also very narrow, and we can thus resonantly enhance the FR signal.

A second advantage is in the mechanics of the measurement technique itself. Performing an optical pump-probe time-resolved measurement requires the scanning of a long mechanical delay line (60 cm for a modest 4 ns of delay), which can be cumbersome to align and time-consuming to scan. Our method of using a CW laser uses a fast photodetector and oscilloscope to digitize the signal in real time and the maximum time delay accessible automatically becomes the laser repetition rate. This becomes especially convenient if one uses a pulse picker or other device to reduce the repetition rate to sub-MHz or even kHz rates, which would require a kilometer-long delay line.

Perhaps more important than the ease of accessing very long delay times, the continuous wave measurement has the advantage of *always* collecting data. When using a pulsed laser, the delay line is fixed a certain time delay and the experimenter is *only* measuring data at that time delay. All of the other times in the experiment are inaccessible. In our measurement we are always collecting data and therefore we can take less time to achieve our desired signal to noise ratio. This becomes even more significant when our signal of interest contains fluctuations.

One reason this technique should be so valuable for single spin measurements is that it samples the noise better than a pump-probe experiment using pulsed beams. Essentially the cw probe is always measuring the system. Because of imperfect coupling between the optical field and the spin, the spin may not always be in the state that one wishes to put it into. The GHOST technique is able to average over these events. This is what leads to what we call "intrinsic noise" of the experiment.

The Faraday rotation signal from a semiconductor can be quite small, on the order of 10^{-5} radians for a single electron. Using a fully quantum-mechanical model of Faraday rotation, Ma and Levy [74] have found that there exists an intrinsic noise term, not related to shot noise, that is the result of the circularly polarized pump photon sometimes creates a mixed state instead of the expected pure spin-up or down state. They found the following expression for the fluctuation of the Faraday angle when neglecting hyperfine interactions:

$$\Delta\theta_F(t, \tau) = \sqrt{1/4N + \tau(1 - \tau)(\theta_+ - \theta_-)^2}, \quad (2.45)$$

where θ_{\pm} is the Faraday rotation angle for an initially pure spin state, and τ is a measure of the purity of the state ($\tau = 1/2$ is a fully mixed state). The first term under the radical is related to photon shot noise and the second term is a measure of the intrinsic noise.

The existence of intrinsic noise can be minimized by continuous measurement. Unfortunately, to accomplish this task requires electronics that are not commercially available. The original GHOST experiments were performed with a high bandwidth (6 GHz) oscilloscope and DSP done in software on a PC. The oscilloscope can acquire 1.6 ms of continuous data, which corresponds to about 120,000 experiments (120k pump laser repetitions), but the scope requires on the order of 10 seconds to "recover" before the next 1.6 ms acquisition can begin.

To overcome this problem we have entered into a collaboration with MaxTek/Tektronix to use hardware that they are developing that combines a fast ADC (12 GS/s) with a field-programmable gate array (FPGA). The FPGA allows us to process the high-speed data in real time before transferring the data to a computer. This so-called FPGA GHOST is not used in this thesis and will be the subject of some future work.

2.5 PHOTOLUMINESCENCE

Luminescence is the process by which an excited system relaxes to the ground state by emitting a photon to conserve energy. If the system is initially excited by a photon this process is known as *photoluminescence*. A photoluminescence spectroscopy measurement is typically performed by exciting carriers non-resonantly with above-bandgap light. The carriers then recombine by emitting a photon, the energy of which will tell us about the internal states of the material. Carriers may radiatively recombine across the band gap, between donors or acceptors, with or without phonon assistance, or by annihilation of an exciton.

The optical selection rules described in §2.3 are also valid for carrier recombination. Thus, detecting the polarization of photoluminescence can give us information about the spin orientation of electrons and holes. This effect is used in a Hanle measurement, which measures the depolarization of spins in a magnetic field. A circularly polarized laser is used to excite spin-polarized electrons. Applying a magnetic field transverse to the initial spin orientation will cause the spins to

process. Measurement of the circular polarization of the photoluminescence will reveal the average number of spins oriented along the measurement direction.

Photoluminescence spectroscopy has been used as a sensitive probe of the internal electronic states in quantum dot. Photoluminescence on single quantum dots has measured neutral excitons by varying the pump power [75] and charged excitons by varying the quantum dot occupancy [76]. A quantum dot molecule is two or more adjacent coupled quantum dots. Photoluminescence on these quantum dot molecules [77, 78] has revealed tunneling between the dots and the coupled charge and spin degrees of freedom are manifested in observable singlet and triplet states. We perform photoluminescence on single quantum dots as a diagnostic tool to identify the energy of single exciton transitions. In this way we will know in what vicinity to tune our probe laser's energy for an absorption of Faraday rotation measurement.

2.6 PHOTOCONDUCTIVITY

If a material changes its conductivity in response to some radiation then it is known as a photoconductor [79]. This property was first observed by Smith in 1873 [80] during experiments he was performing on selenium. In fact, photoconductive selenium was a central component in the first automated photocopiers. A photoconductive drum roller is initially charged. Projecting an image of the document onto the drum causes some of the areas to become conducting and the charge in those regions are able to dissipate. When the charged toner is introduced it will thus only stick to the charged regions.

In general, all materials that are not metals have some degree of photoconductivity. When above-bandgap light creates free electrons in the conductance band (and holes in the valence band), the conductivity of the material increases, which is known as intrinsic photoconductivity. In a doped semiconductor, light with energy much below the bandgap can excite electrons from the impurities into the conduction band. This energy will be on the order of tens of meV and thus can be used as a far-infrared detector. If a doped semiconductor is cooled to low temperature, the carriers will freeze onto the impurities. Light can then ionize the impurities, which is known as extrinsic photoconductivity. Raising the temperature allows one to optically excite carriers into

excited bound states which are then thermally excited into the conduction. This technique, called photothermal ionization spectroscopy, measures the ionization energies of the impurities.

In nanowire devices it is desirable to measure the local photoconductivity because the devices most likely do not have uniform internal electric fields. So called scanning photocurrent imaging has been used to measure Si nanowires [81] and the authors found the nanowires' energy bands are bent at the source and drain contacts. This same technique has been used on Ge nanowires [82] and CdS nanowires [83].

3.0 ROOM TEMPERATURE FERROELECTRICITY IN STRAINED STO

¹ Systems with a ferroelectric to paraelectric transition in the vicinity of room temperature are useful for devices. Adjusting the ferroelectric transition temperature (T_C) is traditionally accomplished by chemical substitution—as in $\text{Ba}_x\text{Sr}_{1-x}\text{TiO}_3$, the material widely investigated for microwave devices in which the dielectric constant (ϵ_r) at GHz frequencies is tuned by applying a quasi-static electric field [84, 85]. Heterogeneity associated with chemical substitution in such films, however, can broaden this phase transition by hundreds of degrees [86], which is detrimental to tunability and microwave device performance. An alternative way to adjust T_C in ferroelectric films is strain [87, 88, 89, 90, 91]. Here we show that epitaxial strain from a newly developed substrate can be harnessed to increase T_C by hundreds of degrees and produce room-temperature ferroelectricity in strontium titanate, a material that is not normally ferroelectric at any temperature. This strain-induced enhancement in T_C is the largest ever reported. Spatially resolved images of the local polarization state reveal a uniformity that far exceeds films tailored by chemical substitution. The high ϵ at room temperature in these films (nearly 7,000 at 10 GHz) and its sharp dependence on electric field are promising for device applications [84, 85].

3.1 INTRODUCTION

Enormous strains can be imparted to thin films and have previously been used to alter the T_C of ferromagnetic [92, 93] and superconducting [94, 95, 96] materials. For such phenomena, strain-induced enhancements in T_C as large as tens of degrees have been observed [92]. Owing to the

¹Originally published in a different form in *Nature* [47].

strong coupling between strain and ferroelectricity, much larger T_C shifts are expected [87, 89], and have been observed [90, 91], in ferroelectric materials.

In its pure, unstressed form, strontium titanate (SrTiO_3) is an incipient ferroelectric. It remains paraelectric down to 0 K, although chemical [97, 98] or isotopic substitution [99], as well as the application of stress [88], easily disturb this delicate state, resulting in ferroelectricity. The boundary conditions imposed by a substrate profoundly affect ferroelectricity in thin films. Figure 3.1 shows the predicted [88] shift in T_C for SrTiO_3 [100] under biaxial strain $\epsilon_S = (a_{\parallel} - a_0)/a_0$, where a_0 is the lattice parameter of free-standing SrTiO_3 and a_{\parallel} is the in-plane lattice parameter of a biaxially strained (100) SrTiO_3 film. The hatched region shows the range in predicted T_C due to the spread in reported property coefficients for SrTiO_3 [101, 102] that enter into the thermodynamic analysis. For example, for positive ϵ_S and $T > 120$ K, the enhancement in T_C is given by $\Delta T_C = 2\epsilon_S \epsilon_0 C(Q_{11} + Q_{12})/(s_{11} + s_{12})$, where ϵ_0 is the permittivity of free space, C is the Curie constant, Q_{11} and Q_{12} are the electrostrictive coefficients, and s_{11} and s_{12} are elastic compliances of SrTiO_3 . The breadth of the hatched region in Figure 3.1 for T_C is mainly due to the nearly factor-of-two variation in the ratio of $(Q_{11} + Q_{12})/(s_{11} + s_{12})$ for what are considered the most accurate reported values of these constants. These predictions imply that a biaxial tensile strain of order 1% will shift the T_C of SrTiO_3 to the vicinity of room temperature.

In practice, the synthesis of uniformly strained ferroelectric films is challenging. Epitaxial ferroelectric films are usually grown to thicknesses greatly exceeding their critical values, resulting in undesirable relaxation towards a zero-strain state by the introduction of dislocations. Dislocation densities of $\sim 10^{11} \text{ cm}^{-2}$ are typical in epitaxial $\text{Ba}_x\text{Sr}_{1-x}\text{TiO}_3$ films [103], and the resulting inhomogeneous strain further smears the phase transition, in addition to the effects of chemical heterogeneity mentioned above. Our approach to controlling the properties of ferroelectric SrTiO_3 films centers on the development of new substrates that enable the growth of uniformly strained films below, or at least far closer to, the critical thickness for relaxation.

Depending on the choice of substrate, films may be grown under compressive or tensile strain. Commercially available substrates that are larger than SrTiO_3 , such as KTaO_3 ($a = 3.989 \text{ \AA}$) [104, 105] or MgO ($a = 4.212 \text{ \AA}$) [104, 105], are unsuitable for high-quality SrTiO_3 ($a = 3.905 \text{ \AA}$) [101] growth because of their excessively large lattice mismatches (2.2% and 7.7%, respectively). On such substrates dislocation introduction commences soon after film nucleation, and films typically

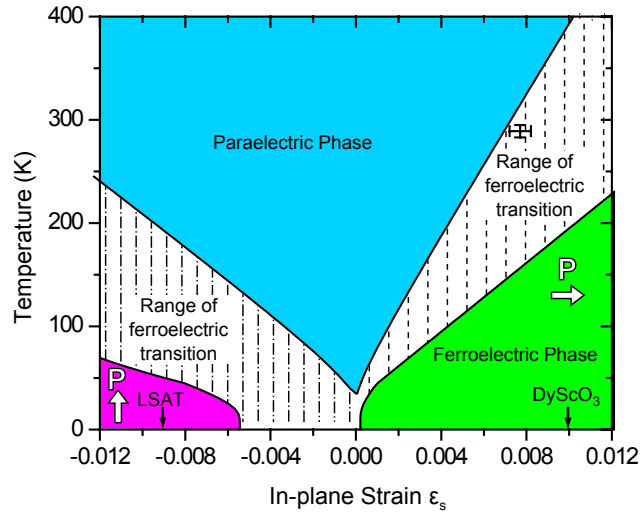


Figure 3.1: Expected shift in T_C of (100) SrTiO₃ with biaxial in-plane strain, based on thermodynamic analysis. The arrows indicate the predicted direction of the polarization for strained SrTiO₃: in-plane for biaxial tensile strain and out-of-plane for biaxial compressive strain. The ϵ_s values for SrTiO₃ fully constrained (commensurate) to the lattice constants of LSAT and (110) DyScO₃ substrates are indicated by the positions of the corresponding arrows. The cross shows the observed T_C shift of a 500 Å-thick SrTiO₃ film epitaxially grown on (110) DyScO₃.

have very large mosaic spread. As the critical thickness at which dislocations begin to form varies approximately inversely with lattice mismatch, lower mismatch is desired to allow strained, low-dislocation density SrTiO₃ films to be grown that are thick enough to allow their ferroelectric properties to be conveniently probed. To produce a closer lattice match, we have developed single crystals of a new substrate material, DyScO₃, for the growth of SrTiO₃ films under uniform biaxial tensile strain. DyScO₃ is orthorhombic with lattice constants [106] $a = 5.440 \text{ \AA}$, $b = 5.731 \text{ \AA}$, and $c = 7.887 \text{ \AA}$. It is not ferroelectric down to 4 K. The (110) DyScO₃ surface has a nearly square surface mesh with an in-plane lattice spacing $a_{\parallel} = 3.944 \text{ \AA}$, resulting in a tensile lattice mismatch at room temperature (25°C) of +1.0% with (100) SrTiO₃. For comparison, the commercial substrate (LaAlO₃)_{0.29}(SrAl_{0.5}Ta_{0.5}O₃)_{0.71} (LSAT [107], $a = 3.869 \text{ \AA}$) with a lattice mismatch of -0.9% at room temperature was also used to grow epitaxial (100) SrTiO₃ films under uniform compressive strain. The low dielectric constants of both DyScO₃ ($\epsilon_{11} = 22.0$, $\epsilon_{22} = 18.8$, and $\epsilon_{33} = 35.5$) and LSAT ($\epsilon_r = 22.5$) [108] reduce field penetration in the substrate and facilitate modeling of the in-plane ϵ_r of the SrTiO₃ films when interdigitated electrodes are used [109], as in this study.

3.2 SAMPLE GROWTH AND CHARACTERIZATION

Reactive molecular beam epitaxy (MBE) was used to grow epitaxial SrTiO₃ films on both (110) DyScO₃ and (100) LSAT substrates. During growth the substrates were held at 650°C and immersed in 5.0×10^{-7} torr (background pressure) of oxygen plus approx 10% ozone. Reflection high-energy electron diffraction (RHEED) intensity oscillations were monitored to ensure that complete SrO and TiO₂ monolayers were deposited alternately to form the SrTiO₃ films [110]. Although many samples were grown and characterized, the properties of a 500 Å-thick film grown on each substrate are compared below to show the effect of strain state on the ferroelectric properties of SrTiO₃.

X-ray diffraction scans show the out-of-plane lattice constant to be compressed ($a_{\perp} = 3.88 \pm 0.01 \text{ \AA}$) for the films grown on DyScO₃, and extended ($a_{\perp} = 3.93 \pm 0.01 \text{ \AA}$) for the films grown on LSAT, as expected from the boundary conditions imparted by the substrates. High-resolution X-ray diffraction measurements of the 500 Å-thick SrTiO₃ film grown on DyScO₃ reveal that its in-

plane lattice constant at room temperature is $a_{\parallel} = 3.935 \pm 0.002 \text{ \AA}$, corresponding to 0.8% biaxial tensile strain. Its out-of-plane lattice constant is $a_{\perp} = 3.8785 \pm 0.0005 \text{ \AA}$. Although somewhat beyond the critical thickness at which relaxation begins to occur, the rocking curve full-width at half-maximum (FWHM) of the (200) SrTiO₃ X-ray diffraction peak is 13 arcsec (0.004°), the narrowest ever reported for an epitaxial SrTiO₃ film. This, and other aspects of the X-ray scattering measurements, indicate that this film has a higher degree of uniformity and structural perfection than is typical of Ba_xSr_{1-x}TiO₃ films. The rocking curve FWHM of the (200) SrTiO₃ peak of the 500 Å-thick SrTiO₃ film grown on LSAT was also quite narrow, 21.5 arcsec (0.006°).

Measurements of the complex dielectric permittivity were performed on the SrTiO₃ films as a function of frequency (1-20 GHz), temperature (75-330 K), and direct current (d.c.) electric field ($\pm 40 \text{ V}$ across $6 \text{ }\mu\text{m}$) using interdigitated electrodes. The 1-2 μm -thick Ag interdigitated electrodes had 80 μm finger lengths and 6 μm finger gaps for the room-temperature measurements and 40 μm finger lengths and 12 μm finger gaps for the temperature-dependent measurements. The fingers were aligned parallel to the $\langle 110 \rangle$ in-plane directions of the SrTiO₃ films.

Figure 3.2 shows the temperature-dependent in-plane [109] ϵ_r and loss tangent, $\tan \delta$, of the 500 Å SrTiO₃/DyScO₃ film measured at 10 GHz. These data are from a device acting as a microwave varactor (a voltage-tunable capacitor) with 2:1 tuning, demonstrating the technological significance of these films. The curves agree well with expected Curie-Weiss behavior (inset) for a uniformly strained film, exhibiting a maximum in ϵ_r and $\tan \delta$ at $T_C \approx 293 \text{ K}$ and a Curie constant typical of displacive ferroelectrics. The peak ϵ_r of nearly 7,000 at 10 GHz is higher and the width of the peak in ϵ_r versus T is narrower than any value reported for Ba_{1-x}Sr_xTiO₃ thin films. By contrast, SrTiO₃/LSAT has a much lower dielectric constant and there is no peak in ϵ_r versus T . This result is fully consistent with the biaxial strain state causing the ferroelectric polarization to lie in the plane of the film for SrTiO₃ on DyScO₃, the direction sensed by the interdigitated electrodes, but lying out-of-plane of the SrTiO₃ grown on LSAT.

The observed T_C shift surpasses all prior records [90, 91] and gives credence to prior work on SrTiO₃/SrZrO₃ superlattices where ferroelectricity at room temperature in 8 nm-thick strained SrTiO₃ layers was assumed to be responsible for the dielectric properties of the composite superlattice [111]. Our results are consistent with a strain-induced phenomena; the possibility that minute

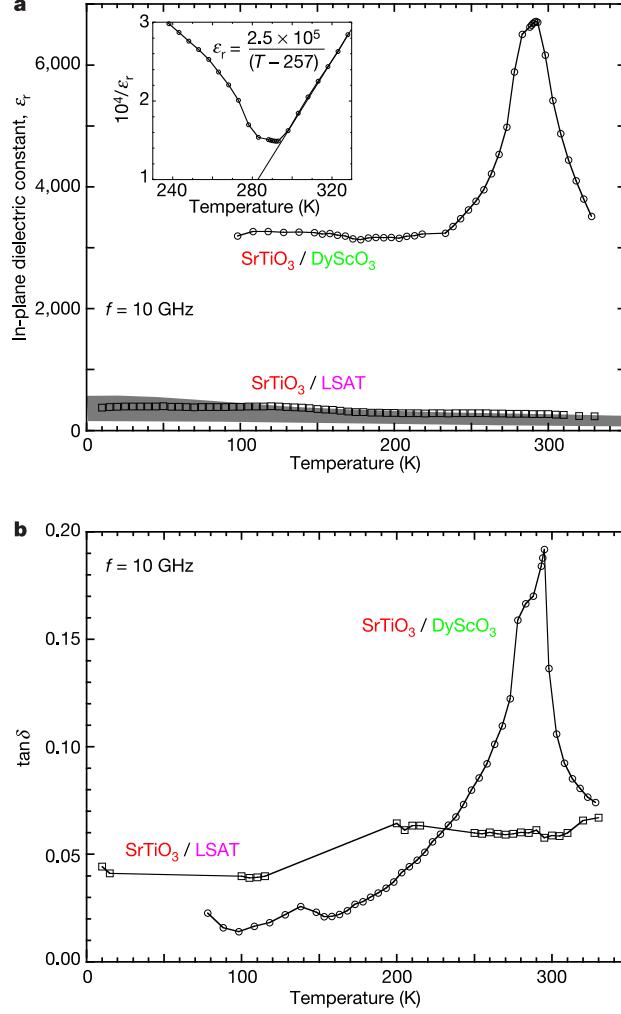


Figure 3.2: In-plane dielectric constant (ϵ_r) and dielectric loss ($\tan \delta$) in strained epitaxial SrTiO₃ films as a function of temperature and film thickness at a measurement frequency (f) of 10 GHz. (a), (b) Contrast of in-plane ϵ_r and $\tan \delta$, respectively, of 500 Å-thick SrTiO₃/(110) DyScO₃ and SrTiO₃/(100) LSAT epitaxial films. These films are under biaxial tensile and compressive strain, respectively. The peak in ϵ_r of about 7,000 and the simultaneous peak in $\tan \delta$ indicate that the T_C of SrTiO₃ under biaxial tension of $\epsilon_s = 0.008$ is about 293 K. The inset in (a) shows a Curie-Weiss fit to $1/\epsilon_r$. Owing to systemic errors involved in the measurement and calculation of the in-plane dielectric constant, the vertical scale in (a) may be off by as much as 10%. The shaded region in (a) corresponds to the expected value of the in-plane ϵ_r for a SrTiO₃ film commensurately strained to LSAT ($\epsilon_s = -0.009$), based on thermodynamic analysis and the range of relevant reported property coefficients for SrTiO₃ [101, 102].

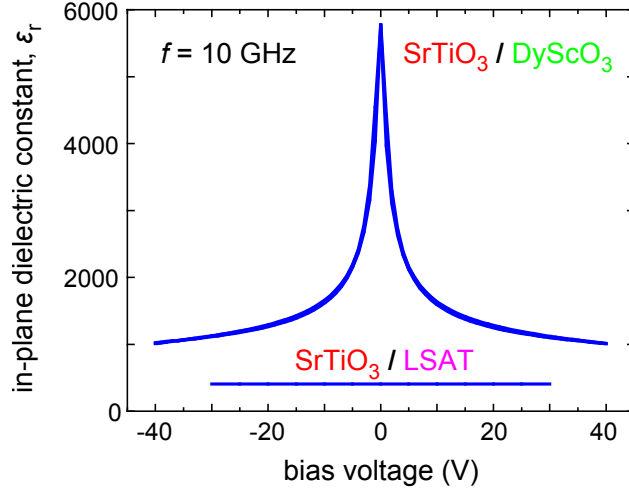


Figure 3.3: Dielectric tunability of the same 500 Å-thick SrTiO₃ films grown on DyScO₃ and LSAT as shown in Fig. 3.2. The film grown on DyScO₃ shows 82% tuning between 0 and ±40 V at room temperature, with slight hysteresis. The film grown on LSAT exhibits approximately 0% tunability with the application of ±40 V at room temperature.

Sc doping from the DyScO₃ substrate is in part responsible for the dramatic changes in dielectric behavior is also being investigated, although no such effects have ever been reported [112].

The remarkable field sensitivity of ϵ_r , which drops by 82% for an applied voltage of 40 V across 6 μm gaps, is shown in Figure 3.3. Such large tuning with modest fields makes these films applicable to a variety of microwave applications.

As is typical of ferroelectric thin films, their properties depend on thickness (Figure 3.4). These films, except the one marked “as-grown,” have been annealed at 700 °C for 1 h in 1 atm of air after growth. The drop in measured capacitance with SrTiO₃ film thickness is consistent with the ferroelectricity being in the SrTiO₃ film and not associated with the DyScO₃ substrate itself or a ferroelectric interfacial layer. The decrease in C_{max} (the height of the maximum of the capacitance as a function of temperature from the background capacitance value) with decreasing film thickness is a result of nonferroelectric (parasitic) contributions to the capacitance. Such behavior as a function of thickness is commonly seen in (Ba,Sr)TiO₃ films and is expected. From the partial capacitance approach [109], the thickness dependence of the total measured capacitance of the

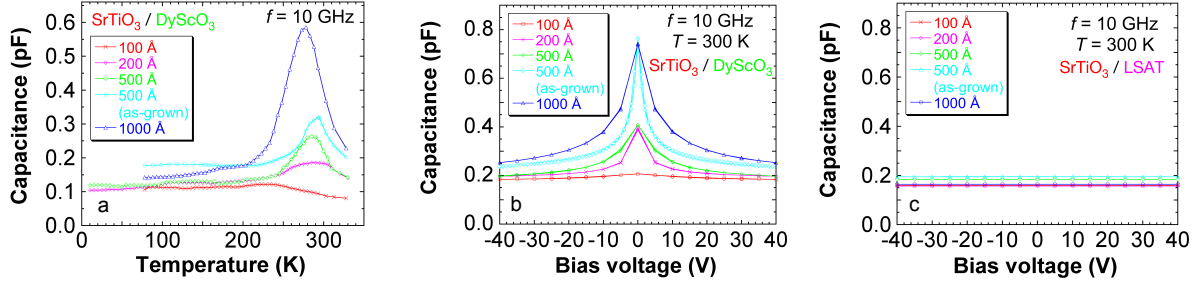


Figure 3.4: Thickness dependence of SrTiO₃ thin films. (a) The thickness dependence of the measured capacitance is shown for SrTiO₃/(110) DyScO₃ films of thickness 100 Å, 200 Å, 500 Å, and 1000 Å. (b) The thickness dependence of the dielectric tunability is shown for the same SrTiO₃/(110) DyScO₃ films shown in (a). (c) The thickness dependence of the dielectric tunability of SrTiO₃/(100) LSAT films with corresponding thicknesses and growth conditions to the SrTiO₃/DyScO₃ films is shown in (a) and (b). No tunability is seen in SrTiO₃/LSAT at room temperature, regardless of film thickness.

interdigitated capacitor is $C_{measured} \approx C_0 + \epsilon_0 (\epsilon_{film} - \epsilon_{sub}) Lh/s$, where ϵ_0 is the permittivity of free space; ϵ_{film} and ϵ_{sub} are the dielectric constants of the ferroelectric film and substrate, respectively; h is the thickness of the ferroelectric film; s and L are the width and total length of the slot between the electrodes, respectively; and C_0 is the contribution of the air and substrate to the total capacitance of the interdigitated capacitor, which is independent of h . This approximation is valid for $L \gg s \gg h$, which is the case for our interdigitated capacitors.

3.3 CSOM MEASUREMENTS

Optical measurements of the ferroelectric polarization at microwave driving fields were performed using time-resolved confocal scanning optical microscopy (TR-CSOM) [113, 65]. The in-phase and out-of-phase response at the microwave driving frequency correspond to the real and imaginary parts of the polar contribution to the dielectric response at that frequency.

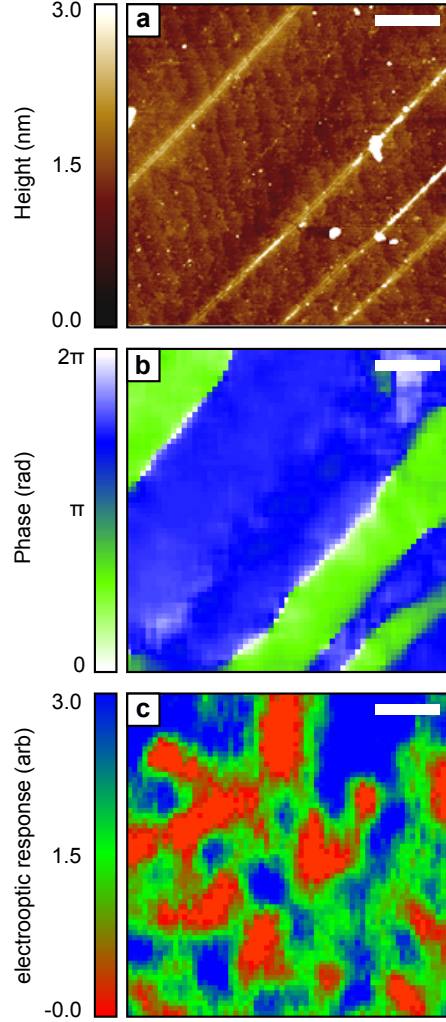


Figure 3.5: Comparison of the morphology and microwave electro-optic response of tunable dielectric films at room temperature (just above T_C). The scale bars are $1\ \mu\text{m}$ for all images. (a) An AFM image of the same $500\ \text{\AA}$ -thick SrTiO_3 film grown on DyScO_3 shown in Fig. 3.2. In addition to unit-cell-high steps on the surface of the SrTiO_3 film, four diagonal linear features that protrude $\sim 50\ \text{\AA}$ from the surface are evident. Similar surface imperfections are seen on the bare substrates, suggesting that they are associated with polishing. (b) Image of the phase shift between the electro-optic response and microwave driving field ($3.27\ \text{GHz}$) for the same $\text{SrTiO}_3/\text{DyScO}_3$ film (but not the identical region) as in (a), revealing uniform in-plane polarization separated by clear boundaries like the ones observed by AFM. (c) TR-CSOM image (at one time delay) of a typical epitaxial $\text{Ba}_{0.5}\text{Sr}_{0.5}\text{TiO}_3/\text{MgO}$ film at $2.06\ \text{GHz}$, showing inhomogeneous in-plane polarization.

Figure 3.5b shows a typical TR-CSOM image of the phase shift between linear electro-optic response and a microwave driving field (3.27 GHz), measured for the 500 Å SrTiO₃/DyScO₃ film. The electro-optic phase is computed from a fit to the temporal response at various points in the microwave drive cycle [113, 65]. Most striking are the large regions in which the phase is essentially uniform, separated by sharp boundaries at which the phase changes by 90° or 180°. These boundaries correspond to features observed by atomic force microscopy (AFM) on the film (Figure 3.5a) as well as on bare DyScO₃ substrates, and may be due to surface imperfections that break the in-plane symmetry and produce an easy axis for the SrTiO₃ films. For sake of comparison, Figure 3.5c shows a typical TR-CSOM image (at a fixed time delay) for a ferroelectric film (Ba_{0.5}Sr_{0.5}TiO₃/MgO) that has not been strain-engineered. The strong fluctuations in the electro-optic response on sub-micrometer scales are typical of films that are inhomogeneously strained.

3.4 CONCLUSIONS

The remarkable dielectric properties of SrTiO₃, while recognized for many decades, have previously only been accessible in the bulk and at cryogenic temperatures. Efforts to shape the properties of ferroelectric films have been restricted by available substrates. Through controlled substrate engineering, often overlooked in the growth of thin films, we have achieved ϵ_r and tunability at room temperature in SrTiO₃ films with properties comparable to bulk SrTiO₃ at cryogenic temperatures. In addition to radically enhanced dielectric properties, we expect other ferroelectric properties (including pyroelectricity, piezoelectricity, and nonlinear optical effects) of SrTiO₃ to be accessible at room temperature through the application of appropriate homogeneous strain.

4.0 LOCALIZED MICROWAVE RESONANCES IN STRAINED STO

¹ Local frequency-dependent polar dynamics of strained SrTiO₃ films grown on DyScO₃ are investigated using time-resolved confocal scanning optical microscopy. Spectroscopic information is obtained with < 1 μm spatial resolution over the frequency range 2-4 GHz. Most of the DyScO₃ film is found to be spatially homogeneous, in contrast to relaxed films. A strong correlation between spatial and spectral homogeneity is revealed. In addition, resonant structures are discovered that are localized both in space and in frequency.

4.1 INTRODUCTION

Understanding the relationship between the polar structure and dynamic response of ferroelectrics is critical for the development of integrated devices. There are many factors which can produce dielectric dispersion in these systems. Some are intrinsic to the phase transition itself, while others depend on the existence of domain structures and their dispersive properties. Arlt *et al.* have predicted that stripe domain patterns in bulk BaTiO₃ single crystals will produce strong dispersion in the GHz regime [115]. Similarly, polar complexes observed in relaxor ferroelectrics have been identified by their characteristic frequency response [116, 117]. McNeal and coworkers have linked the domain state of BaTiO₃ (by way of grain and particle size) with microwave resonances [118]. The relevant length scales for ferroelectrics span an unusually wide range, from the atomic [119] to the crystal dimension itself [120], and frequency responses can also span from quasi-dc (~ 1 Hz) [121] to the ferroelectric soft mode (~ 10¹¹ Hz) [122, 123]. Understanding how polar structure at a given length scale relates to the dynamic response at a given frequency scale can shed light on

¹Originally published in a different form in *Applied Physics Letters* [114].

basic issues for device fabrication such as the fundamental limitations for domain switching and mechanisms of microwave dielectric loss.

The dielectric constant of capacitors fabricated from ferroelectric thin films can be changed with modest applied DC voltages, making them suitable for tunable microwave devices such as phase shifters [124] and filters [125]. A widely investigated material system is $\text{Ba}_x\text{Sr}_{1-x}\text{TiO}_3$, whose Curie temperature T_C can be varied from nearly 0 K for pure SrTiO_3 ($x = 0$) to 400 K for pure BaTiO_3 ($x = 1$) [85]. For thin films grown under most conditions, non-uniform strain as well as stoichiometry fluctuations can lead to an inhomogeneous broadening of T_C over hundreds of degrees. The growth of high-quality ferroelectric films is complicated by a lack of suitably lattice matched substrates. Recently, bulk single crystals of DyScO_3 have been synthesized and used to grow uniformly strained SrTiO_3 films by molecular beam epitaxy [110, 47]. The large biaxial tensile strain in this system results in ferroelectric behavior at room temperature [47, 126].

Here we describe local spectroscopic investigations of polar dynamics in a 500 Å-thick SrTiO_3 film grown on DyScO_3 [47]. We have developed an extension of time-resolved confocal scanning optical microscopy (TR-CSOM) that enables local polar dynamics to be measured as a function of frequency as well as spatial location. Using the electro-optic response to reveal polar dynamics in the SrTiO_3 film, we identify localized resonant features associated with the periodic domain boundaries. While the domain structure appears to be templated by the DyScO_3 substrate, the existence of these resonant features represent the first direct experimental evidence linking microwave resonances to domain structures.

4.2 SPECTROSCOPIC MICROWAVE CSOM

A schematic of the experiment is shown in Figure 4.1. An ultrafast (~ 120 fs) mode-locked Ti:sapphire laser is used to generate both the microwave electrical “pump” field and the optical probe pulse. The microwave pump signal is derived from a phase-locked oscillator (PLO) that is locked to a high harmonic of the repetition rate of the laser, $f_1 = 76$ MHz. The electrical signal is applied to the SrTiO_3 film using Ag interdigitated electrodes deposited on the film surface (gap width $d = 10$ μm), and are oriented parallel to the $\langle 110 \rangle$ STO direction. Details about sample

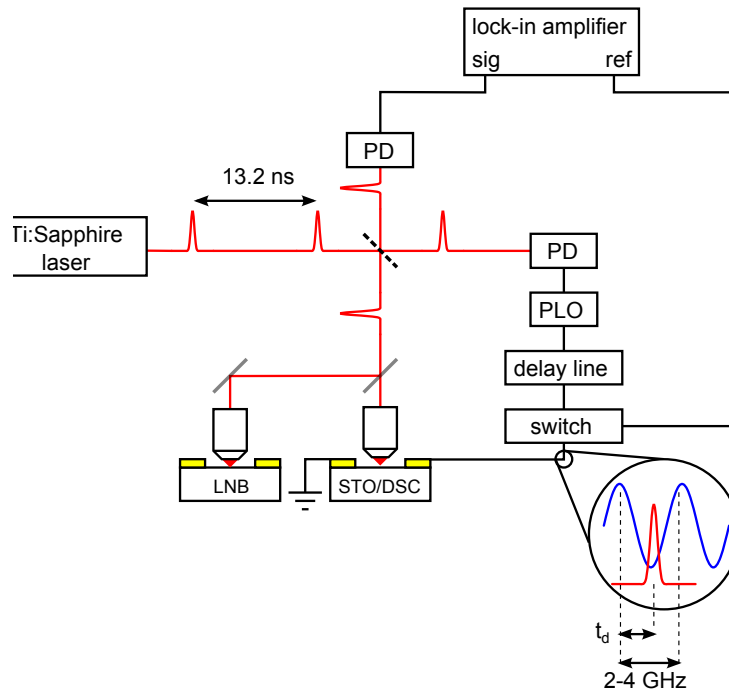


Figure 4.1: Pulses from a mode-locked Ti:Sapphire laser are sampled by a fast photodiode (PD) that provides a reference for a microwave-frequency phase-locked oscillator (PLO) whose frequency is locked to a high harmonic of the fundamental repetition rate ($f_1 = 76$ MHz) of the laser. This microwave signal is then applied to the sample by using interdigitated silver electrodes. The microwave signal at the sample is delayed in time relative to the incoming laser pulses using a programmable delay line. The samples are raster scanned relative to the microscope objective with a piezoelectric stage to produce images. A single-crystal LiNbO_3 sample is used to produce a reference phase at the different frequencies.

preparation can be found elsewhere [110, 47]. The laser pulses, focused to a diffraction-limited spot using a microscope objective ($NA = 0.85$), probe the electro-optic response at a fixed phase of the microwave signal. The relative phase between electrical and optical signals is controlled using an electrical delay line. The amplitude of the microwave field is modulated at a low frequency (~ 1 kHz) and the resulting electro-optic signal is detected using an optical bridge and lock-in amplifier [113]. The reflected polarization of the laser light probes the electro-optic response. The temporal response provides direct information about local polar contributions to the microwave permittivity of the film [86].

TR-CSOM images are acquired by raster scanning the sample relative to the laser spot. Images are taken at ten different time delays t_d (step size $\delta t = 50$ ps) for 27 different microwave frequencies $f_n = n f_1$, $26 \leq n \leq 53$, spanning the range 2-4 GHz. An entire scan of frequencies, time delays, and spatial locations takes approximately 12 hours to complete; thermal control of the TR-CSOM apparatus is maintained to within $T \sim 0.02$ K in order to stabilize the images sufficiently. The experiment is performed at room temperature (295 K), which is above T_C in this sample. Post-processing of the images is also performed to account for residual drift over the acquisition period.

There is no intrinsic method for defining the absolute phase of the incident microwave field relative to the optical probe, and the measured phase changes in an uncontrolled way from one microwave frequency to another. To produce a stable reference phase, TR-CSOM measurements were also taken under identical conditions on a single-crystal LiNbO_3 reference sample, located several millimeters away from and connected in parallel with the SrTiO_3 film. The phase of the linear electro-optic response of the LiNbO_3 , assumed to be constant over the frequency range explored, is used to define a reference phase for the frequency-dependent SrTiO_3 measurements.

4.3 DATA ANALYSIS

The polar response of the SrTiO_3 film is well described by Fourier components at angular driving frequency $\omega_n = 2\pi f_n$ and second harmonic $2\omega_n$ [65]:

$$S(t) = S_0 + F_1 \cos(\omega_n t) + F_2 \sin(\omega_n t) + P_1 \cos(2\omega_n t) + P_2 \sin(2\omega_n t). \quad (4.1)$$

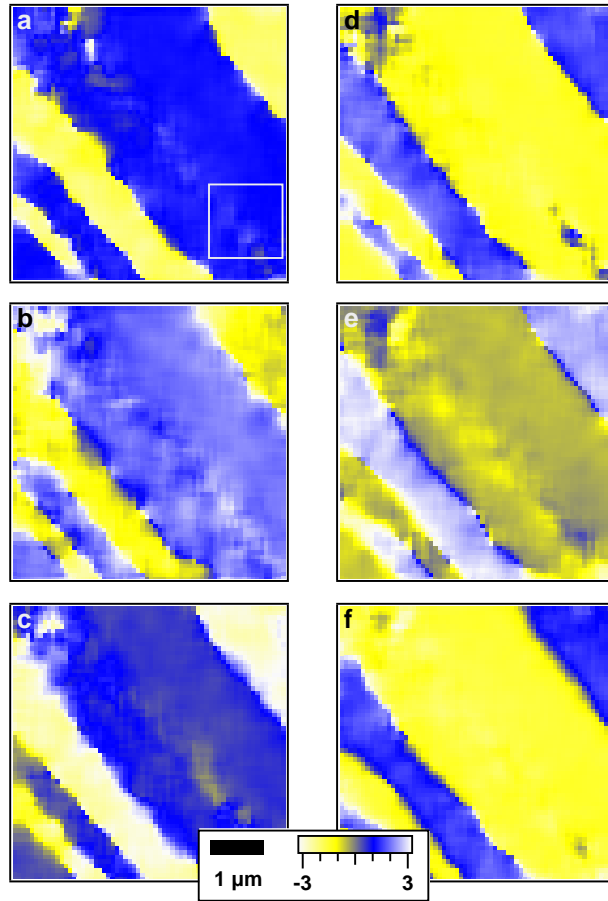


Figure 4.2: Phase of ferroelectric response, φ , plotted as a function of location in the sample for six microwave driving frequencies. (a) 2.2 GHz, (b) 2.43 GHz, (c) 2.74 GHz, (d) 2.96 GHz, (e) 3.27 GHz, (f) 3.5 GHz.

At each driving frequency, the sequence of images at various time delays is used to produce a fit to Eq. 4.1 at each spatial location. The result is an image of each of the four Fourier coefficients, $\{F_1, F_2, P_1, P_2\}$. This analysis is performed for each of the 27 discrete frequencies investigated.

Figure 4.2 shows images of the phase at six representative driving frequencies. The large uniform regions visible in Figure 4.2 are characteristic of the high quality of the SrTiO₃ film, and are observed only with uniformly strained samples grown on DyScO₃ substrates [47]. The stripes correspond to regions that are responding uniformly over the entire frequency range investigated. Alternating stripes differ in phase by approximately π , which is consistent with the existence of a domain wall boundary separating them. These domain boundary regions exhibit a microwave response that is much less uniform, and which exhibit dispersive behavior that is localized in space and in frequency.

To illustrate the ferroelectric response within domains and near the domain walls, we analyze subsections from the datasets shown in the boxed region in Figure 4.2a. Figure 4.3 shows vector field plots of the linear electro-optic response at two microwave frequencies and two different dc bias voltages. Arrows are colored according to the magnitude of the response, while their direction indicates the local phase relative to the LiNbO₃ single crystal. Regions of the sample that are far from the domain boundaries have a uniform response, irrespective of applied frequency or DC bias. However, select regions that are closer to the domain boundaries show significant local dispersion when a DC bias is applied.

To further investigate the local dynamics, the complex electro-optic response $\mathbf{F} = F_1 + iF_2$ is compared for several regions of the sample. In Figure 4.4, the linear electro-optic response for the 16 sub-regions identified in Figure 4.3 are averaged and plotted as a function of applied electric field frequency. Highly dispersive responses are observed at 2.4 GHz and 3.5 GHz. When a DC bias is applied, the dispersion increases at 2.4 GHz while decreasing somewhat at 3.5 GHz.

4.4 CONCLUSIONS

A typical characteristic of relaxor ferroelectrics is their dielectric dispersion characteristics, many of which can be understood by sound emission due to domain walls vibration [127]. Biegalski *et al.*

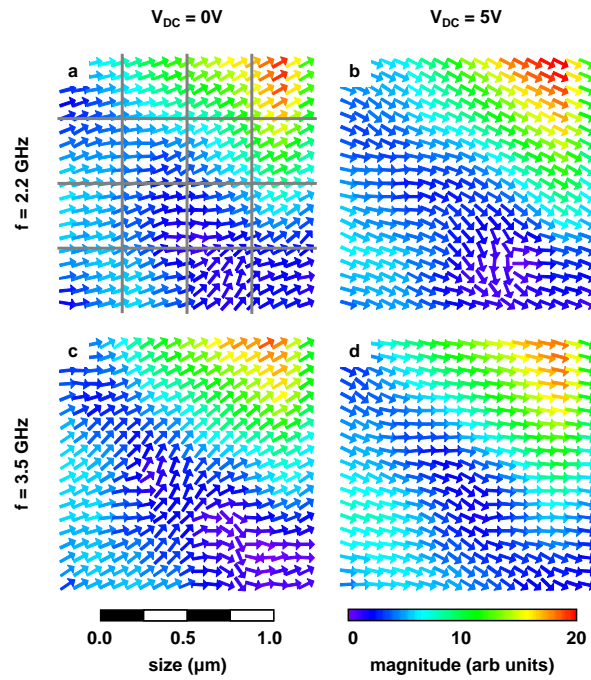


Figure 4.3: Vector plots showing magnitude (color) and phase (angle) in the region identified in Fig. 4.2 (a). (a) and (b) compare DC biases of 0 V and 5 V, respectively, at 2.2 GHz. (c) and (d) compare DC biases at 3.5 GHz

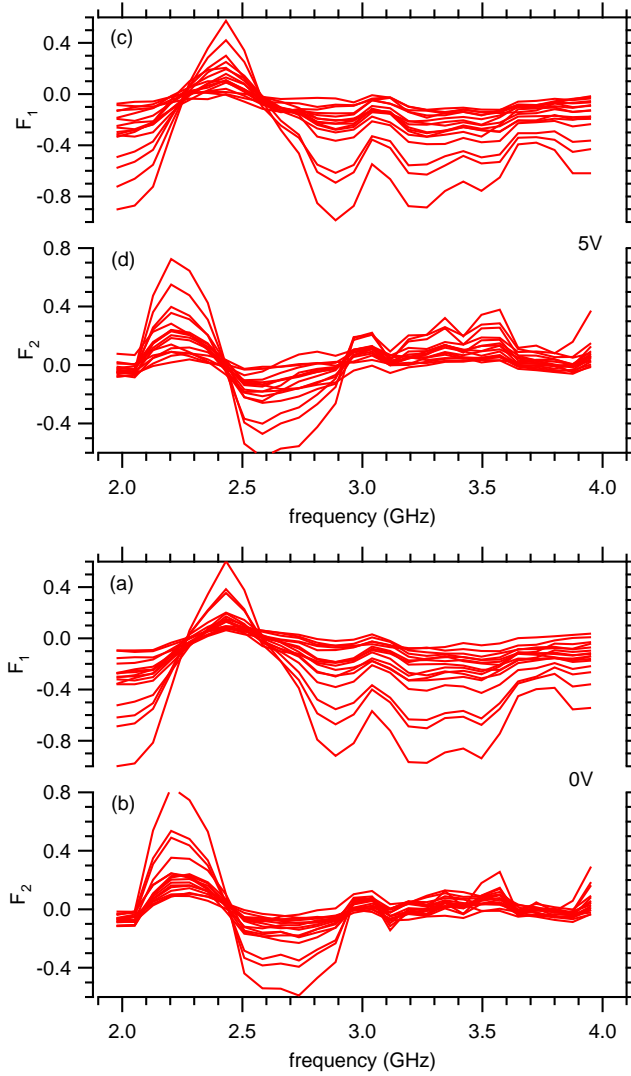


Figure 4.4: In- and out-of-phase components of ferroelectric response plotted as a function of driving field frequency. Curves are taken from the area shown in Fig. 4.3 and each line is an average over each of the 16 sub-regions identified in Fig. 4.3(a).

have shown that these SrTiO₃/DyScO₃ films show relaxor behavior in this frequency range [128]. Additionally, the periodic domain structures observed by TR-CSOM may produce shear waves that interfere constructively or destructively, depending on the driving frequency [115]. In addition to providing evidence of uniform ferroelectric response, the stripe domain pattern we observe could also be the source of the resonances we detect near the domain boundaries and within the domains themselves.

5.0 THREE-DIMENSIONAL POLARIZATION IMAGING OF BST:MGO

¹ The dielectric tuning and loss of (Ba,Sr)TiO₃:MgO bulk composites depend strongly on the connectivity and interaction among the two phases. To investigate this relationship, the polar structure and dynamics of these composites is mapped as a function of space and time using a pair of three-dimensional probes: second-harmonic confocal scanning optical microscopy (SH-CSOM), which maps ferroelectric polarization in three dimensions, and time-resolved scanning optical microscopy (TR-CSOM), which maps polarization dynamics along two spatial dimensions and one time dimension. SH-CSOM measurements reveal a high degree of homogeneity within the (Ba,Sr)TiO₃ regions, while TR-CSOM measurements indicate that topologically connected regions respond with a spatially uniform phase.

5.1 INTRODUCTION

Over the past decade, a variety of ferroelectric materials (including (Ba,Sr)TiO₃, (Pb,Sr)TiO₃, SrTiO₃, KTaO₃, Cd₂Nb₂O₇, etc.) have been investigated for frequency-agile microwave electronics (FAME). It is highly desirable that materials selected for such devices have suitable dielectric constants and high tunability figure of merit defined by $\kappa = (\epsilon_0 - \epsilon_E) / (\epsilon_0 \tan \delta)$, where $\tan \delta$ is the dielectric loss, and ϵ_0 and ϵ_E are the dielectric permittivity at zero and E electric fields. Many of the materials being investigated possess spatially non-uniform structure and properties, and hence it is important to understand how local ferroelectric properties (i.e., polarization state, local permittivity) correlate with the figure of merit, so that improvements in device performance can be made.

¹Originally published in a different form in *Applied Physics Letters* [129].

Of all the materials investigated for FAME applications, (Ba,Sr)TiO₃ (BST) has received the most attention [130, 131, 132, 133] due to its intrinsic high dielectric tunability and capacity to optimize the figure of merit at a given temperature by changing the Ba/Sr ratio. Most studies of BST for FAME applications have been carried out in thin films [130, 131]. For bulk applications in microwave phase shifters, varactors, etc., lower dielectric constants than are achievable with BST are required. For this reason, several bulk composites have been developed using BST and MgO [132, 133]. The relatively low dielectric constant and loss of MgO helps to reduce the effective dielectric constant and loss of the composite while maintaining respectable tunability. In these composites, the connectivity of the two phases plays an important role in the reproducibility of the properties.

5.2 SECOND-HARMONIC CSOM

Optical techniques have long been used to image properties of interest in ferroelectric materials. Electro-optic contrast in ferroelectrics has been exploited since the discovery of BaTiO₃ [134], and has more recently been refined with advances in laser and optical technologies [86]. Imaging is typically performed by collecting information as a function of two spatial dimensions. To better understand the properties of bulk materials and composites, adding a third dimension is especially helpful. With second-harmonic confocal scanning optical microscopy (SH-CSOM) it is possible to probe for a ferroelectric response within the bulk of the material. Alternatively, the temporal response of a material can be regarded as a third dimension. Time-resolved confocal scanning optical microscopy (TR-CSOM) substitutes time for the third dimension, enabling polar dynamics to be recorded within a single microwave cycle. Both methods provide important and complementary information about the nature of dielectric tuning in these composite single crystal materials.

Three-dimensional maps of the polar response of single crystal composites of Ba_{0.6}Sr_{0.4}TiO₃:MgO are obtained using both SH-CSOM and TR-CSOM. A Ba_{0.6}Sr_{0.4}TiO₃ composition, with T_C close to room temperature, is selected for these studies. Single crystals of BST:MgO are grown by the laser heated pedestal growth (LHPG) technique. The details of the growth experiments are reported elsewhere [135]. The *c*-axis oriented composite crystal plates are cut and polished from

the LHPG grown crystals. Surfaces of the plates are polished using 0.1 μm size alumina powder and annealed at 500°C in order to reduce the mechanical surface strain caused during the polishing.

Figure 5.1a shows an SEM image of a typical sample used for these experiments. Energy dispersive spectroscopy (EDS) of individual grains shows the chemical constituents of the grain chemistry. Figure 5.1b reveals negligible intermixing of the BST and MgO components [136]. Silver electrodes are deposited on the surface of the crystal, with a gap spacing of 30 μm .

The second harmonic response of a material is highly sensitive to the breaking of inversion symmetry [137], and has been exploited in diverse applications, from probing living cells [138] to semiconductor quantum dots [139]. Second harmonic generation has been applied to ferroelectric materials to image ferroelectric domain walls in KTiOPO_4 (KTP), LiNbO_3 [140], and BaTiO_3 [141]; to distinguish between surface and bulk effects in SrTiO_3 [142]; and to produce three dimensional images in lithium triborate [143].

Here SH-CSOM is used to collect second harmonic light as a function of three spatial dimensions for the BST:MgO composite. Light from a mode-locked Ti: sapphire laser (wavelength $\lambda = 800\text{ nm}$) passes through a spatial filter and is focused with a high numerical aperture microscope objective ($NA = 0.8$) to a $V = 0.5 \times 0.5 \times 1.0\ \mu\text{m}^3$ region within the sample volume (Figure 5.3a). The high peak intensity of the ultrashort light pulse ($\sim 130\text{ fs}$ pulse duration) produces a strong second-harmonic response in the BST, locally generating light with wavelength $\lambda_{SH} = 400\text{ nm}$. The microscope objective collects both the reflected IR light and SH light; an ultrafast mirror and shortwave pass filter allow only the frequency doubled light to be detected by a near-ultraviolet sensitive avalanche photodiode (APD). By scanning the laser spot over a volume of sample a three-dimensional representation of the ferroelectric polarization in BST: MgO composite is produced.

A series of SH-CSOM images is shown in Figures 5.3b and c. The bright regions correspond to areas in which a large amount of SH light is collected, corresponding to volumes in which BST is present. MgO possesses a center of symmetry and therefore no SH light is produced; dark areas therefore correspond to volumes containing MgO. Imaging the SH response of the material allows us to probe the sample at different depths, and therefore produce a three-dimensional polar image of the sample. Figure 5.3d shows a three-dimensional rendering [144] of the second harmonic

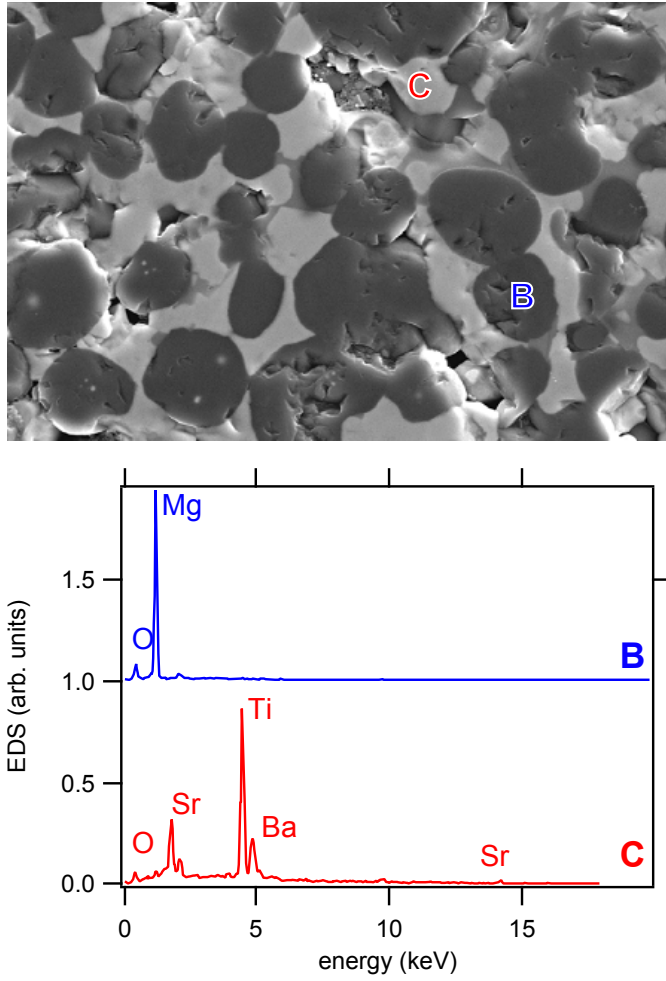


Figure 5.1: (a) SEM image showing grain distribution of BST (light) and MgO (dark). (b) EDS analysis of MgO and BST grains, showing negligible intermixing. Curve B offset for clarity.

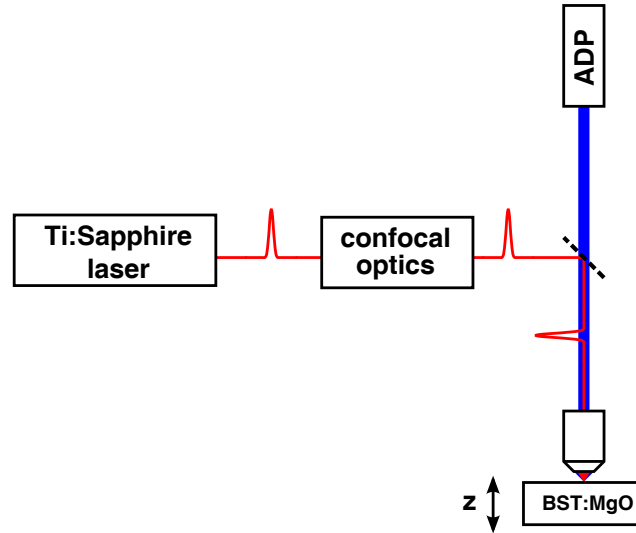


Figure 5.2: (a) Schematic of SH-CSOM technique.

response, which gives a clearer view of the distinct BST and MgO regions. The solid objects in the rendering are areas where there exists a second harmonic response, namely, regions of BST.

TR-CSOM maps the dynamic response of ferroelectric materials to applied microwave frequency electric fields [113]. A diagram of the experiment is shown in Figure 5.4. The same confocal setup used for SH-CSOM is used to focus 800 nm light pulses from the Ti:Sapphire laser to a diffraction-limited spot on the sample surface. A sampled portion of the beam is used to generate a reference for a phase-locked oscillator (PLO). The PLO produces electric fields between 2 – 4 GHz that have a fixed phase with respect to the laser pulses. By scanning an electrical delay line, the time-resolved images of the electro-optic response of the sample are obtained.

Figures 5.5a and b show TR-CSOM images at two representative time delays, 100 ps and 400 ps, respectively. The temporal response for two distinct BST grains in the BST:MgO composite is shown in Figure 5.5c. Note that the responses of the two grains are approximately out of phase by 180° . This out of phase relationship indicates that the static polarization of the two domains is approximately antiparallel: the application of an electric field causes the polarization to increase in one region and decrease in the other. The polar response at each spatial location in a time-sequence of TR-CSOM images can be fit to extract the Fourier coefficients of the ferroelectric response [65].

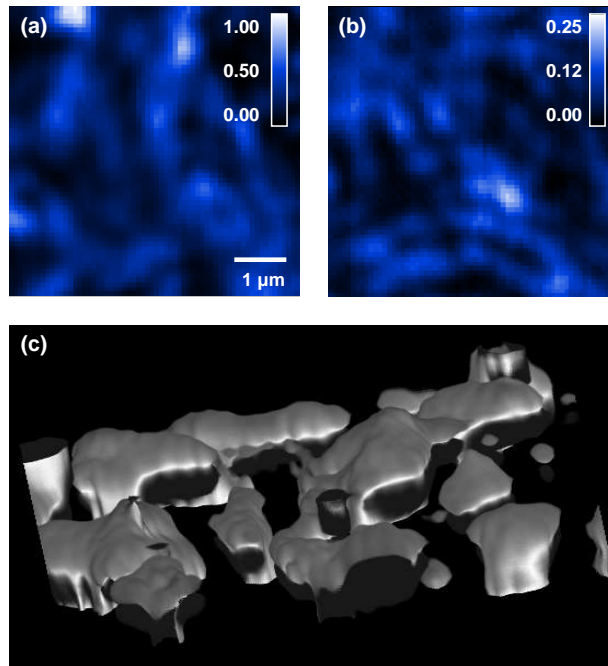


Figure 5.3: (a-b) SH-CSOM images acquired at depths 1.6 μm and 4.0 μm below the surface. The bright regions correspond to areas with strong SH collected, and correspond to the BST grains, while the dark regions correspond to MgO. (c) Three-dimensional rendering of SH response of BST: MgO taken over an $8.8 \times 8.8 \times 4.0 \mu\text{m}^3$ volume using confocal sectioning. Solid objects are BST while transparent regions are MgO.

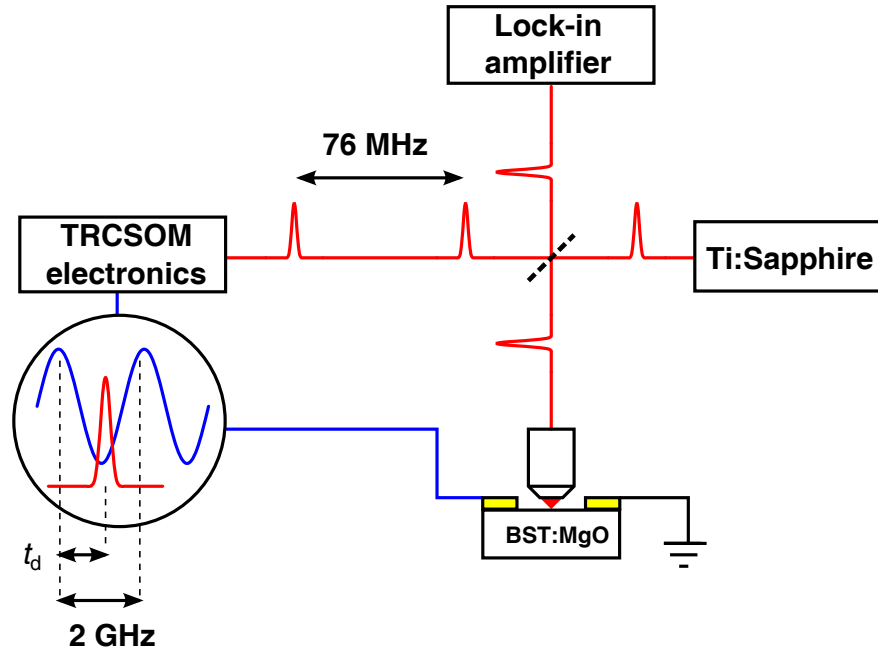


Figure 5.4: Diagram of TRCSOM experiment.

Images of the magnitude and phase of the Fourier coefficients are shown in Figures 5.5d and e, respectively. The length scales over which polarization is uniform in magnitude correspond roughly to those imaged by SH-CSOM. Hence, the BST regions appear to be either few- or single-domain, based on the spatial uniformity of the microwave response.

5.3 CONCLUSIONS

Both SH-CSOM and TR-CSOM images of BST: MgO composite show evidence of distinct BST and MgO regions and the TR-CSOM images illustrate that the ferroelectric polarization behaves nearly uniformly within individual grains at microwave frequencies. In addition, there is negligible microwave dispersion within the grains, in contrast to observations made for BST thin films [65]. While the polarization direction between grains appears random, determined likely by local shape

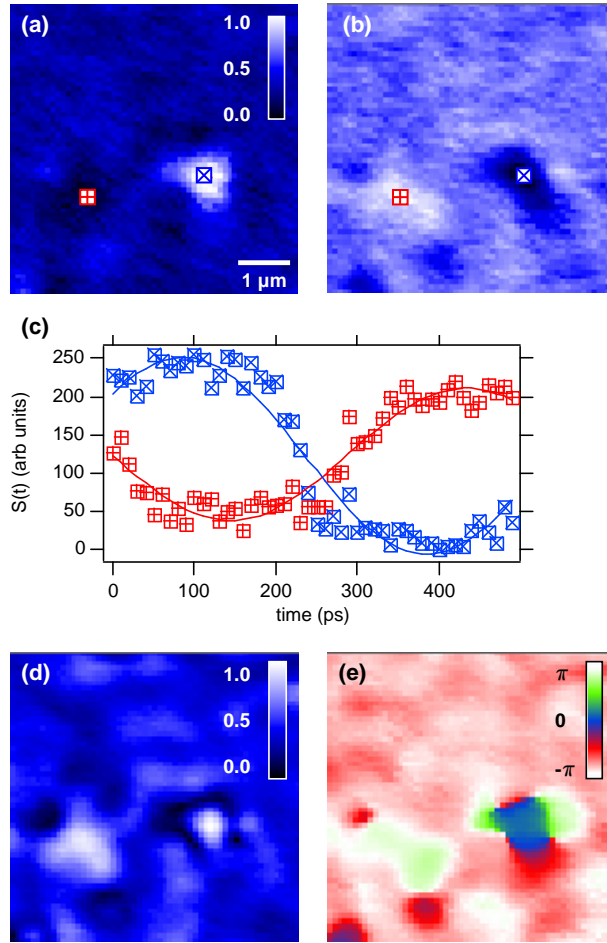


Figure 5.5: (a-b) TR-CSOM images of BST: MgO at two distinct time delays $t_D = 100$ ps (a) and $t_D = 400$ ps (b). (c) TR-CSOM curves, $S(t)$ obtained at two locations indicated by square markers in (a-b), corresponding to two distinct BST grains. The temporal response indicates an out-of-phase relationships between the two grains. (d-e) Spatial maps of the magnitude and phase of the TR-CSOM response.

considerations and differential thermal contraction after growth, the MgO appears to have little impact on the microwave properties of the BST, thus fulfilling its requirements as a low-loss, low dielectric constant spacer material.

6.0 GIGAHERTZ OPTICAL SPIN TRANSCEIVER (GHOST)

¹ We present a time-resolved optical technique to measure electron spin dynamics with GHz dynamical bandwidth, transform-limited spectral selectivity, and phase-sensitive (lock-in) detection. Use of a continuous-wave (CW) laser and fast optical bridge enables greatly improved signal-to-noise characteristics compared to traditional optical sampling (pump-probe) techniques. We demonstrate the technique with a measurement of GHz-spin precession in *n*-GaAs. This approach may be applicable to other physical systems where stroboscopic techniques cannot be used because of either noise or spectral limitations.

6.1 INTRODUCTION

Electron spin in semiconductors [146] has been extensively measured using a variety of techniques including Kerr rotation (KR) [147], Hanle effect [148], electrical detection with ferromagnetic electrodes [149], and noise spectroscopy [150]. The spin dynamics in these systems have generally been studied using stroboscopic techniques which utilize the temporal properties of mode-locked [151] or pulsed diode lasers [152].

Ultrafast spectroscopy provides exceptional time resolution, but there are drawbacks to the stroboscopic pump-probe approach for some investigations. Ultrashort optical pulses are limited in their spectral resolution by the time-energy uncertainty relation ($\Delta E \cdot \Delta t \geq \hbar$). High spectral resolution becomes particularly important if one is interested in probing the dynamics of a system with sharp optical transitions, such as semiconductor quantum dots or defect states, without influence or disturbance from nearby systems. For example, pulses from a Ti:Sapphire laser with

¹Originally published in a different form in *Optics Express* [145].

150 fs pulsewidth at $\lambda = 750$ nm will have a transform-limited spectral width of $\Delta E \sim 12$ meV; by contrast, the linewidth of a typical quantum dot is less than 40 μ eV [60]. A second, less fundamental limitation relates to acquisition of dynamics over long time scales comparable to the repetition rate for the experiment. Mechanical delay lines become cumbersome for pump-probe delays > 5 ns; acquisition speed is limited by the rate at which these delay lines can be scanned. Other optical techniques that infer dynamics from continuous wave optical sources, for example fluorescence correlation spectroscopy [153], lack phase information that may be critical for some investigations.

While many of these limitations can be remedied by suitable choice of lasers, e.g., pulsed laser diodes with narrower spectra [152] and asynchronous optical sampling to address limitations associated with mechanical delay lines [154], there is a more subtle effect that impacts the signal-to-noise ratio (SNR) in stroboscopic or sampling experiments. In a typical pump-probe experiment the dynamics are sampled only for a small fraction of the interval in which the dynamics takes place. This fraction, $\Delta t/T$ (where Δt is the sampling time and T is the period of the pulsed laser system), undersamples both the signal and any intrinsic noise (other than shot noise). In order to achieve an optimal SNR, it is advantageous to sample (hence average) the intrinsic noise as much as possible.

For purposes of illustration, one can assume that the signal of interest $S(t)$ is periodic with period T and is sampled by an optical probe with intensity profile $I(t)$. One may consider two limiting cases where the optical profile is either constant ($I(t) = I_0$) or pulsed with a width t_0 ($I(t) = I_0 \cdot T/t_0$, $0 < t < t_0$, and zero otherwise). Assuming that the intensity fluctuations in the optical signal are only limited by shot noise, one can model the physical system as

$$S(t) = S_0(t) + \eta(t), \tag{6.1}$$

where $S_0(t)$ is a noise-free periodic function and $\eta(t)$ represents an intrinsic noise term (assumed here to be white: $\langle \eta(t) \cdot \eta(0) \rangle = \delta(t)$). The system is sampled by a shot-noise limited photon field $I(t)$, and the measured signal consists of averaging the product $S(t) \cdot I(t)$ over many periods. Comparison of the two results (Figure 6.1a) for the same number of measurement photons shows that continuous measurement results in a maximum SNR improvement $\sim (T/\Delta t)^{1/2}$ over sampling methods, for the case where intrinsic noise dominates over shot noise (Figure 6.1b).

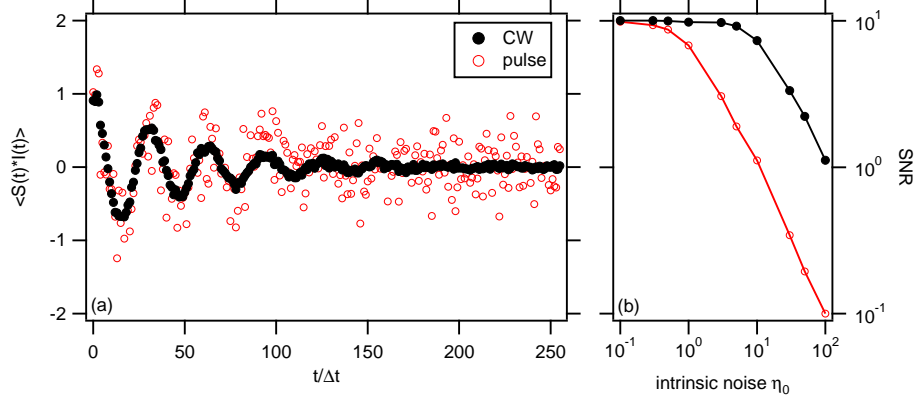


Figure 6.1: Simulation of noise reduction when comparing a sampling technique (pulsed probe) with a continuous detection one (CW probe): (a) Averaged data for CW and stroboscopic acquisition. Here $S_0(t) = \exp(-T \cdot t) \cos(\omega \cdot t)$. The intrinsic noise is $\eta_0 = 0.3$ and the pulse width is $t_0 = 1$. (b) Comparison of SNR for CW and stroboscopic acquisition.

Here we report on a realization of this approach to time-resolved optical detection based on the continuous detection method outlined above. Our approach utilizes a CW laser and high-bandwidth balanced photoreceiver to measure spin dynamics in semiconductors with superior noise characteristics compared to pump-probe (sampling) techniques. The functionality of this detection scheme is demonstrated by investigating spin dynamics in a well-studied sample, *n*-GaAs [151].

6.2 EXPERIMENTAL SET-UP

In the investigation of spin dynamics in semiconductors, the Kerr effect provides direct information about the spin orientation. Upon reflection from a magnetic material, a linearly polarized laser will have its polarization direction rotated by an amount proportional to the magnetic moment along the propagation direction [155]. A diagram of our experiment is shown in Fig. 6.2. A pulsed laser is used to create a population of spin polarized electrons and a continuous-wave laser monitors the

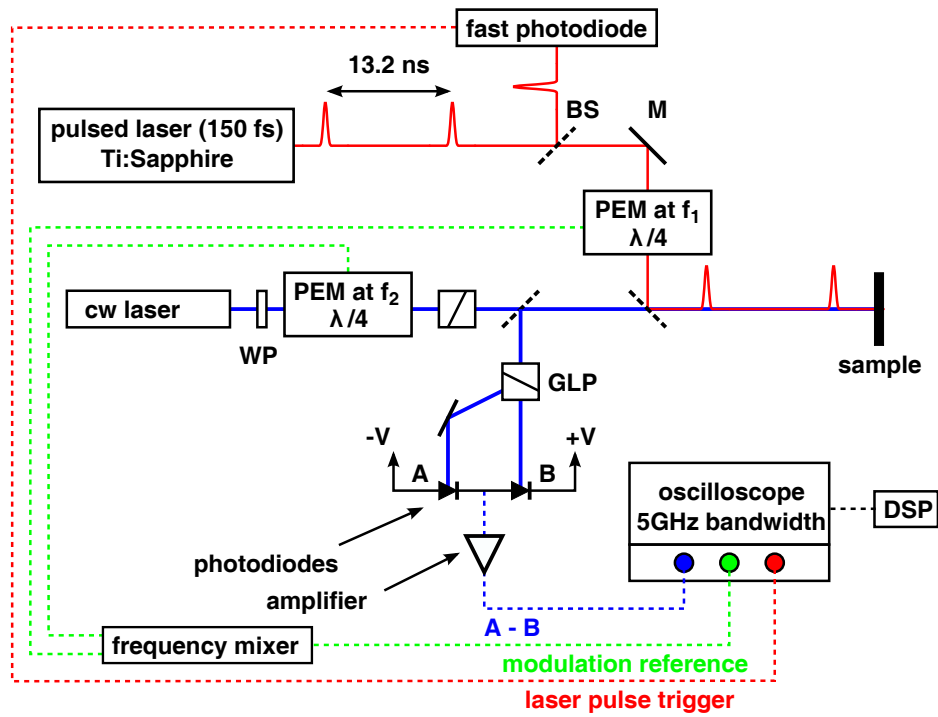


Figure 6.2: Schematic drawing of the experimental setup for the detection of electron spin coherence in semiconductors. (GLP) Glan-Laser polarizer; (WP) quarter wavelength plate; (PEM) photoelastic modulators; (BS) beamsplitters; (M) mirrors; (DSP) digital signal processor.

spin polarization by using the Kerr effect. In order to perform lock-in detection, the pump beam is modulated in helicity at frequency f_1 by a photoelastic modulator (Hinds PEM-90) to alternately create majority spin up and spin down electrons. The probe beam is intensity modulated with a PEM at frequency f_2 . By tuning the probe wavelength one can measure the wavelength dependence of the Kerr signal. Additionally, this detection scheme also allows one to perform electro-optic measurements with comparable bandwidths.

A fast detector converts the polarization into an electrical signal that is then sent to a real-time, digitizing oscilloscope (LeCroy Wavemaster 8500A-VL) with 20 GS/s sampling rate. Oscilloscope acquisition is initiated by a pair of triggers: after first detecting a rising edge of the optical modulation, $f_r (f_1, f_2)$, the oscilloscope then triggers on the first detected laser pulse. After being triggered, the oscilloscope simultaneously acquires two waveforms until the fast memory (32 MB) is filled, corresponding to 1.6 ms of continuous data. One waveform corresponds to the signal from the fast detector, while the other channel acquires a waveform representing the pump laser. This second waveform is necessary to determine the time of the pump events because the pump laser is not phase-locked to the sampling clock of the oscilloscope, as discussed in Section 6.3.

6.3 DIGITAL SIGNAL PROCESSING

The 32 MB waveforms acquired by the detection electronics are transferred over gigabit Ethernet to a single processor Pentium PC (2.4 GHz clock speed, 2 GB memory), which performs the digital signal processing while the oscilloscope acquires the next dataset. The main steps of the digital processing algorithm implemented are: demodulation, time slicing, and averaging of the data.

As mentioned above, the pump and probe laser beams are modulated in polarization and intensity, respectively, allowing the implementation of a phase sensitive lock-in detection scheme by applying a Fourier decomposition method to the acquired time-dependent digital signal of samples. For the frequency of interest, f_r , one can define a basis of square-integrable functions:

$$\begin{aligned}
 \tilde{X}_0(t) &\equiv 1/\sqrt{2} \\
 \tilde{X}_i(t) &\equiv \cos(2\pi i f_r t), \quad i = 1, 2, \dots, \\
 \tilde{Y}_j(t) &\equiv \sin(2\pi j f_r t), \quad j = 1, 2, \dots
 \end{aligned}
 \tag{6.2}$$

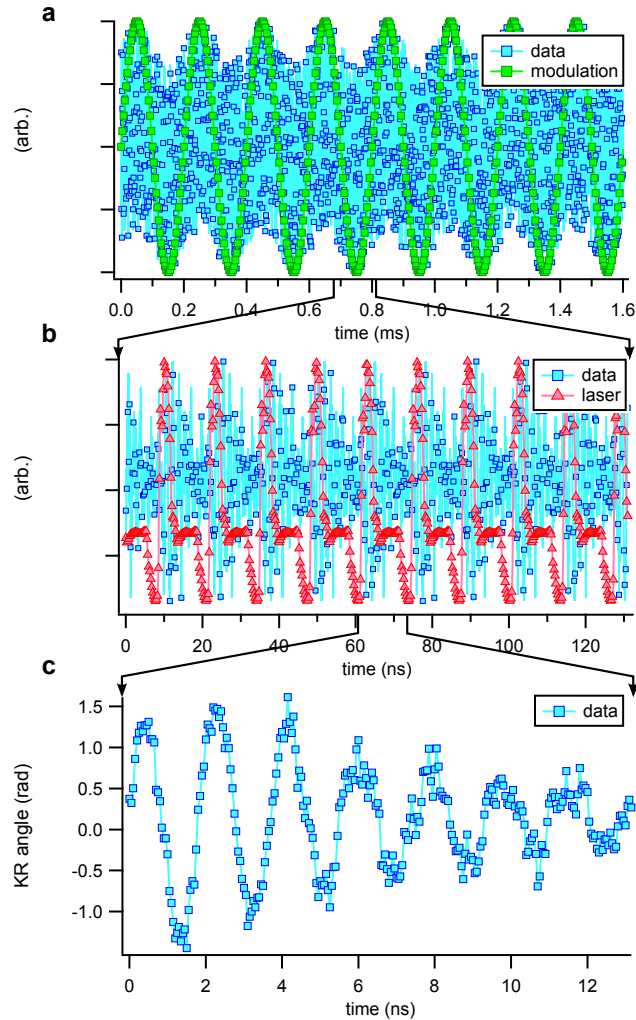


Figure 6.3: Data processing steps: (a) the acquired data is demodulated at the reference frequency f_r ; (b) the independently acquired laser pulses are used as a reference for slicing the data waveform into segments commensurate with the excitation laser period; and (c) the resulting time-resolved Kerr rotation after processing 1.6 ms of acquired data.

with the property that $\langle \tilde{X}_i | \tilde{Y}_j \rangle = 0$ and $\langle \tilde{X}_i | \tilde{X}_j \rangle = \delta_{ij}$, where δ_{ij} is the Kronecker delta function. The Fourier decomposition of the signal then becomes

$$\tilde{S}(t) = \sum_{i=0}^n a_i \tilde{X}_i(t) + \sum_{j=0}^n b_j \tilde{Y}_j(t), \quad (6.3)$$

where $a_i = \langle \tilde{S} | \tilde{X}_i \rangle$, $b_j = \langle \tilde{S} | \tilde{Y}_j \rangle$ and the upper limit $n = t_{\text{samp}} / (2 \cdot f_r)$, with the sampling period $t_{\text{samp}} = 1/20 \text{ GHz} = 50 \text{ ps}$. In the simple case this allows the in- and out-of-phase components of the Kerr rotation at the reference frequency f_r to be extracted. The phase is determined by an autophase sequence similar to a conventional lock-in amplifier when the data is processed off-line.

For a typical pump laser repetition rate of 80 MHz and a data acquisition time of 1.6 ms, the sample is excited $\sim 128,000$ times. Consequently, the acquired waveform contains an equivalent number of snapshots of the spin dynamics, with each time interval being approximately $T_L \approx 13 \text{ ns}$ long and digitized in $n_L = 264$ samples. Using the independently acquired waveform of the laser pulses, the demodulated data can be partitioned into one-period segments, which are averaged together (Figure 6.3c) to produce a final waveform with 264 samples. The demodulation, time slicing, and averaging are thus equivalent to n_L parallel lock-in amplifiers. Therefore the speed at which dynamic data can be acquired is proportionally increased compared with traditional scanning mechanical delay stage, pump-probe experiments.

6.4 EXPERIMENTAL RESULTS

We have implemented our detection scheme to characterize the electron spin dynamics in n -GaAs (10^{16} cm^{-3} Si doped) epilayers. The sample was placed in the Voigt geometry in a magneto-optical cryostat which allows magnetic fields to be applied parallel to the sample surface. The sample was held at 15 K for the duration of the experiment. The electron spin direction is initialized with circularly polarized laser pulses (150 fs pulsewidth) generated by a mode locked Ti:Sapphire laser (50 mW), tuned above the bandgap of GaAs (815 nm). A linearly polarized continuous wave Ti:Sapphire laser (20 mW) is tuned to 822 nm to be near the absorption edge of GaAs. (Although our probe beam has a higher power than is generally used, the peak power is approximately five orders of magnitude less than when using femtosecond pulses.) The probe beam monitors the component

of the electron spin magnetization along the light propagation direction. The time-dependent Kerr signal is detected using a pair of fast balanced photodiodes (New Focus Si 650 MHz balanced receiver). Demodulation was performed at the sum frequency: $f_r = f_1 + f_2$.

In a transverse magnetic field, the initialized electron spin population precesses around the magnetic field direction at the Larmor frequency, which is proportional to the magnetic field B and the electronic g factor. The instantaneous component of the electron population perpendicular to the magnetic field can be described by

$$S_z(t) = A \exp(-t/T_1^*) \cos(\omega_L t), \quad (6.4)$$

where A is the transversal magnetization of the electron spins at $t = 0$, $\omega_L = g\mu_B B/\hbar$ is the Larmor frequency (where g is the Landé g -factor, μ_B is the Bohr magneton, and B is the magnetic field), and an exponential envelope for the oscillatory signal is introduced to account for decoherence of the spin system with the inhomogeneous transverse dephasing time [151].

Figure 6.4a depicts the Kerr rotation data recorded for the n -GaAs epilayers as a function of time and magnetic field. The magnetic field is swept from -200 to $+200$ mT in steps of 1 mT; 16 ms of data is acquired at each field step. The experimental data is in good agreement with simulated data obtained using $g = -0.41$ and a transverse spin decoherence time of $T_2 = 10$ ns. The small offset from zero field arises from trapped flux in the superconducting magnet. In GaAs, the spin decoherence time is particularly long compared with the laser repetition rate so we have used a modified version of Equation 6.4 [151]:

$$S_z(t) = \sum_{n_{probe}} \exp\left(-\left(t + n_{pulse}T_L\right)/T_2\right) \cos\left(\omega_L\left(t + n_{pulse}T_L\right)\right). \quad (6.5)$$

This equation accounts for the polarization of the electron spin remaining beyond the 13 ns period between consecutive laser pulses.

A consequence of this long decoherence time is the observation of resonant spin amplification at specific magnetic fields for which the Larmor precession frequency is commensurate with the laser repetition rate (Figure 6.5) [151]. One of the experimental features not accounted for in the simulation is the higher intensity of the resonant spin amplification signal at $B = 0$ T. However, in our simulation we have not considered the field dependence of the spin life time which for $n = 3 \times 10^{16} \text{ cm}^{-3}$ doped GaAs decreases with increasing magnetic field [151].

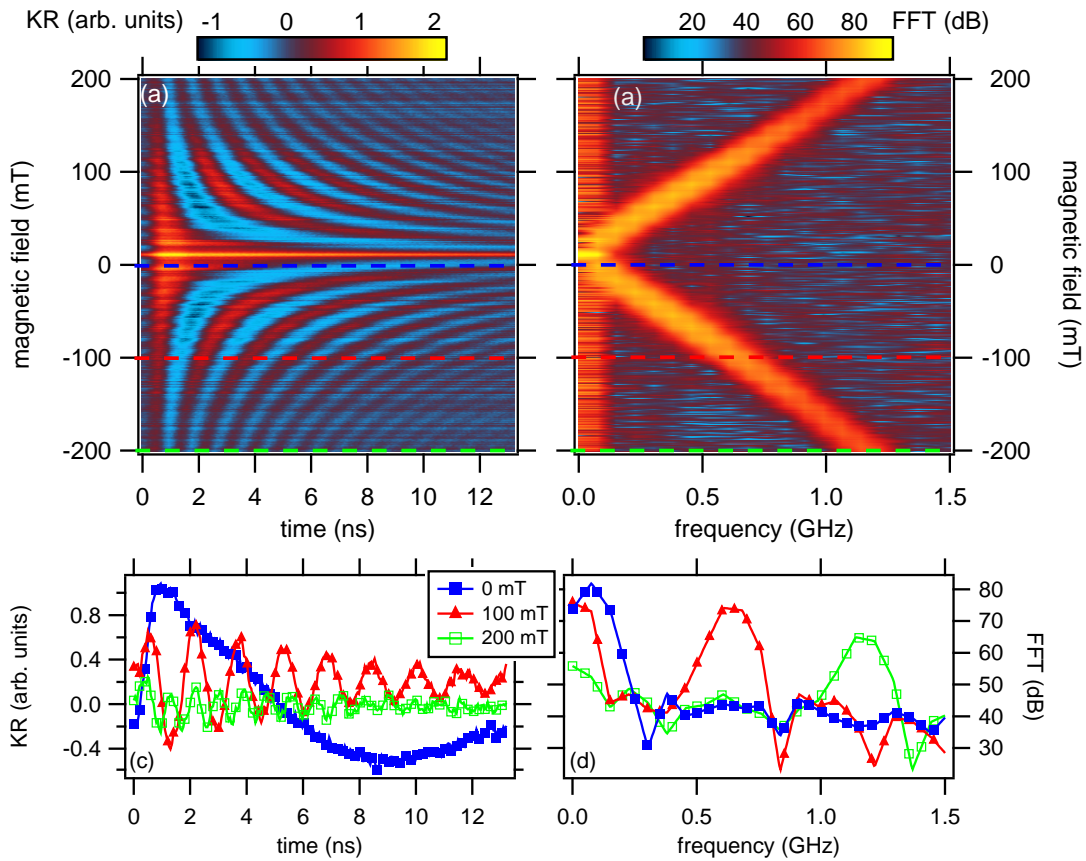


Figure 6.4: (a) Acquired Kerr rotation data for n-GaAs as a function of the delay time (horizontal axis) and external magnetic field (vertical axis); (b) Fast Fourier Transform (FFT) of the data giving the Larmor precession frequency as a function of the magnetic field; (c) Line cuts through the Kerr rotation plot at different magnetic fields (0, 100 and 200 mT); (d) Line cuts through the FFT data showing the resonant frequency for $B = 0, 100, 200$ mT.

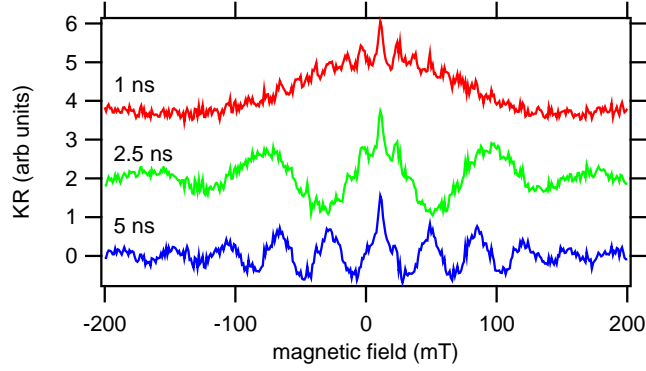


Figure 6.5: Kerr rotation as a function of magnetic field. Rapid oscillation visible at 1 ns is due to resonant spin amplification. Slow oscillations visible at 2.5 and 5 ns are due to changing precession frequency with field. Curves are offset for clarity.

6.5 DISCUSSION

The estimated speed of collecting and processing the information is similar to that of scanning mechanical delay pump-probe experiments. The major bottleneck in the presented implementation is the PCI architecture of the oscilloscope, in which the data stream requires a $T_r \sim 13$ s recovery time after each 1.6 ms segment of data is acquired by the fast memory in the oscilloscope. With the use of dedicated field programmable gate arrays (FPGA) for the DSP, the current architecture can be greatly improved by virtually eliminating the recovery time and increasing the efficiency by $T_r / (N \cdot T_{samp})$: a factor of 10^4 speedup for a given SNR.

Given the above potential for improving the data collection efficiency, is it reasonable to think that the GHOST technique has the ability to detect the signal from a single spin? Mikkelsen and Berezovsky *et al.* [156] were able to use conventional sampling TRKR to measure single spin dynamics (albeit with a rather long probe pulse and long integration times). The KR signal they measured, ϑ_{MB} , was about $10 \mu\text{rad}$. As their quantum dots were embedded in a Fabry-Perot cavity, they got an approximately $15\times$ enhancement of the signal. Therefore, we conclude that the KR angle from a single spin without a cavity is $\vartheta_{SS} = 0.67 \mu\text{rad}$. They observe approximately 6

Table 6.1: Summary of noise calculation comparing the GHOST measurement technique with the single spin dynamics measured by Mikkelsen and Berezovsky *et al.* (Ref. 156).

	Mikkelsen - Berezovsky	GHOST
NEP ($\mu\text{rad} / \sqrt{\text{Hz}}$)	7.76	0.78
ϑ_{SS} (μrad)	0.67	*
T_{min} (sec)	43	0.043

μrad of noise. When compensating for the cavity amplification, and accounting for the $T = 2$ min integration time, we calculate their noise equivalent power (NEP) to be $\delta\vartheta_{MB,NEP} = 7.8 \mu\text{rad} / \sqrt{\text{Hz}}$.

It is not straightforward to directly measure the KR angle using the GHOST setup because the fast detector does not output the sum signal or the signal from each channel individually. (Recall from Chapter 2 that the expression for Kerr angle is $\vartheta_F \approx \frac{1}{2} (V - H) / (V + H)$, where $V - H$ is what is measured by GHOST.) We can, however, estimate $V + H$ from the probe laser power at the sample and our knowledge of the losses for the reflected beam going to the detector. In this way, we have calculated the angle of the data, as shown in Figure 6.3c. After subtracting a fit to the data, we find the noise to be $\delta\vartheta_{GHOST} = 179 \mu\text{rad}$. To calculate the NEP we use the integration time of $T = 1.6$ ms *divided by* the number of points, $n_L = 264$ (because GHOST uses parallel acquisition technique). In this way we determine that $\delta\vartheta_{GHOST,NEP} = 0.78 \mu\text{rad} / \sqrt{\text{Hz}}$. Table 6.1 summarizes these results and shows the minimum integration time, T_{min} , to have a signal to noise ratio of one (assuming that the rotation angle from a single spin is $\vartheta_{SS} = 0.67 \mu\text{rad}$).

As shown above, by calculating the noise power we can estimate how long we must integrate to get to the signal from a single spin, and we conclude that it is in principle possible to measure the signal levels produced by a single spin with the GHOST technique. Furthermore, as pointed out by Berezovsky [157], the KR angle from a single spin is not N times smaller than the KR angle from N spins. The signal from a single spin has a Lorentzian lineshape of the form

$$\vartheta_{KR}(E) \propto \frac{E - E_{c,v}}{(E - E_{c,v})^2 + \Gamma_v^2}, \quad (6.6)$$

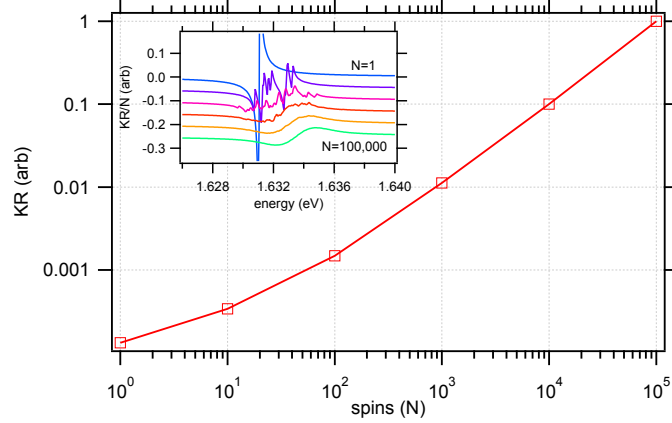


Figure 6.6: Modeling the Kerr rotation angle of an ensemble of spins. One can see that the signal from a single spin is not 10^5 times smaller than the signal from 10^5 spins. The inset shows the modeled KR as a function of energy, where each curve is a summation of Equation 6.6 from $N = 1$ to 100,000 spins. Curves are offset for clarity.

where $E_{c,v}$ is the energy of the transition and Γ_v is the linewidth. The signal from an ensemble of spins will be given by summing Equation 6.6 over the number spins *and* inhomogeneously broadening $E_{c,v}$. Figure 6.6 shows how the KR angle scales sub-linearly with the number of spins.

6.6 CONCLUSIONS

In summary, we have presented a method for acquiring time-resolved optical signals using CW optical probes. Using this method, it is possible to work close to the time-energy uncertainty limit and obtain simultaneously high spectral selectivity and temporal resolution. This method is able to provide improved signal to noise characteristics compared to sampling techniques. With signal processing improvements, the method presented here may enable the real-time monitoring of electron spin dynamics in spectrally narrow systems, such as semiconductor quantum dots.

7.0 TOWARDS SINGLE SPIN DETECTION IN SEMICONDUCTORS

For spintronics and solid-state quantum computing applications, controlling and interacting with single electrons is an important requirement. Many solid-state quantum computing proposals intend to use electron spin (a natural two-level system) as a qubit. In semiconductors with a direct bandgap, optical selection rules can be used to create a spin polarization, and in low-dimensional systems, such as quantum dots, optical pumping can achieve 100% spin polarization. A central component of the COSMQC proposal (reviewed in Chapter 1) are single electrons confined in a Ge/Si quantum dots. In this chapter I will discuss our efforts to develop optical experiments that are sensitive to single quantum dots. Unless stated otherwise, all optical experiments are performed at 10 K in a continuous flow cryostat.

7.1 INDIUM ARSENIDE QUANTUM DOTS

A central component of a COSMQC quantum computer is the use of single spins confined in Ge/Si quantum dots as qubits. As discussed in Chapter 1, important reasons for this material choice are an established method for patterning ordered arrays of Ge/Si quantum dots [34] and the long (millisecond) coherence times of spins in Si. These are features that represent important steps in satisfying two of DiVincenzo's requirements: scalability and long qubit lifetimes.

Although Ge/Si quantum dots sound like a promising system, creating an ordered array of dots with a direct bandgap ($d < 10$ nm) was and still is an ongoing research project in itself. We therefore pursued, in parallel, developing measurement techniques on a quantum dot system that is iso-energetic with Ge/Si: InAs/GaAs quantum dots. These are III-V quantum dots with a direct bandgap, and therefore performing optical measurements should be more straightforward.

InAs quantum dots with energies of ~ 1 eV were grown by molecular beam epitaxy at LNL in Campinas, Brazil [158, 159]. A buffer layer of epitaxial GaAs is initially grown on a GaAs wafer. A Si-doped GaAs back contact is grown before an undoped GaAs tunnel barrier. InAs QDs are grown on top of this buffer layer. The quantum dots are capped by an undoped GaAs layer. Photolithography is used to define contacts. Ohmic contacts are formed by annealing Ni/Au/Ge in a forming gas atmosphere. Schottky contacts are made by depositing Ni, Ti, or Pt on the GaAs cap before finishing with a bonding layer of Au.

Initial attempts to perform single dot measured measurements focused on applying lock-in measurement techniques to high-resolution spectroscopy [160]. The goal of this approach was to measure the small signals originating from single dots by spectrally separating the signal of interest from the background of the neighboring dots. This instrument used a 2 m spectrometer with an InGaAs focal plane array detector. The spectrometer dispersed light onto the x -axis of the detector. An acoustic optic modulator (AOM) synchronized with a pulse laser source deflected the beam onto the y -axis of the detector, giving access to dynamical information as well as spectral. Fourier processing of the time axis gave access to the signal at the frequency of interest, f_r .

Our next attempt at boosting the signal involved putting the quantum dot layer in the middle of a Fabry-Perot cavity. In this way we hoped to not only boost the signal (for example from photoluminescence or Faraday rotation) by increasing the coupling in the transmission window of the cavity, but we also wished to extinguish the signal from dots outside of it. Placing a quantum well or quantum dots inside a cavity has been used before to enhance the FR signal [161, 162].

The structure of our cavity is shown in Figure 7.1a. The sample is grown by molecular beam epitaxy (MBE). The end mirrors are distributed Bragg reflectors (DBRs) and are formed by growing twelve repeated layers of $\text{Al}_{0.15}\text{Ga}_{0.85}\text{As}$: $\text{Al}_{0.96}\text{Ga}_{0.04}\text{As}$. Between the two reflectors, InAs quantum dots are grown in a GaAs matrix. The length of the InAs/GaAs region determines the transmission window of the cavity. Figure 7.1b shows the transmission of the cavity (blue curve) along side the photoluminescence (red curve). From this graph one can see that the photoluminescence profile is related more to the passband of the cavity rather than the intrinsic quantum dot energy profile. This made it difficult to identify the charge state of the quantum dots in the cavity window. Future experiments would require carefully growing quantum dots in a cavity structure and a control structure without the DBR mirrors. Alternatively, one could incorporate an etch stop

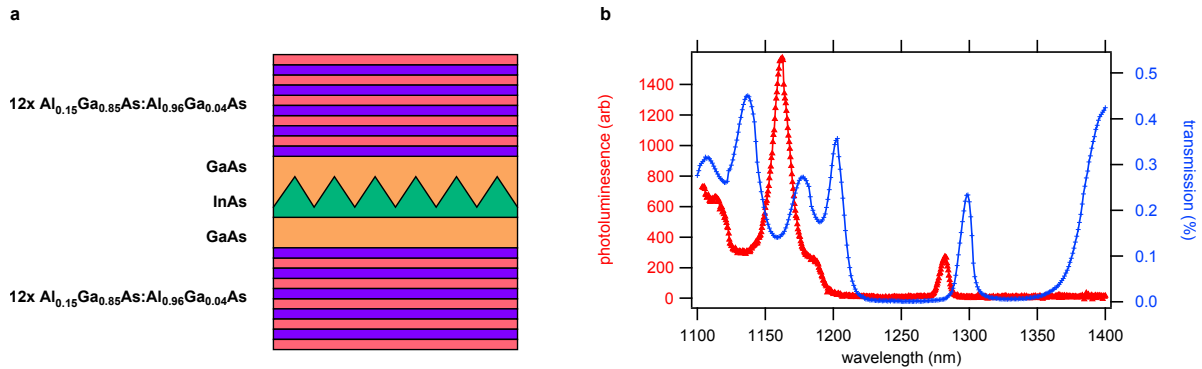


Figure 7.1: InAs/GaAs quantum dots in a DBR cavity. (a) Device structure. DBR mirrors are formed from 12 layers of $\text{Al}_{0.15}\text{Ga}_{0.85}\text{As}:\text{Al}_{0.96}\text{Ga}_{0.04}\text{As}$. (b) Comparison of photoluminescence at 10 K (red curve) and transmission at 300 K (blue curve).

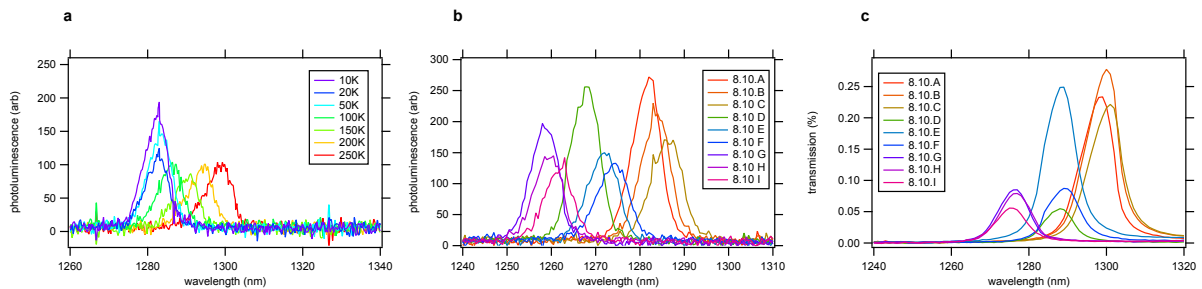


Figure 7.2: Photoluminescence and transmission of InAs quantum dots in DBR cavity. (a) Photoluminescence as a function of temperature. (b) and (c) Photoluminescence and transmission at different positions on the wafer.

layer above the quantum dots and then mask and etch away the top DBR stack in a selected area. Although because AlGaAs is typically used as an etch stop for GaAs, it is not immediately obvious how to go about this process. Additionally, the quantum dots are in a λ -cavity of only $\sim 1 \mu\text{m}$ thickness, so this structure would require a very delicate processing procedure.

Photoluminescence as a function of temperature is shown in Figure 7.2a. The luminescence shifts to shorter wavelengths (higher energies) as the temperature is lowered, as expected [163, 164]. Photoluminescence at 10 K (Figure 7.2b) and transmission at 300 K (Figure 7.2c) demonstrate how the cavity can be tuned by changing positions on the wafer. This was done intentionally by varying the DBR parameters (cavity transmission and mirror reflectivities) during growth. The substrate was rotated during the quantum dot growth stage, so they should be generally uniform.

Ultimately these experiments were unsuccessful as single dot probes. As mentioned above, it was very difficult to identify the photoluminescence features. Another major problem was that we lacked the ability to gate the dots through the DBR stacks. Without this control we were unable to put the dot into an initial, known configuration. Another problem the cavity revealed was the noise inherent in our InGaAs detectors. We were able to fabricate cavities with quality factors (Q) exceeding 100, and even with the associated signal enhancement we could still not observe single dot processes.

Our first attempt to move to shorter wavelength quantum dots, and thus lower-noise Si detectors, was to anneal InAs/GaAs quantum dots [165, 166, 167]. The quantum dots were loaded into a rapid thermal annealer (RTA) and heated with a quartz lamp. Photoluminescence at different stages of annealing is shown in Figure 7.3. By increasing the annealing temperature to 900°C we could shift the photoluminescence to 900 nm. This is a delicate process as annealing at too high of a temperature has the potential to damage the sample through As or In lesion.

On these annealed dots we performed two types of measurements: photocurrent and photoluminescence. In order to gate the quantum dots we applied electrodes to the sample surface. An Ohmic electrode is contacted below the quantum dots and a Schottky contact is deposited on the surface. Various sizes of apertures are then defined using e-beam lithography and etched into the top gate in order to isolate a small number of quantum dots. The sample structure with electrical gates is shown in Figure 7.4a.

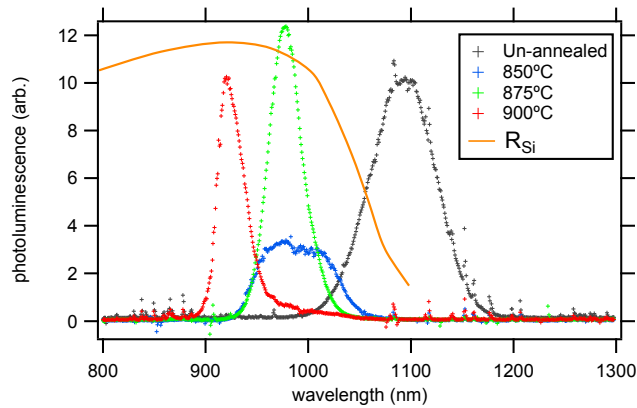


Figure 7.3: Photoluminescence of InAs/GaAs quantum dots as a function of annealing temperature. The yellow curve represents the typical responsivity of a Si detector (~ 0.2 A/W at 1100 nm). $T = 77$ K.

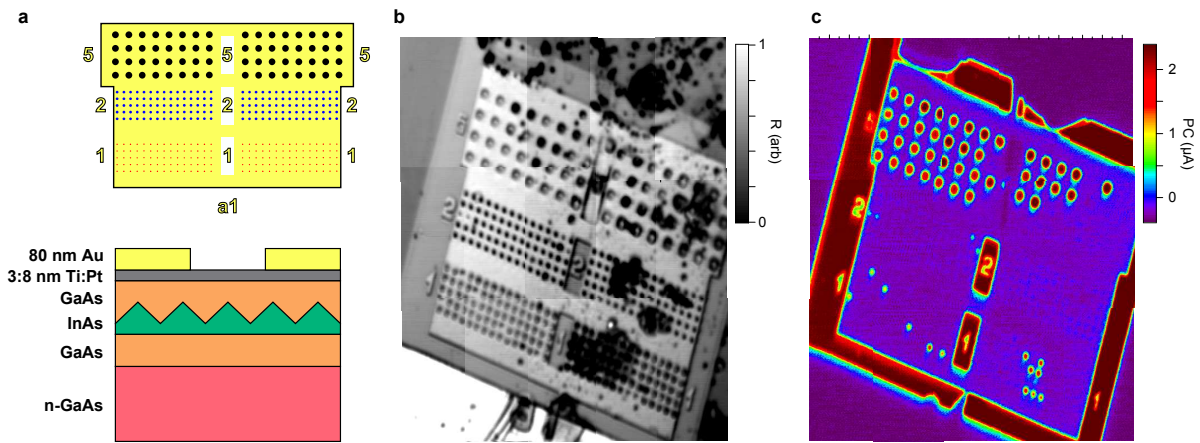


Figure 7.4: Investigating annealed quantum dots with apertures. (a) Top: Top gate electrode pattern showing 5, 2, and 1 μm apertures and markers. Bottom: Sample structure. Because of the proximity of the quantum dots to the surface (20-50 nm) it is necessary to use a semitransparent electrode under the aperture. (b) Reflectivity image of the top gate. (c) Simultaneously acquired scanning photocurrent image of top gate.

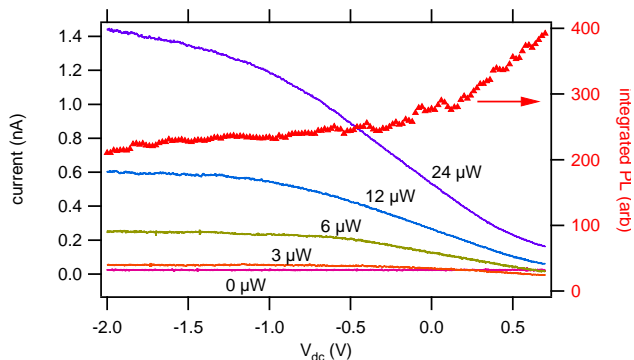


Figure 7.5: Photocurrent as a function of pump power and bias across sample.

We performed scanning photocurrent microscopy by exciting non-resonantly and collecting the photocurrent as a function of the laser position. In this way we can identify “good” apertures, as shown in Figure 7.4c. Figure 7.5 shows photocurrent as a function of DC bias and pump power. A positive bias will keep the electron-hole pairs in the dot, thus decreasing the photocurrent and giving them a chance to recombine (and therefore also increases the photoluminescence signal, as shown). Most of the 5 μm apertures are open, but only several 1 μm are open. A longer lift-off step or harsher chemicals are needed. We then tuned the pump-laser to the PL transition energy to try to resonantly excite a single dot. Unfortunately we were unable to observe signatures of single dot absorption. We also tried to measure single dots using photoluminescence. By focusing the pump laser on an aperture and lowering the power, we observed the highest occupied states drop from F to D to P to S . However, again we were unable to observe single exciton transitions.

7.2 GALLIUM ARSENIDE QUANTUM DOTS

As one can see, we tried several methods of performing single quantum dots experiments on InAs/GaAs quantum dots, unfortunately without much success. We then began to look for a different system to study. The material we finally settled on, and had the most success with in performing single spin experiments, was to use GaAs/AlGaAs interface fluctuation quantum dots. Berezovsky

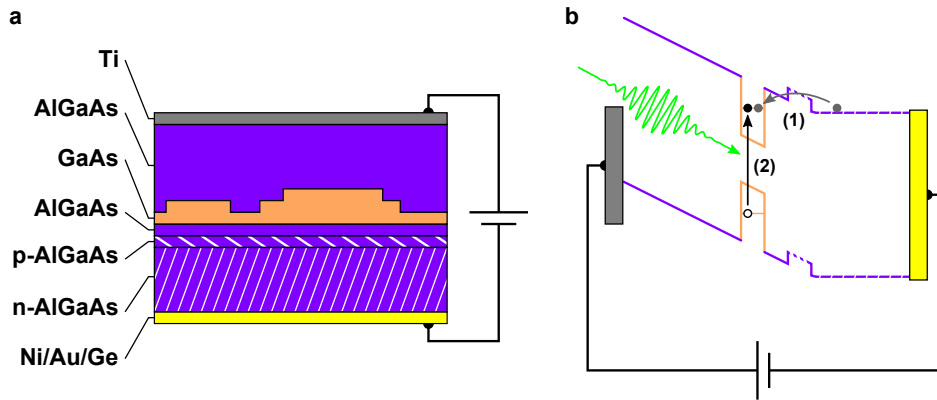


Figure 7.6: Sample structure of GaAs/AlGaAs quantum dots. (a) Physical structure of sample: GaAs quantum dots formed by interface fluctuations are embedded in an AlGaAs matrix. (b) Schematic band diagram of sample. Growth direction is to the left. The occupation of a quantum dot can be changed (1) electrostatically or (2) by optical pumping.

first measured Faraday rotation in a single GaAs/AlGaAs quantum dot [39] and followed up that work by measuring the dynamics [156] and coherent control of a single spin [168]. Part of the reason these dots are so desirable is their size, which is ~ 100 nm in diameter. Simply put, the electron and hole wavefunctions occupy a larger area, compared to InAs/GaAs quantum dots, and thus they have larger cross section in which to interact with photons, resulting in a larger Faraday rotation angle. There are also other technical reasons to like this system, such as the fact that these dots have energies that allow us to use Si photodetectors for optimal signal to noise.

Like the InAs/GaAs quantum dots, we use electric fields to tune the quantum dots. A “top” gate electrode tunes the energy levels of the quantum dots relative to a “back” gate electrode. When the levels become resonant with the Fermi sea of the back contact an electron is able to tunnel through the barrier and into the quantum dot. A circularly polarized laser would then excite an exciton with a spin-polarized electron in the conduction band. After the fast (~ 1 ns) recombination of the exciton, the dot would be left with a single electron of known spin orientation and long lifetime. Photoluminescence is used to determine the energy of the exciton. A probe laser tuned to the exciton transition can then determine if an electron is indeed present and interrogate the spin

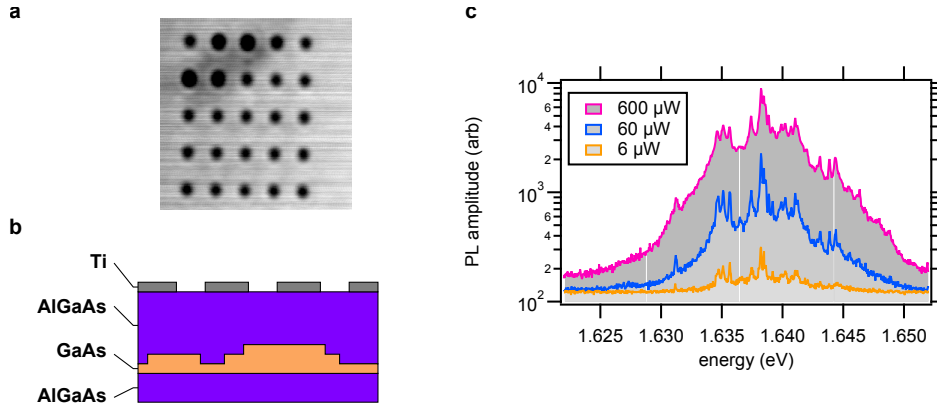


Figure 7.7: Sample with apertures. (a) Optical micrograph shown 1 μm apertures etched into electrode. (b) Sample structure showing apertures etched into top gate. (c) Photoluminescence as a function of power.

orientation via Kerr rotation (KR). The KR can study decoherence phenomena of the spin or its response to external stimuli such as applied magnetic field, adjacent ferroelectric polarization, or microwave electric fields.

Samples are grown by molecular beam epitaxy (MBE) at the University of California Santa Barbara (UCSB). Figure 7.6 shows a schematic diagram of the sample. A 1 μm -thick, n -doped $\text{Al}_{0.3}\text{Ga}_{0.7}\text{As}$ layer is deposited on a GaAs substrate. Because of the thickness of the n -doped layer, a thin (25 nm) p -doped AlGaAs layer is deposited to ensure the quantum dot energy levels will be in resonance with the back gate at reasonable biasing conditions (± 1 V). Following a 48 nm AlGaAs barrier, a 4.2 nm-thick layer of GaAs is deposited. Quantum dots are formed by a growth interruption technique [59, 60]. When the GaAs deposition is paused for several minutes, the atoms will migrate on the surface to form large (100 nm), monolayer-thick islands. The GaAs is then capped with 710 nm of intrinsic AlGaAs and finally with a thin 10 nm GaAs layer.

A back electrode is formed by masking an area with photoresist and etching through to the n -doped region. An ohmic contact is formed by evaporating Ni/Au/Ge and subsequently annealing at 500°C for 1 min. The top gate is formed by depositing 80 nm of Ti on the top surface, which will form a Schottky barrier.

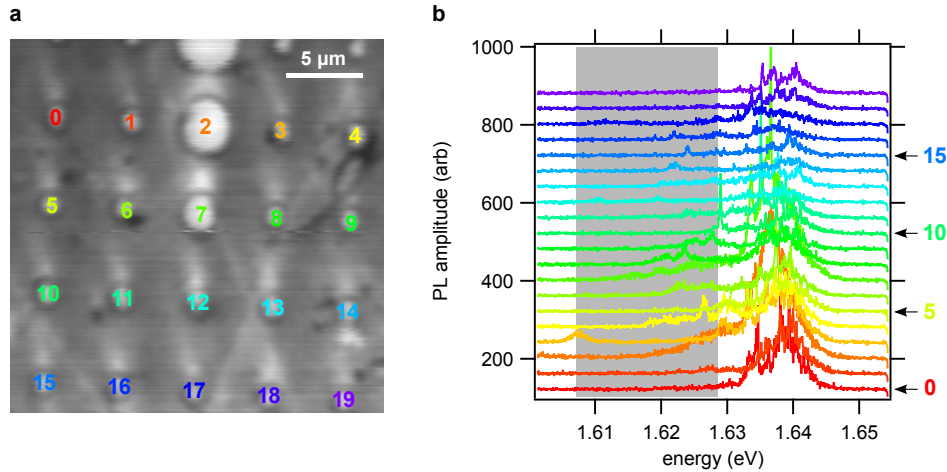


Figure 7.8: (a) Optical micrograph identifying apertures. (b) Photoluminescence of apertures identified in (a). Shaded region shows tuning range of probe laser.

Even though the quantum dots are “large,” there are still ~ 10 dots within a diffraction-limited laser spot. Our first attempt to isolate single dots is to use electron-beam lithography (EBL) to define 1 μm diameter apertures in the top gate. While this is much larger than is typically used for single dot experiments, the thick top barrier necessitates the use of large apertures, as one can see from a simple geometrical argument. Figure 7.7 shows the result of forming the apertures: a broad spectrum on an unpatterned area becomes discrete exciton transitions when exciting through an aperture. The next step is to perform a systematic search in order to find an aperture that contains a quantum dot with a well-defined charging event and energy that is separated from its neighbors. Figure 7.8 shows the results of one such search. One can see for the large marker apertures (#2, #7) the photoluminescence broadens due to contributions to the signal from a larger number of quantum dots. Overlaid with the PL graph is the tuning range of our probe laser, which further constrains which dots would be acceptable.

In order to charge the dots and tune the energy levels a bias is applied between the top and back gates. The electric field bends the energy bands so that the energy levels of the dot become resonant with the back gate. Additionally, the energy levels can be “fine-tuned” due to the quantum confined Stark effect. Photoluminescence as a function of applied bias is shown in Figure 7.9. The

“jump” in exciton lines observed near 0.5 V is a charging event, most likely going from a neutral (X^0) to a charged exciton (X^{-1}).

By applying an AC electric field (V_{AC}) we can modulate the exciton energy at f_R in order to perform lock-in detection. Figure 7.10a shows photoluminescence versus V_{DC} for $V_{AC} = 0 V_{PP}$. Figure 7.10b shows the PL during which time V_{AC} is ramped from 0 to 0.5 V_{PP} while at the same time holding fixed the DC bias at several discrete values.

We have demonstrated that we are able to use Stark-shift modulation [169] to measure the absorption of a single exciton line. Figure 7.11a shows the photoluminescence overlaid with the probe laser spectrum. Figure 7.11b shows the voltage-induced absorption change as a function of V_{DC} and V_{AC} . The result is a negative signal on the low energy side of the absorption line and a positive signal on the high energy side. Figure 7.11c shows the absorption measured as a function of V_{DC} and probe energy at a fixed AC field amplitude. The “jumps” in absorption are well-correlated with the discrete tuning of the solid-state probe laser.

Even though up to this point we have achieved several important milestones,¹ experiments to measure KR from a single exciton were unsuccessful. Berezovsky and Mikkelsen used a sample structure that sandwiched their GaAs quantum dots inside a DBR cavity, an approach we previously applied to our InAs/GaAs quantum dots. They reported an enhancement of the KR signal by a factor of 15, which is consistent with similar experiments performed with DBR cavities [161, 162].

We did not have access to a DBR cavity for our GaAs sample, so we sought to improve the coupling efficiency by utilizing index-matching from a zirconium oxide (ZnO_2) solid immersion lens (SIL) [170, 171]. A SIL has been used with a single semiconductor quantum dot to extinguish the transmission of a laser beam by 12% [172]. The index of refraction of GaAs ($n = 3.3$) is such that there is severe refraction at the solid-vacuum interface that limits the numerical aperture of light coupled into the surface. While the refractive index of ZnO_2 is high ($n = 2.13$)², there will still be unwanted refraction at the interface of GaAs and ZnO_2 . However, our efforts to obtain GaAs hemispheres were unsuccessful.

¹(1) lithographic processing to form gateable electrodes with apertures. (2) ability to detect photoluminescence from single excitons. (3) use of the Stark effect to charge dots and modulate their energy in order to measure absorption from a single exciton.

² ZnO_2 is also known as cubic zirconia. Its clear color, high refractive index, and relatively low cost make it desirable as synthetic diamond jewelry.

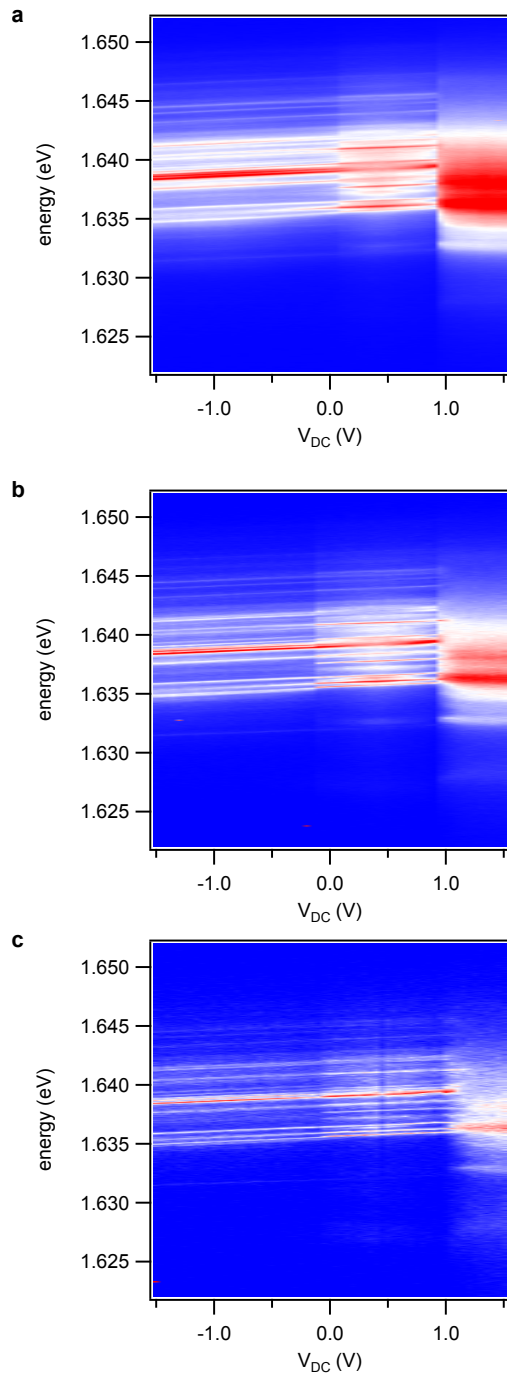


Figure 7.9: Photoluminescence through an aperture versus DC bias. (a) $600 \mu\text{W}$. (b) $60 \mu\text{W}$. (c) $6 \mu\text{W}$.

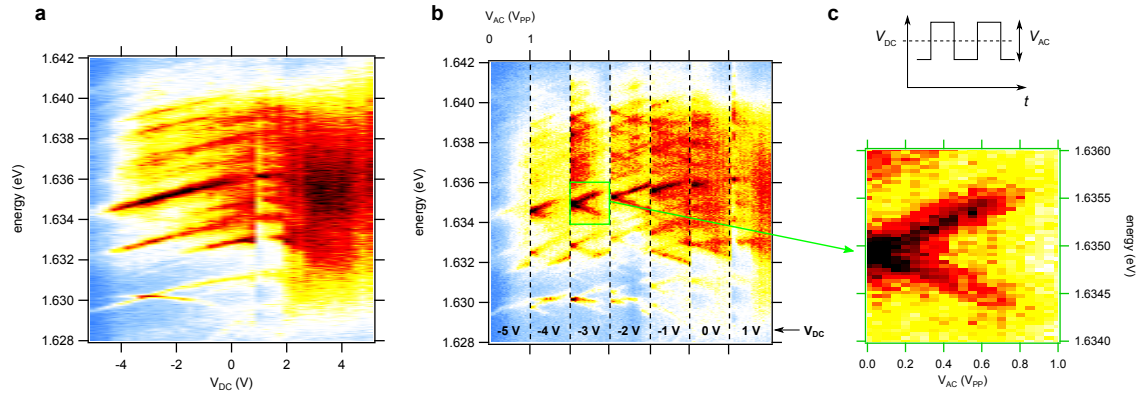


Figure 7.10: Photoluminescence versus DC and AC bias. (a) $V_{AC} = 0$ (b) Photoluminescence measured by fixing V_{DC} and then sweeping V_{AC} from 0 to 1 V_{PP} . (c) Top: bias schematic. Bottom: zoom of PL in area indicated in (b).

Attaching a SIL to the surface of our sample was not straightforward because of our need to gate the quantum dots. The existence of the top electrode acted as a spacer, creating an air-gap between the SIL and the sample, thus diminishing the benefits of index-matching. We tried pressing the SIL onto the electrode with a clamp, but this technique was not reliable. We therefore settled on “gluing” the SIL with UV-curable epoxy (Norland NOA 60). While this had yet another index of refraction ($n = 1.56$), this was more desirable than an air-gap. Even with the aforementioned problems, Figure 7.13 shows the efficacy of this technique. We measured a factor of seven (7x) enhancement of the photoluminescence from *the same aperture* with and without the SIL (Figure 7.13b).

A second type of enhancement due to the SIL is shown in Figures 7.13d-h. Each is an image of the photoluminescence at a distinct energy from a sample with a SIL but *without* apertures. The SIL improves the spatial resolution and allows us to use less excitation power (because of the improved coupling) to the point of being able to spatially and energetically resolve single quantum dots. However, apertures still are necessary for two reasons: (1) Gating with semi-transparent electrodes proved to be problematic (for unknown reasons) and (2) the apertures provide a useful marker to verify we were taking measurements on the same quantum dot week after week. An

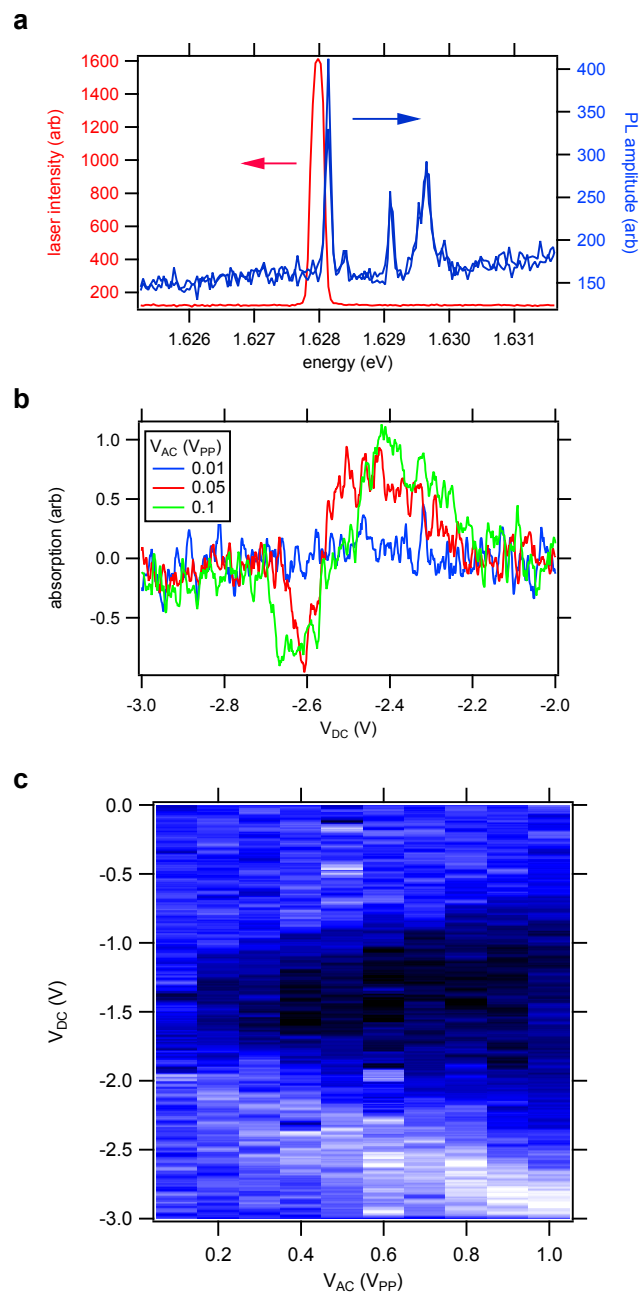


Figure 7.11: Single exciton absorption. (a) Photoluminescence (blue) overlaid with representative probe spectrum (red). (b) Single exciton measured using Stark-shift modulation absorption. (c) Absorption as a function of V_{DC} and V_{AC} .

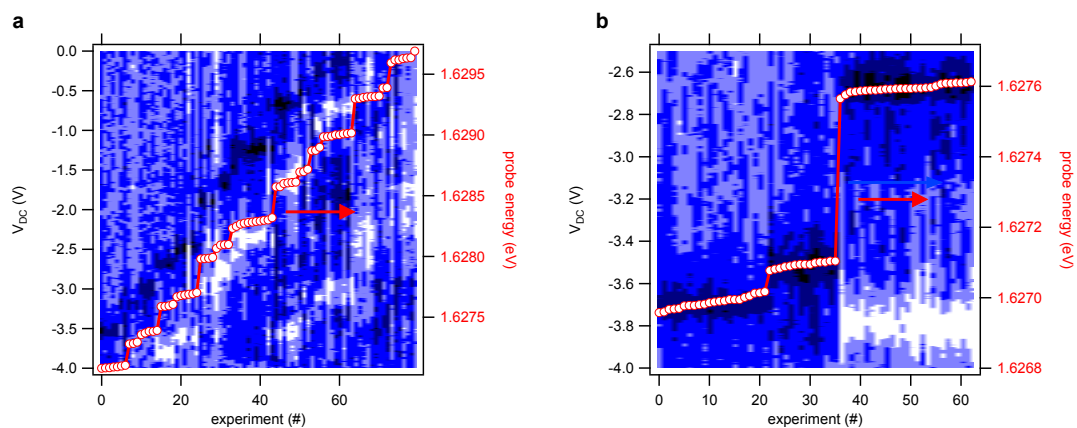


Figure 7.12: Single exciton absorption as a function of probe energy and V_{DC} .

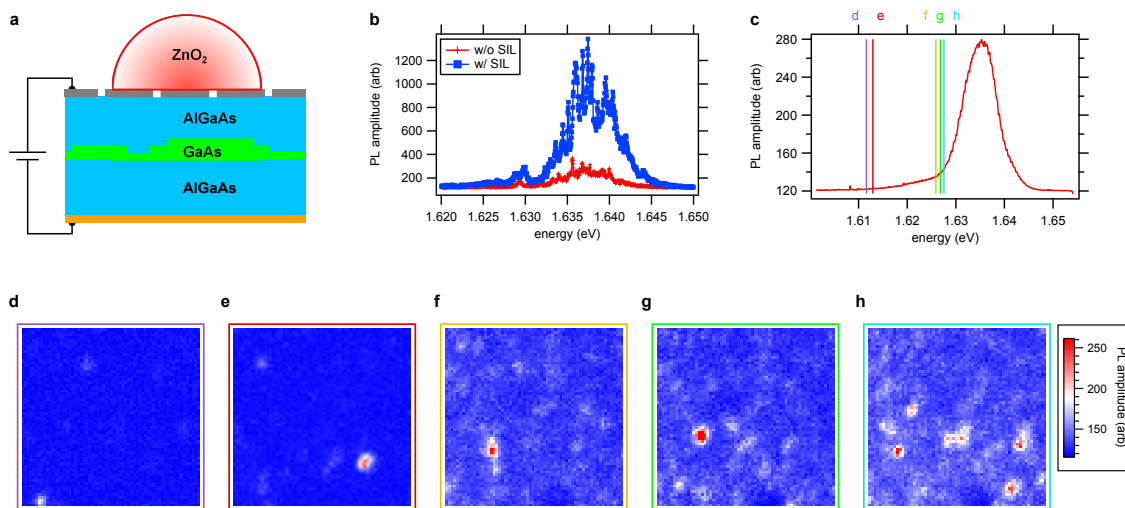


Figure 7.13: Experiments using solid immersion lens (SIL). (a) Diagram of sample. A ZrO_2 hemisphere is used as a SIL. (b) Comparison of PL with and without SIL on same aperture. An enhancement of 7x is observed. (c) PL averaged over scan area shown in Figures (d) - (h). PL images at discrete energies: (d) 1.6116 eV. (e) 1.6129 eV. (f) 1.6259 eV. (g) 1.6268 eV. (h) 1.6276 eV.

aperture also provided a feedback mechanism: by monitoring the reflectivity we could fine-tune and readjust the objective position because of sample drift. On the other hand, the resolution enhancement provided by the SIL was such that during the “gluing” procedure we could look through the SIL with an inspection microscope to center the SIL over a previously patterned array of 1 μm apertures.

Unfortunately, even with the SIL we were still unable to observe KR from a single exciton. As previously mentioned, the main difference between our sample and UCSB’s is the use of a DBR cavity. We used a SIL to increase coupling, but that may not be optimal because of the need to gate the structures. The gate electrode acts a spacer between the SIL and the sample, which decreases the utility of using an index-matching materials. A more serious problem is more likely the sample itself. The thick AlGaAs barriers necessitate a p -doped layer adjacent to the GaAs to bring the energy levels near resonance with the Fermi sea of the back contact under zero field conditions. Berezovsky and Mikkelsen were able to see a clear transition from neutral to charged exciton ($X^0 \rightarrow X^{-1}$) at +0.5 V. We have been unable to observe such a clear transition before charge screening occurs at moderate positive bias. It is possible that the p -doped layer on our sample is not the optimal thickness or doping concentration. A second problem is that the tuning range of our probe laser is limited (shown in Figure 7.8b), leaving us unable to access higher-energy quantum dots.

7.3 CONCLUSIONS

This chapter has presented our efforts to measure single spins. These measurements were initiated on InAs/GaAs quantum dots that are energetically similar to the Ge/Si dots we are interested in for quantum computing. Several experiments and sample modifications were done before switching to GaAs/AlGaAs interface fluctuation quantum dots. This system has been used by other groups to measure single spin dynamics. While we have made significant progress in performing these measurements, we were unable to observe Faraday rotation from a single exciton. It was decided that the sample itself may have been the source of our problems, either because it was not well matched with the probe laser we have or because of the device doping prevented us from getting

to the X^{-1} charge state. Measurements performed on quantum dots in a cavity could significantly improve our prospects for measuring Faraday rotation on single spins and for ultimately applying our GHOST measurement technique to single spin Faraday rotation.

8.0 A REWRITABLE NANOSCALE OXIDE PHOTODETECTOR

¹ Nanoscale devices with photonic properties have been the subject of intense research for the past decade [173, 174, 175, 176, 177, 178, 179, 82]. Potential nanophotonic applications include telecommunications [177], polarization-sensitive detectors [174], and solar power generation [180]. Although much progress has been made in the placement of nanowires [181] and combining electronic and optical nanowire components on a single chip [182], the scaling of *single* nanowire devices to macroscopic circuit sizes remains a major obstacle. *Cen et al.* [52, 53] have shown that an atomic force microscope tip can be used to write, erase, and rewrite nanoscale devices such as wires, diodes, and transistors into the interface between LaAlO₃ and SrTiO₃. Here we demonstrate the photosensitivity of these devices. By writing a wire with a gap we are able to position a nanoscale photodetector with nanometer accuracy. The detectors are sensitive to light with wavelengths from 532 nm to 1340 nm. Because the electrodes are made with standard photolithography techniques before writing the sensor, we anticipate the scaling of these nanophotonic devices to larger circuit dimensions.

8.1 INTRODUCTION

The recent discovery that a two-dimensional electron gas (2DEG) can be formed at the interface between SrTiO₃ and LaAlO₃ [48] has generated tremendous interest from the research community. The conductivity of the interface is tunable by varying the LaAlO₃ thickness [51] or by the application of an electric field [50]. In a sample with appropriate LaAlO₃ thickness, an atomic force microscope (AFM) probe can be used to write a nanoscale wire into the interface. The writing of

¹Submitted for publication to *Nature Nanotechnology*.

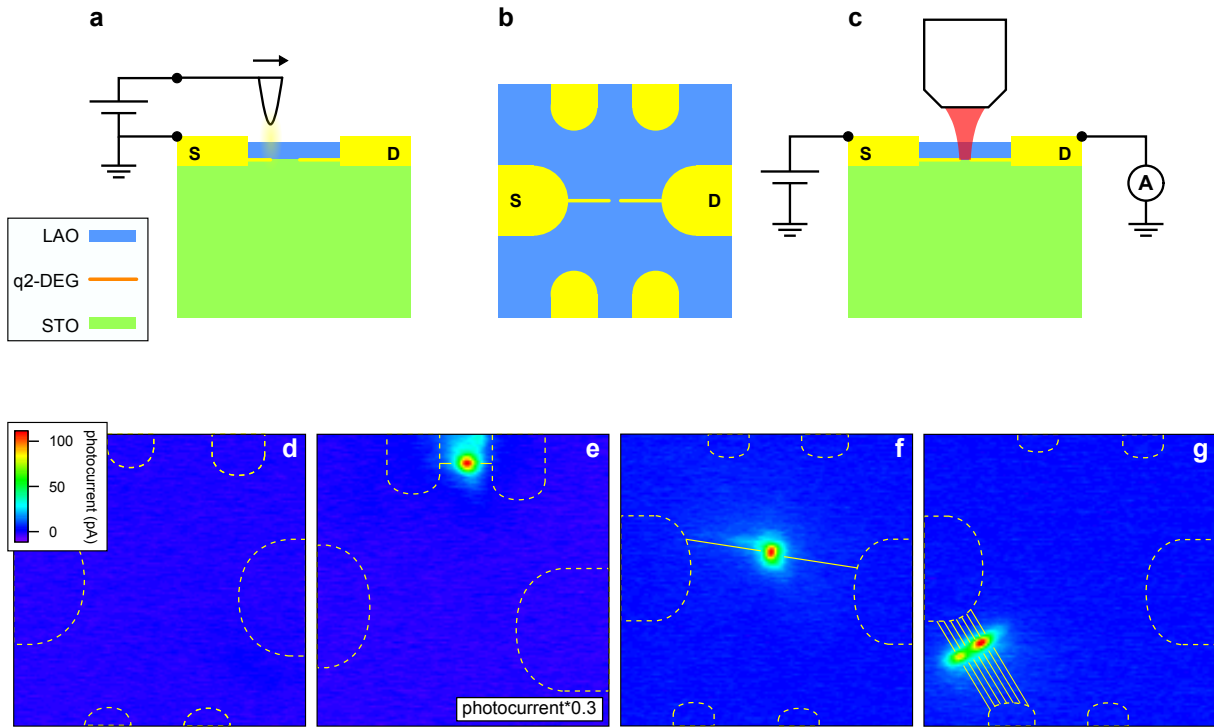


Figure 8.1: Diagram of sample and demonstration of optical sensitivity. (a) An atomic force microscope (AFM) tip is used to write a wire, resulting in (b) a 2.5 nm-wide wire with a 2.5 nm gap. (c) Optical measurements are performed by applying an electric field to the gap, shining light, and measuring the resulting photocurrent. (d) - (g) Scanning photocurrent images of various nanostructures. Images are $50 \times 50 \mu\text{m}^2$. Dashed yellow lines show outline of electrodes; solid yellow lines indicate position of nanowires. Width of line and gap separation exaggerated for clarity. (d) When no structures are written there is no observed photocurrent. A single wire with a gap can be written near (e) and far (f) from the electrodes. (g) A set of parallel wires with adjacent gaps results in a photocurrent image elongated in one direction. (d) and (e) $I \sim 2.5 \text{ kW/cm}^2$. (f) and (g) $I \sim 3.8 \text{ kW/cm}^2$. For all images: $\lambda = 633 \text{ nm}$, $V_{SD} = 0.5 \text{ V}$, $T = 300 \text{ K}$.

dots and wires smaller than 5 nm, diodes, and transistors have all been demonstrated [52, 53, 183]. These devices are being explored for applications such as reprogrammable transistors and high density data storage. In this chapter we explore the usefulness of these nanowire devices as optical photodetectors.

Samples are grown by pulsed laser deposition. Low miscut ($\sim 0.05^\circ$) toward (001) SrTiO₃ substrates were treated by a modified BHF etch and annealed in oxygen at 1000°C for 2 hours to produce a TiO₂-terminated and atomically smooth surface with single unit cell (uc) steps, as verified by AFM inspection. 2.9 uc of LaAlO₃ were deposited at a temperature of 550-600°C and oxygen pressure of 10^{-3} mbar. A laser with energy density of 2 J/cm² and repetition rate of 3 Hz was used to vaporize the LaAlO₃ single crystal target. In order to probe the interface of LaAlO₃ and SrTiO₃ low-resistance electrodes are contacted directly to the 2DEG. Ar ions from an ion beam etching system are used to mill ~ 25 nm deep into the SrTiO₃. Electrodes are then formed by first sputter-depositing a 2 nm Ti adhesion layer followed by ~ 23 nm of Au into the etched region.

Wires with 2.5 nm width are drawn between the electrodes using an Asylum MFP3D AFM in contact mode. A positive bias on the tip creates a wire and a negative bias will erase the wire. Writing is done in atmosphere at room temperature and the AFM is kept in a dark environment to suppress photo-doping of the SrTiO₃ substrate ($E_g = 3.2$ eV). The conductivity of the 2DEG is monitored with a Keithley picoammeter while writing: when the wire is connected to both electrodes a sudden rise in conductance is observed. Similarly, the conductance is monitored while cutting a wire. The distance over which the conductance drops is an indication of the wire width, as shown in Figure 8.4. Writing and erasing of nanowires is reproducible for a given tip bias.

Optical measurements are performed by focusing light through a microscope objective ($NA = 0.13$ or 0.73) to the surface of the sample (Figure 8.1c). To perform lock-in measurements, the light is amplitude modulated with a mechanical chopper at frequency f_R . A bias is applied to a source (V_{SD}) electrode and the current is collected from a drain electrode (I_D) and measured with a lock-in amplifier at frequency f_R . To create a scanning photocurrent (SPC) image, the objective is raster scanned relative to the sample with a closed-loop, three-axis piezo stage. Because the optical measurements are performed ex-situ from the AFM, as a precaution against possible device degradation [53] all measurements are performed in a vacuum of < 1 mbar. To reduce the signals

from thermally-activated carriers, some experiments are performed in a continuous flow cryostat at $T = 77$ K.

8.2 CHARACTERIZATION

Demonstration of writing photosensitive wires is shown in Figures 8.1d-g. When no device is written there is no photocurrent observed (Figure 8.1d). When a wire with a gap of 10 nm is written we observe photocurrent that is produced only at the gap (Figures 8.1e,f). Figure 8.1g demonstrates the creation of a photodetector with larger active area: seven parallel wires are drawn between the source and drain electrodes with a tip bias of +10 V and a spacing of 2 μm . The AFM tip is then moved perpendicular to the wires with a tip bias of -10 V in order to create adjacent gaps in each wire of ~ 10 nm. The resulting photocurrent image shows the expected stripe shape, demonstrating that the photocurrent signal originates from all of the gaps. Even though the focused spot size ($\sim 0.5 \mu\text{m}$) is smaller than the line spacing we cannot distinguish individual wires. This is an indication of how far from the wire free carriers are generated. The appearance of two larger peaks in the photocurrent stripe could be due to the AFM not creating wires with identical barriers in the initial writing step. These devices can repeatably be switched on and off and at least as high as 3 kHz, as shown in Figure 8.5.

In order to tune the conductance of the gap we can create a gate electrode by writing a wire perpendicular to the source-drain wire (Figure 8.2). We make the gate a “T” shape to minimize any gate-drain leakage current. Figure 8.2b shows a composite of scanning photocurrent images at various source and gate biases. Each image is produced by scanning a 2 μW 633 nm laser. By adjusting the gate voltage (V_{GD}), we can extinguish the photocurrent at reverse gate bias.

To investigate the energy dependence of the device we image the photocurrent as a function of laser energy. Excitation lasers with wavelengths of 532 nm, 633 nm, 735 nm, 1260 nm, and 1340 nm are used. Figure 8.3a shows the photocurrent measured as a function of laser wavelength and power. For visible wavelengths the photocurrent shows a nearly linear dependence with power. Remarkably, we see photosensitivity into near-infrared wavelengths, making these devices potentially useful for telecommunications applications. Comparing with the device characteristics at

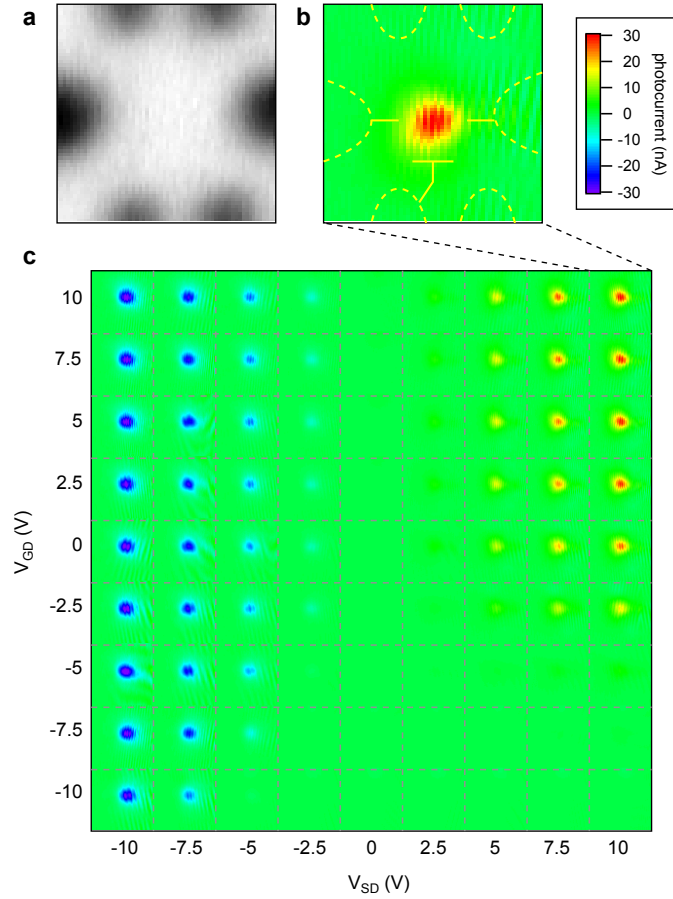


Figure 8.2: Tuning of photoconductivity. (a) Reflectivity image and (b) simultaneously acquired scanning photocurrent (SPC) image at $V_{SD}, V_{GD} = +10$ V. Dashed yellow lines show outline of electrodes and solid lines show nanostructures written with the AFM tip. Scan size is $50 \mu\text{m}$ (c) Composite image of SPC images for an array of source and gate biases. We only observe photocurrent where the photodetector was written. The photocurrent is suppressed for positive V_{SD} and negative V_{GD} . $I = 18 \text{ W/cm}^2$. Data taken at 77 K.

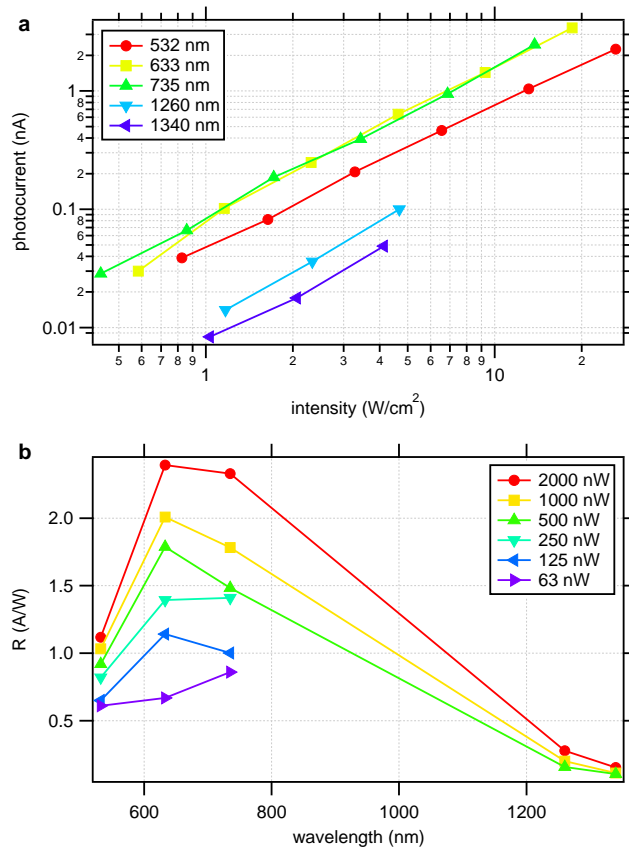


Figure 8.3: Wavelength and power dependence. (a) Photocurrent versus intensity for different laser wavelengths. (b) Responsivity as a function of wavelength. Method for calculating responsivity given in text. All data is taken on the same device as shown in Figure 8.2. $V_{SD} = 2$ V and $V_{GD} = 0$ V. $T = 77$ K.

visible wavelengths, scanning photocurrent images at 1340 nm show a similar active area of the device (when accounting for the increased spot size) and the same tuning behavior as a function of the source and gate biases (see Figure 8.6).

To calculate the responsivity R of our nanodetector we follow the method used by Hegg and Lin [184], where they use the device size to calculate the effective photon flux in order to compute R . The diffraction limited radius of a beam (w_0) is given by the expression $w_0 = \lambda f / (\pi w)$, where λ is the wavelength, f is the focal length of the lens, and w is the initial beam radius. Beginning with an expression for the intensity profile $I(r)$ of the beam in terms of the total power P_0 ,

$$I(r) = \frac{2P_0}{\pi w_0^2} e^{-2r^2/w_0^2}, \quad (8.1)$$

we then integrate $I(r)$ over the size of our detector, $r = w_D$, to calculate the effective power incident on the detector P_D :

$$P_D = \int_0^{w_D} \frac{2P_0}{\pi w_0^2} e^{-2r^2/w_0^2} 2\pi r dr, \quad (8.2)$$

$$P_D = \frac{4P_0}{w_0^2} \int_0^{w_D} e^{-2r^2/w_0^2} r dr, \quad (8.3)$$

$$P_D = \frac{4P_0}{w_0^2} \frac{-w_0^2}{4} (e^{-2r^2/w_0^2}) \Big|_0^{w_D}, \quad (8.4)$$

$$P_D = P_0(1 - e^{-2w_D^2/w_0^2}). \quad (8.5)$$

The drain current I_D is calculated by fitting each SPC image to a 2-dimensional Gaussian function of the form

$$f(x, y) = I_B + I_D \exp\left(\frac{(x - x_0)^2}{2\sigma_x^2} + \frac{(y - y_0)^2}{2\sigma_y^2}\right). \quad (8.6)$$

I_B is any DC background present in the image; x_0 and y_0 describe the location of the SPC spot in the image; σ_x and σ_y are the widths of the SPC spot. The responsivity of the detector is given by the drain current divided by the effective incident power, $R = I_D/P_D$.

Plotting R versus λ reveals a maximum in the responsivity near 630 nm (~ 2 eV), as shown in Figure 8.3b. The direct and indirect bandgaps of SrTiO₃ are 3.75 eV and 3.25 eV, respectively [185], and experiments performed on bulk SrTiO₃ show a photocurrent response only for above-bandgap excitation, $\lambda < 400$ nm [186, 187]. Therefore the mechanism by which we are exciting

carriers with such below-bandgap light is not immediately obvious. We suspect that in our samples we are exciting mid-bandgap states, of which there can be many types, as discussed below.

Feng observed an anomalous photocurrent peak at 390 nm, which was not visible in the absorption spectrum [188]. Based on infrared photoluminescence, the anomalous peak was tentatively attributed to the internal transitions of a Cr^{3+} impurity. Other reports on SrTiO_3 photoconductivity have not observed such a peak [189], although it is well-known that there can be much variability in the quality of SrTiO_3 substrates [190]. Visible photoluminescence has been attributed to the recombination of a free hole to the conduction band. Blue luminescence has been induced in SrTiO_3 by irradiating with Ar^+ [191] (thereby creating oxygen vacancies) or by electronic doping with La^{3+} or Nb^{5+} [192]. Photo-excited infrared absorption [193, 194] and multiple decay processes observed in time-resolved photoluminescence experiments [195] have been attributed to electrons and holes being captured by mid-gap traps, electrons forming polarons (which have energy below the conduction band), or electrons and holes forming self-trapped excitons (which is possible because SrTiO_3 is an ionic crystal).

While the previously discussed experiments on bulk SrTiO_3 did not show photoconduction for sub-bandgap excitation, it is possible the electric field from the electrodes gave access to the various mid-gap states by shifting the chemical potential. Shibuya *et al.* [196] have observed an electric field-induced metal-insulator transition in SrTiO_3 . In SrTiO_3 the Fermi level exists slightly below the bottom of the conduction band and when a bias is applied to the gate electrode injected electrons can become trapped in the vacant in-gap states. As the number of trapped carriers increases, the Fermi level shifts toward the conduction band, at which point the conducting channel becomes metallic.

The mechanism we therefore propose is the following. The electrodes inject carriers which are then trapped by the mid-gap states. These carriers can then be excited into the conduction band using sub-bandgap light. The nanowire created by the AFM finally provides a conducting path for the current to flow to the drain electrode. A more comprehensive photoconductivity spectrum measurement is underway, which may illuminate the nature of the mid-gap states. Additionally, a measurement of the photocurrent as a function of wavelength and electric field may also confirm this “trapped carrier” theory. This mechanism does not explain why photocurrent is visible only at

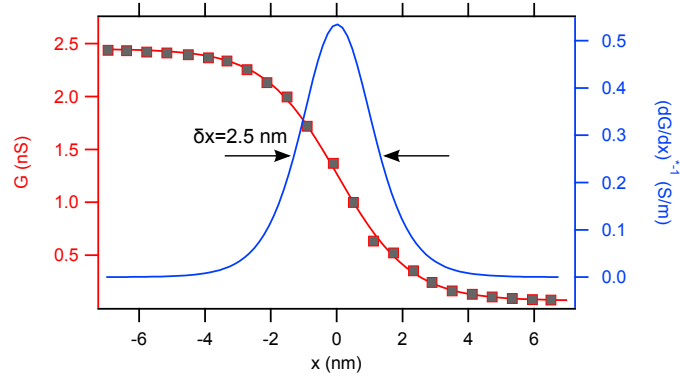


Figure 8.4: Wire width. Width of wire is determined by moving a reverse-biased tip across the wire while monitoring the conductance. The change in conductance is fitted to the function $G(x) = G_0 + G_1 \tanh(x/h)$. Also plotted is the deconvolved differential conductance $(dG/dx)^{-1}$, from which we determine the width of the nanowire.

the gap, and not everywhere along the nanowire, although it is possible that the high electric field found in the gap ($\sim 40 \times 10^6$ V/m) is necessary to accelerate the photo-excited carriers.

8.3 CONCLUSION

We have demonstrated a rewritable nanoscale photodetector. We can localize the detector with nanometer accuracy on an oxide "canvas" by placing the photosensitive junction at the location where we wish to sense a local light source. The use of pre-patterned electrodes, created using standard photolithography techniques, facilitates the configuration of multiple device geometries. Even though the direct bandgap of SrTiO₃ is 3.2 eV, in the long UV, our detectors exhibit photosensitivity to at least 1.34 μm , the limit of our measurement capability. We anticipate these devices can find widespread application in the integration of photonic and nanoscale devices for macroscopic device preparation.

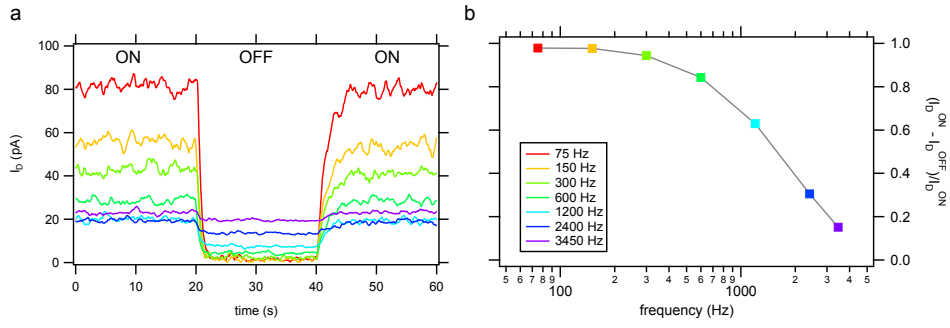


Figure 8.5: Photocurrent versus time for blocking and unblocking light for different laser modulation frequencies. (b) shows the fractional photocurrent $(I_D^{ON} - I_D^{OFF})/I_D^{ON}$.

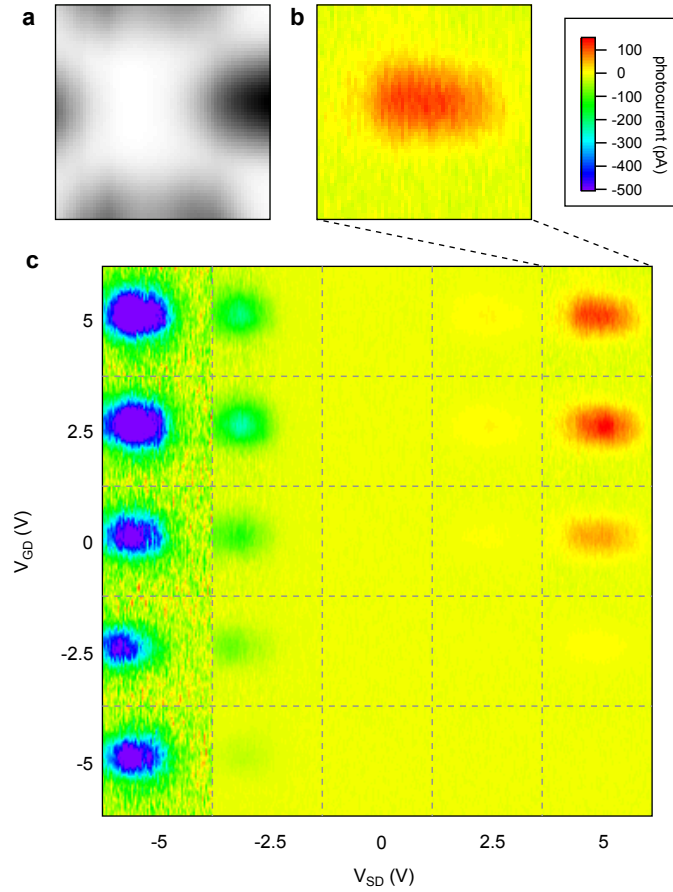


Figure 8.6: Tuning the photoconductivity in the near-infrared. $I = 4 \text{ W/cm}^2$. Data taken at 77K.

9.0 SUMMARY AND FUTURE OUTLOOK

This thesis has presented optical measurements on ferroelectric thin films and composites, bulk III-V semiconductors and quantum dots, and polar oxide interfaces. Much of this work is motivated by the COSMQC quantum computing proposal, a central component of which is Si. Although no experiments on Si-based samples are presented in this thesis, the group has generally shifted to materials that use Si in some capacity, as will be discussed below.

9.1 FERROELECTRICS

Chapters 3-5 presented the results of our optical measurements on two samples. The first was a SrTiO₃ thin film coherently strained by growth on a DyScO₃ substrate, which raised T_C above room temperature. Our TR-CSOM measurements demonstrated the uniformity of such films as compared to other room-temperature ferroelectric films like Ba_{0.5}Sr_{0.5}TiO₃. Additionally, performing TR-CSOM for a range of microwave frequencies revealed a correlation between spatial and spectral uniformity.

The second sample was a mixture of Ba_{0.6}Sr_{0.4}TiO₃ and MgO. The introduction of MgO provides an alternate method to reduce the dielectric constant and loss of the ferroelectric material, which is desirable for device applications. Our experiments revealed that the ferroelectric polarization behaves uniformly within individual (Ba,Sr)TiO₃ grains.

At this point in time there are no optical experiments being performed on ferroelectrics in our group. The most active experiments involve piezo force microscopy using an atomic force microscope. These measurements were used to verify the ferroelectricity of SrTiO₃ grown directly on Si [37]. The AFM was also used to pattern the ferroelectric—a technical achievement required by

the COSMQC proposal. Guanglei Cheng has been exploring the ferroelectric field effect in these samples by constructing FETs with a SrTiO₃ gate [197].

9.2 QUANTUM DOTS

In Chapters 6 and 7 we presented our efforts to measure single electron spin coherence in semiconductors. We developed a time-resolved optical technique that uses a continuous wave probe laser and high bandwidth electronics. This project has since focused on “porting” the GHOST code to custom hardware from Maxtek/Tektronix that combines a 12 GS/s ADC with a *user-programmable* FPGA in which we can implement the GHOST algorithm while letting the ADC run at full speed.

Our experiments on InAs/GaAs and GaAs/AlGaAs quantum dots have essentially come to a completion, at least for now. One reason, as discussed in Chapter 7, is due to the materials not being exactly what we needed. Another aspect is that now that Kerr rotation of a single dot has been measured in a single quantum dot [39], we are essentially playing catch-up. We still feel the GHOST technique is valuable for single spin Kerr rotation measurements: the UCSB group resorted to long laser pulses but they still have a low signal to noise ratio. The new GHOST hardware may see its next use in a different material system, for example in the oxide interface experiments discussed below.

Our efforts to make Ge/Si quantum dots are continuing, although no optical studies are being performed at the moment. Olivier Guise was able to pattern a carbon template [32] and subsequent deposition of Ge nucleated onto the carbon sites [34], but we never observed optical effects in these devices [198]. Reasons for this could be problems related to the growth of the Si capping layer providing an inferior barrier, such as one with traps at the interface.

Experiments on patterned Ge/Si quantum dots are now being performed in our group by Dongyue Yang in collaboration with the University of Virginia. This study focuses on materials processing issues, such as cleaning and e-beam patterning, and electrical transport measurements of the dots.

9.3 OXIDE INTERFACES

In Chapter 8 we demonstrated that we can make a nanoscale photodetector with a remarkably wide sensitivity spectrum, going from visible to near-infrared wavelength. As a new project, optical experiments at the $\text{LaAlO}_3/\text{SrTiO}_3$ interface have almost limitless potential. Our group was the first to make nanoscale devices in the interface using AFM patterning, being first reported in 2008. The first nano-photodetectors were made in mid-2009, after mere weeks of trying. Of course, one can imagine more experiments to determine the origin of the signal at junction. One of these is a more comprehensive photocurrent spectroscopy study, which is currently underway. Photoluminescence experiments could help us understand the role of defects in the substrate. Near-field optical measurements can perhaps localize the signals more to the vicinity of the junction and provide more detailed information about the origin of the photoexcited carriers.

A simple time-resolved measurement would involve pumping the device with a short optical pulse and then looking at the output on a fast scope, i.e. a GHOST measurement with the sample itself as the fast detector. Preliminary work has been done on a two-pulse time-resolved correlation experiment. A device based on GaAs photoconductive switches could also be created, even if the individual photodetectors themselves have a fast turn-on and a slow turn off. However, if the junctions do indeed have a femtosecond response, one could imagine this being a detector of THz radiation, and perhaps even a source. Such a capability would be unique in that we could locate these generators and detectors with molecular resolution, and they would have near-field sensitivity.

One can try to modulate the reflectivity of the device by electrically driving it. By modifying the chip carriers we currently use we can also attempt the same measurement in a transmission geometry. An imaging device could be constructed from arrays of detectors, although it is not immediately obvious how to address individual “pixels.”

Recently, our collaborators have succeeded in growing LaAlO_3 on SrTiO_3 grown on Si. Writing and erasing of nanowires on these Si-based devices has been demonstrated and the performance is comparable to LaAlO_3 on bulk SrTiO_3 [199], which is promising for integrating oxide-interface materials with the existing infrastructure of the silicon microelectronics industry. These samples provide new opportunities to try all of the above mentioned optical experiments.

APPENDIX A

IMAGE ALIGNMENT

The spectroscopic TR-CSOM measurements presented in Chapters 3 and 4 took approximately 12 hours for a complete dataset. Analysis then involves fitting Equation 4.1 to each point in the image, and then repeating this for each frequency. This process is shown in Figure A1 for one frequency.

Because we wish to compare the response for one point as a function of frequency it is important that the images overlap. Unfortunately, because of the duration of the experiment the sample tended to drift. I therefore wrote some LabVIEW routines that used markers identified in the reflectivity images to align the CSOM images. The first version of the code was implemented entirely in LabVIEW, with LabVIEW calling routines from MATLAB to correlate the images. In a later version the correlation was done in ImageJ [200], a free program available from the NIH. LabVIEW is still retained to automate the process by organizing the data, creating files suitable for use by ImageJ, and in the end doing the alignment and fitting. The “VolumeJ” plugin is required for ImageJ, and LabVIEW must have access to IMAQ.

A.1 IMAGE ALIGNMENT SOURCE CODE

A.1.1 ImageAlignment_with_ImageJ.vi

The image alignment work flow is described with the LabVIEW VI (virtual instrument) “ImageAlignment_with_ImageJ.vi.”

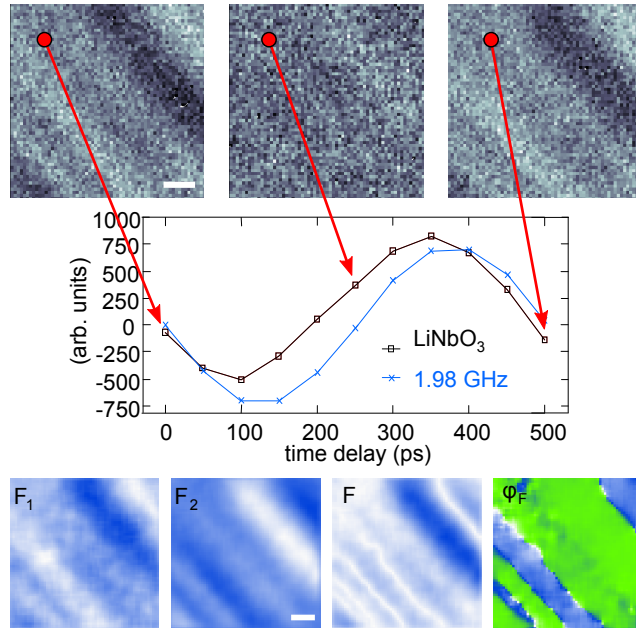


Figure A1: TR-CSOM analysis for one microwave driving frequency. Top panel shown CSOM images at three different time delays (0 ps, 250 ps, 500 ps). The response at one spatial location is plotted as a function of time delay for a LiNbO₃ control sample. These curves are then fit, resulting in images of the Fourier coefficients, as shown in the bottom panel.

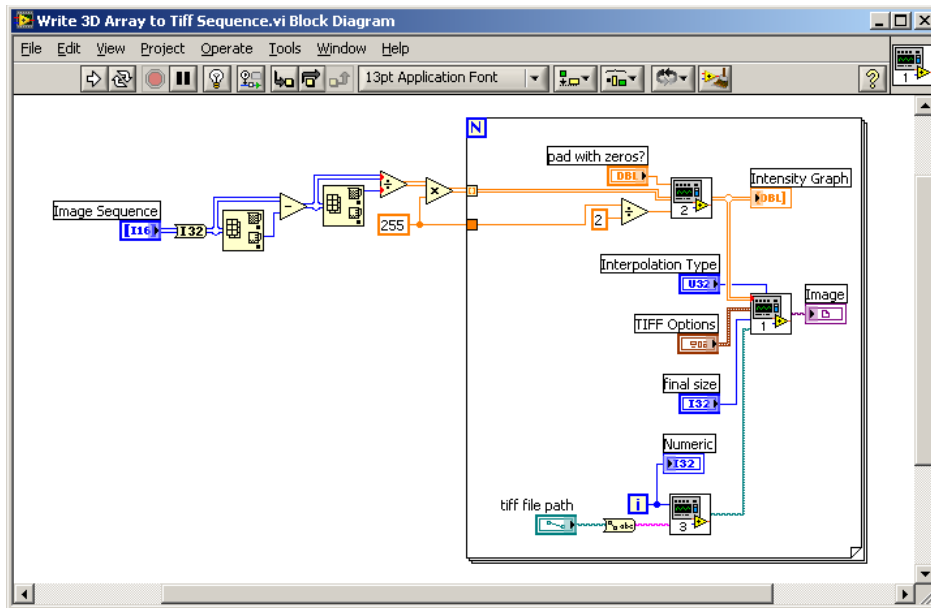


Figure A2: “Write 3D Array to Tiff Sequence.vi” converts a 3D array stored in LabVIEW to a sequence of Tiff images.

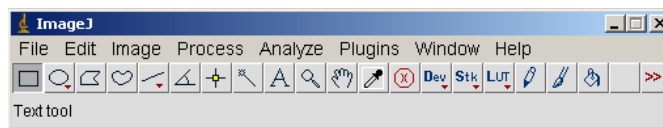


Figure A3: The free program ImageJ determines how the reference images (reflectivity) should be aligned. The “VolumeJ” plug must be installed. The user exports the results to a text file, which will be used in the next step: alignment of CSOM images. Note that the IMAQ software must be installed for LabVIEW to be able to manipulate image files.

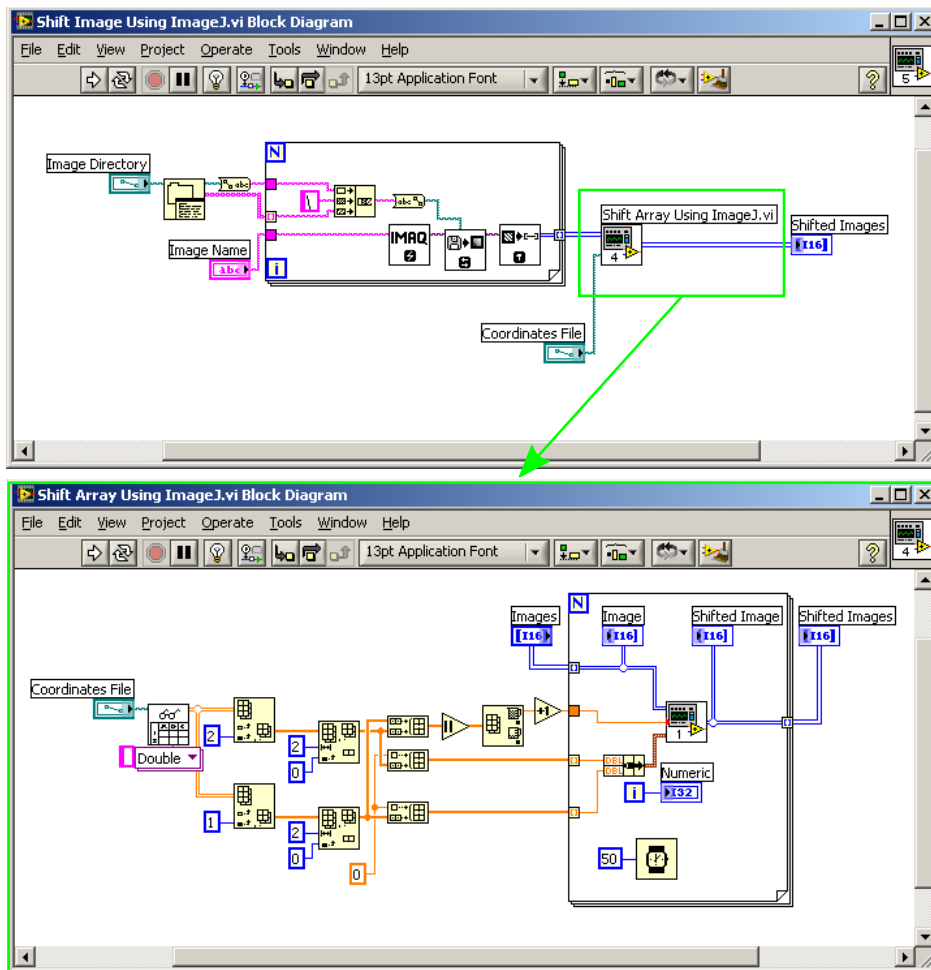


Figure A4: “Shift Images Using ImageJ.vi” reads in the Tiff image sequence, converts each image to an array, and then calls the subVI “Shift Array Using ImageJ.vi” to shift the images according to the text file exported from ImageJ.

APPENDIX B

GHOST SOFTWARE

Data processing for the GHz Optical Spin Transceiver presented in Chapter 6 is implemented in LabVIEW. This appendix will describe the software code and also how to run the program.

B.1 GHOST LABVIEW SOURCE CODE

B.1.1 `_GHOST2.0__.vi`

The source code for the top-level VI; “`_GHOST2.0__.vi`,” ; is shown in Figure B1. There are five subroutines identified: “Initialization” and “Loops 1-4” (L1-L4). L1-L4 are implemented in parallel loops using notifiers.

During the initialization routine, the oscilloscope is prepared by setting the acquisition mode, active channels and gain, and timebase. The oscilloscope is also armed and triggered, meaning an acquisition is initiated. When one acquisition is complete, the program moves to L1.

In L1 two things happen. First, a new acquisition is initiated, and, in parallel, the data from the first acquisition (from the initialization routine) is transferred from the on-board SiGe memory to a PC over an Ethernet bus. When both of these things are complete, L1 is started again, and the program moves on to L2 and L3.

In L2, the program reads the data from the “Reference” channel, which contains a waveform of the laser from a fast detector. The period of the laser is found using a peak-detection routine,

, and then the GHOST algorithm, , is applied to the same reference waveform. This is useful as a diagnostic tool: The signal of the reference channel at f_R should be constant, but the signal at $f = 0$ Hz should result in the averaged laser waveform.

In L3, the data channel is read and the GHOST routine is applied using the laser period found in L2. Here there should be no result for $f = 0$ Hz. When L2 and L3 are complete, they start over by reading the most recent data from the oscilloscope. L4 is then started, which simply reads the results from L2 and L3 and saves them to disk.

B.1.2 Multiply in Sine in Steps 2.0.vi

The GHOST algorithm is implemented in “Multiply by Sine in Steps 2.0.vi,” , the source code of which is shown in Figure B2. This VI first chops up the data from the oscilloscope (which is typically 1.6 ms long) into segments that are commensurate with the laser repetition rate (typically 12 ns). Each of these segments is multiplied by sine and cosine of the frequency of interest (and appropriate phase) by “Sine Lockin 1.1.vi,” .

“Shift PEM Frequency.vi,” , adjusts f_R slightly in order to process an integer number of periods. “Multiply by Sine Logic 1.0.vi,” , stops the loop when an integer number of periods have been processed.

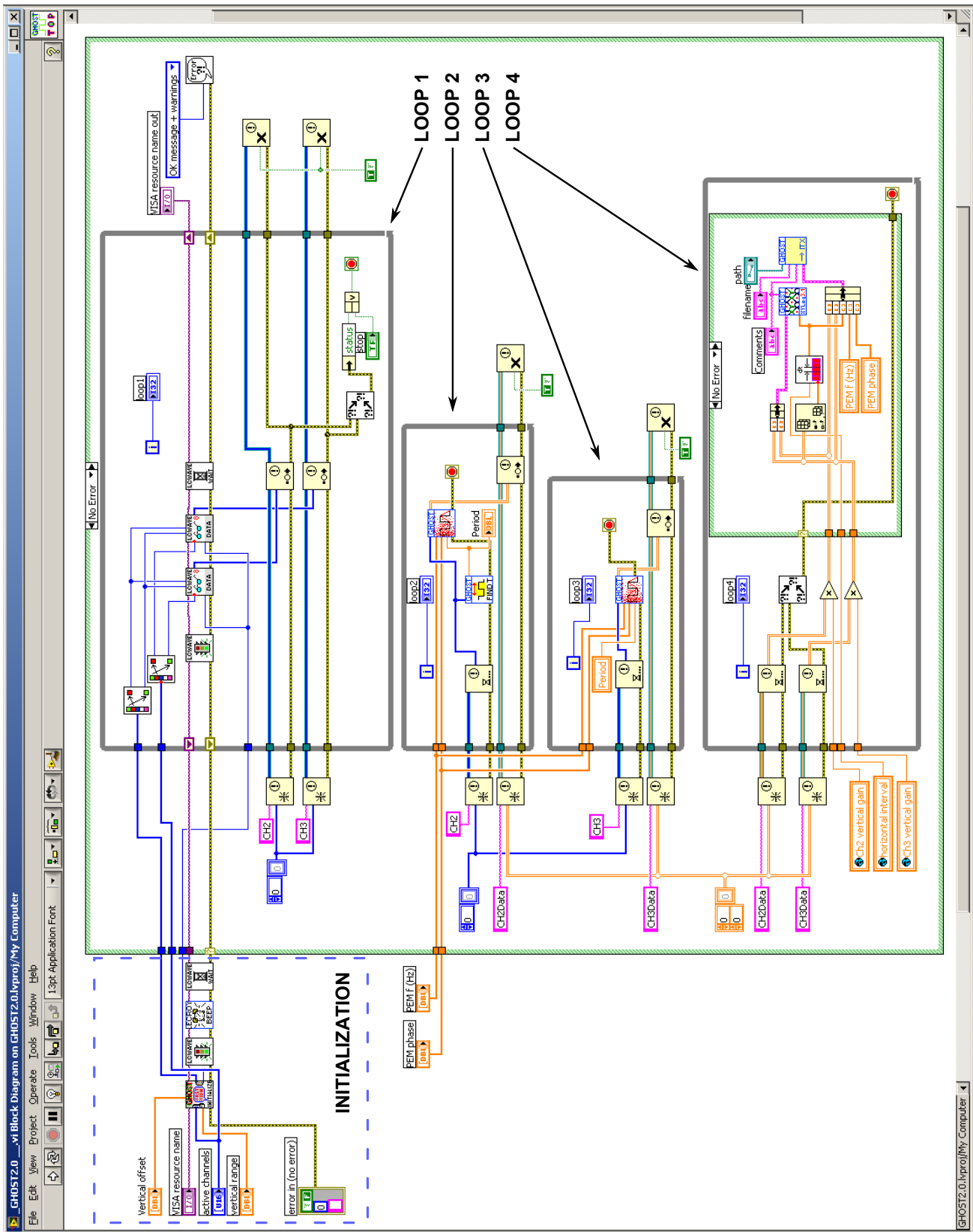


Figure B1: LabVIEW code of main GHOST routine. The functionality of “Initialization” and “Loop 1-4” will be described in the text.

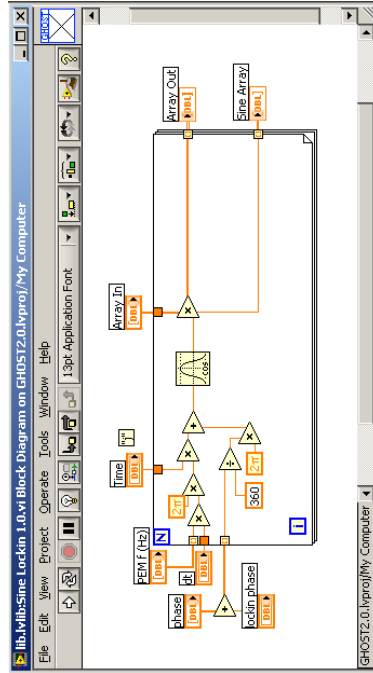
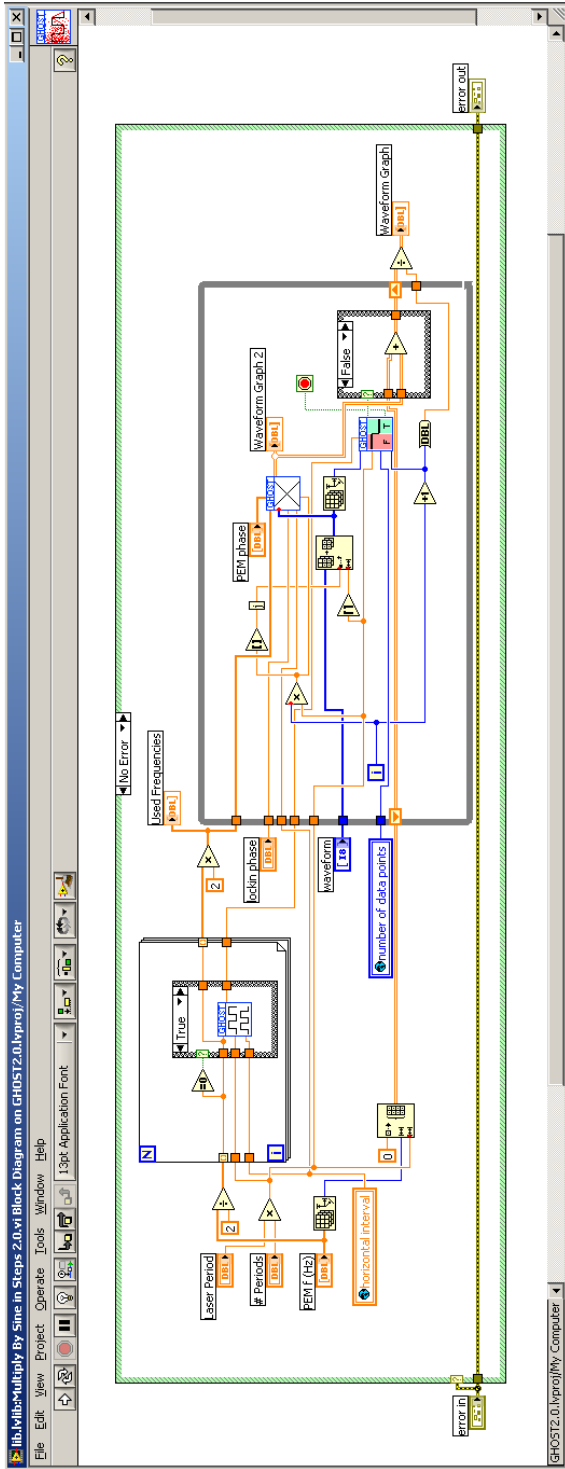


Figure B2: LabVIEW routine for GHOST algorithm. “Multiply by Sine in Steps 2.0.vi” calls “Sine Lockin 1.0.vi.”

APPENDIX C

CRYOSTATS

This appendix will describe the use of the Janis cryostats that reside in OEH 121. They are both visible in the photograph in Figure C1.

C.1 JANIS MAGNETO-OPTICAL CRYOSTAT

The large, Janis magneto-optical cryostat is a top-loading bath cryostat with integrated superconducting magnets and optical access. A schematic diagram is shown in Figure C2. The magnets can apply an 8 T field in the z -direction (toward the ceiling) and 2 T in the x -direction. Both magnets can be operated at the same time, although *not* in persistent mode and *not* at their respective maximum fields. Optical access is provided through a window on the bottom, thus revealing the need for the cryostat to be sitting on “legs.”

The cryostat consists of three main chambers. The innermost chamber is where the sample insert resides; I will refer to this as the “sample space.” Moving towards the outside of the cryostat one next encounters the “He space.” This is where the liquid He (LHe) is stored and where the superconducting magnets are mounted. Finally, the outermost chamber, and the one closest to the top of the cryostat, is the “nitrogen space.” This is filled with liquid N_2 (LN) to provide a thermal anchor to the top of the He space and to cool the radiation shield. Surrounding everything of course is a vacuum jacket.



Figure C1: Photograph of cryostats. The continuous flow cryostat is on left. The magneto-optical cryostat is on the right. The plastic bag used for sample exchanges is visible at the top of the magneto-optical cryostat. Miscellaneous optics are visible in the foreground.

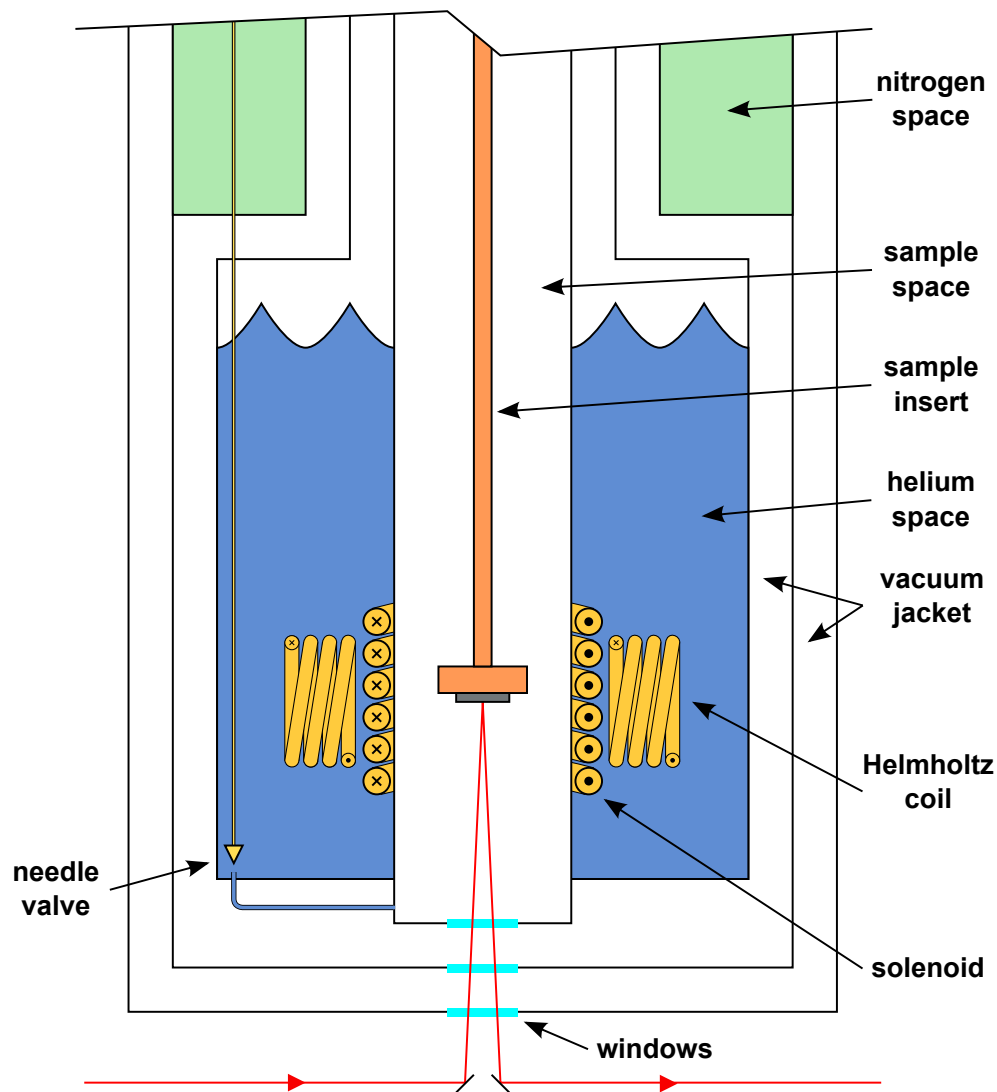


Figure C2: Schematic of magneto-optical cryostat. Green shade is the nitrogen space. Blue shade is the helium space, in which the superconducting magnets (solenoid and split pair) reside. The inner most chamber is the sample space, which is cooled with He vapor. White areas represent vacuum or partial vacuum.

C.1.1 Cooldown

The first step in the cooldown procedure is to make sure there are no leaks and to evacuate all traces of gases (other than He) from the sample space and He space. Why there would be anything other than He will become apparent in a moment when I discuss pre-cooling the magnets.

There are several hundred pounds of superconducting magnets in the He bath. Because of the relative price of LN₂ and LHe (and the inverse relationship of their heat capacities to price) it is very important to pre-cool the magnets with LN₂. This can either be done in two ways. The first method is to evacuate the He bath and fill the nitrogen space with LN₂. Keep it filled for several days, and the magnets will cool to ~ 100 K by conduction, and then you are ready to put LHe into the He space. This is not what we do. The way we pre-cool the magnets is to fill the He space with liquid nitrogen. This must be done through the He *refill* port, otherwise the pressure at the bottom of the tube will be too great to transfer any liquid. Fill the chamber at the end of one day and go home. The next morning the temperature on the vaporizer should be 100 K or less.

The next step is critical—removing the nitrogen. Insert a He transfer line into the *initial* He fill port. Remove the 3 psi safety valve and pressurize the chamber with dry nitrogen (5 – 10 psi is sufficient). Collect the nitrogen in some sort of container, a large, portable dewar is the safest. After the last drops of liquid are expelled, remove the transfer line then flush the chamber several times with **dry He**. At this time it is a good idea to open the needle valve and pump helium through it both ways (from He space to sample space and vice versa).

Now you should be ready to complete the cooldown by transferring liquid He to the He space. It is also a good idea now to open and close the needle valve several times while accumulating LHe to make sure the needle valve stays clear.

C.1.2 Sample exchange

The procedure recommended by Janis to perform a sample exchange while the cryostat is cold is to stop pumping on the sample chamber and open the needle valve to allow LHe to accumulate in the chamber. The idea is that when the chamber is then opened to the atmosphere the LHe in the sample space will boil off and prevent air from entering and condensing on either the window (bad if you are doing optical measurements) or the capillary connecting the LHe bath and sample space

(*very* bad in general). Once the sample insert is removed, seal the chamber and begin pumping again. Don't forget to close the needle valve.

Rarely does a sample exchange go this smoothly. In my experience the insert tends to freeze to the chamber walls while pulling it out. This then requires jamming, pulling, and twisting motions to unfreeze the insert. All of this adds time and a greater chance for air to enter the chamber. If you do manage to remove the insert without condensation on the aforementioned delicate bits, you are now in possession of a very cold insert. Say, is that sample sensitive to moisture? Some groups deal with this by plunging their insert into a plastic tube chamber with a positive pressure of He gas. This may be adequate in many cases, however for our Ti-ANSOM microscope insert, the piezos are very sensitive to moisture and even a short time in the atmosphere could be detrimental to their future performance

We have developed, and had moderate success with, the "bag method" of sample exchange. We attach a long, plastic bag to the ceiling, the length of which will easily accommodate the sample insert. The top is sealed and rope is pulled through and tied to the top of the insert. The rope goes to a pulley on the ceiling and then back to the ground. A person can thus pull on this rope and raise the sample insert. The bag is sealed to the flange *below* the insert. The bag is filled with He gas which is continually allowed to flow to ensure a positive He pressure in the bag. A pressure relief valve is attached to bag to prevent an explosion, although the numerous leaks at the top and bottom seals, in addition to the pinholes in the plastic, typically provide enough pressure relief. Once the sample chamber is brought to atmospheric pressure the rope is pulled on and the insert is lifted to the ceiling. The chamber is then sealed off. The sample insert is allowed to warm up in the He atmosphere.

A problem typically encountered is the freezing of the insert to the cryostat walls. In this case the rope will not provide sufficient pulling force (and zero pushing force) to free the insert. The bag must then be cut and the insert manipulated by hand. Now the chamber will be open longer than it would have without the bag. A second problem relates to sealing the sample chamber after the insert is removed: through an inflated bag one must keep track of an o-ring and blank sealing flange and then manipulate them into position to seal the chamber.

The bag method is good in principle; it is basically a poor-man's load-lock chamber. The following improvements must be made: (1) better sealing of the bag and (2) a more reliable chamber

sealing. The first improvement can be made by machining some more specialized parts (large disks for example) to which the bag can be sealed. It must be a temporary seal in order to allow the bag to be changed after it develops leaks itself. The problem of the sealing chamber can be remedied by placing a gate valve between the sample insert and the cryostat.

C.2 JANIS CONTINUOUS FLOW CRYOSTAT

The smaller cryostat in OEH121 is a continuous flow cryostat. A schematic diagram is shown in Figure C3. A special LHe transfer line with integrated needle valve is left in the LHe storage dewar while the cryostat is being cooled. We also have a special LN₂ dewar that can cool the cryostat to 80 K for much less cost. The experiment time for an experiment at 80 K can be a factor of ~ 5 longer than one at 10 K. The sample resides in vacuum and is cooled by conduction through a Cu cold finger. Having good thermal contact between the cold finger and sample is thus critical. Typically the sample is clamped to the cold finger with a small amount of Apiezon N grease in between.

The main disadvantage of the continuous flow cryostat is the lack of a variable magnet. Rare earth magnets can be incorporated into the cold finger, however you are stuck with that magnetic field. More exotic arrangements of the magnets such as a wedge would allow for some control of the magnetic field strength, but this approach is problematic for experiments involving a single quantum dot, for example.

The advantages of the continuous flow cryostat are the short temperature cycling time and the proximity of the sample to the laboratory space. The magneto-optical cryostat requires at least 2 days to cool down and 2 days to warm up. The continuous flow cryostat can be cycled daily, allowing frequent sample exchanges. This is especially useful when developing sample processing recipes.

The sample is separated from the atmosphere by only one window. This allows one to use a microscope objective with a modest ~ 5 mm working distance. For example, we have a 100x objective with 4.8 mm working distance and 0.73 numerical aperture. Also, by having the micro-

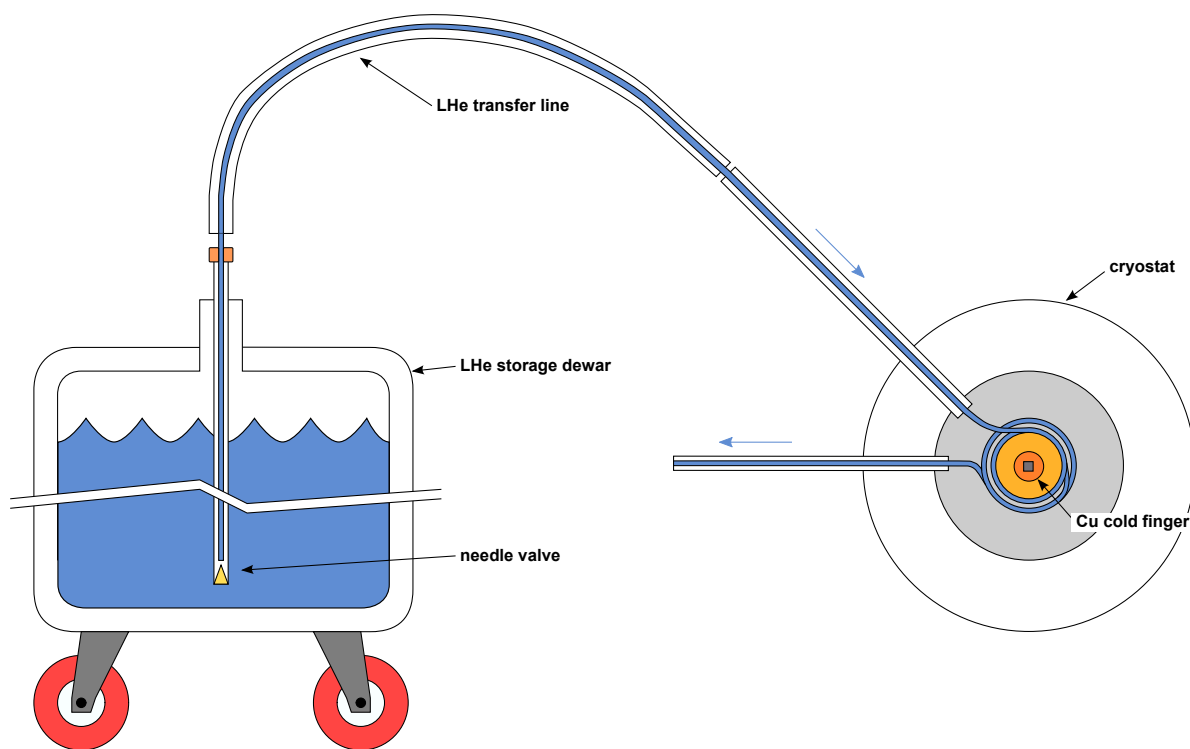


Figure C3: Schematic of continuous flow cryostat.

scope objective outside of the cryostat we can also more easily incorporate a closed-loop scanning stage for imaging experiments.

As shown in the photograph (Figure C1), the cryostat is mounted “sideways.” This orientation is chosen for two reasons. First of all, it keeps the optics close to the table. Second, by adding an extension to the cold finger, one can more easily place the sample in between the poles of a split pair magnet.

BIBLIOGRAPHY

- [1] R. Feynman, *Simulating physics with computers*, Int. J. Theor. Phys. **21**(6), 467 (1982).
- [2] D. Deutsch, *Quantum Theory, the Church-Turing Principle and the Universal Quantum Computer*, Proc. R. Soc. A **400**(1818), 97 (1985).
- [3] D. P. DiVincenzo, *The Physical Implementation of Quantum Computation*, arXiv:quant-ph/0002077 (2000).
- [4] A. Steane, *Space, time, parallelism and noise requirements for reliable quantum computing*, arXiv:quant-ph/9708021 (1997), Fortsch. Phys. **46**, 443 (1998).
- [5] A. Barenco, C. H. Bennett, R. Cleve, D. P. DiVincenzo, N. Margolus, P. Shor, T. Sleator, J. A. Smolin, and H. Weinfurter, *Elementary gates for quantum computation*, Phys. Rev. A **52**(5), 3457 (1995).
- [6] G. Burkard, D. Loss, and D. P. DiVincenzo, *Coupled quantum dots as quantum gates*, Phys. Rev. B **59**(3), 2070 (1999).
- [7] D. P. DiVincenzo, D. Bacon, J. Kempe, G. Burkard, and K. B. Whaley, *Universal quantum computation with the exchange interaction*, Nature **408**(6810), 339 (2000).
- [8] P. W. Shor, *Polynomial-Time Algorithms for Prime Factorization and Discrete Logarithms on a Quantum Computer*, arXiv:quant-ph/9508027 (1995), SIAM J. Sci. Statist. Comput. **26**, 1484 (1997).
- [9] R. L. Rivest, A. Shamir, and L. Adleman, *A method for obtaining digital signatures and public-key cryptosystems*, Commun. ACM **21**(2), 120 (1978).
- [10] A. R. Calderbank and P. W. Shor, *Good quantum error-correcting codes exist*, Phys. Rev. A **54**(2), 1098 (1996).
- [11] A. Peres, *Quantum Thoery: Concepts and Methods* (Kluwer Academic Publishers, Norwell, MA, 1995).
- [12] R. H. Morelos-Zaragoza, *The Art of Error Correctng Coding* (John Wiley & Sons Inc., Hoboken, NJ, 2006), 2nd ed.

- [13] J. Preskill, *Reliable Quantum Computers*, arXiv:quant-ph/9705031 (1997), Proc. R. Soc. A **454**, 385 (1998).
- [14] P. W. Shor, *Scheme for reducing decoherence in quantum computer memory*, Phys. Rev. A **52**(4), R2493 (1995).
- [15] D. P. DiVincenzo, *Two-bit gates are universal for quantum computation*, Phys. Rev. A **51**(2), 1015 (1995).
- [16] QIST, *A Quantum Information Science and Technology Roadmap* (2004).
- [17] D. G. Cory, A. F. Fahmy, and T. F. Havel, *Ensemble quantum computing by NMR spectroscopy*, P. Nat. Acad. Sci. USA **94**(5), 1634 (1997).
- [18] J. I. Cirac and P. Zoller, *Quantum Computations with Cold Trapped Ions*, Phys. Rev. Lett. **74**(20), 4091 (1995).
- [19] A. Shnirman, G. Schön, and Z. Hermon, *Quantum Manipulations of Small Josephson Junctions*, Phys. Rev. Lett. **79**(12), 2371 (1997).
- [20] B. E. Kane, *A silicon-based nuclear spin quantum computer*, Nature **393**(6681), 133 (1998).
- [21] D. Loss and D. P. DiVincenzo, *Quantum computation with quantum dots*, Phys. Rev. A **57**(1), 120 (1998).
- [22] A. Imamoglu, D. D. Awschalom, G. Burkard, D. P. DiVincenzo, D. Loss, M. Sherwin, and A. Small, *Quantum Information Processing Using Quantum Dot Spins and Cavity QED*, Phys. Rev. Lett. **83**(20), 4204 (1999).
- [23] J. Levy, *Quantum-information processing with ferroelectrically coupled quantum dots*, Phys. Rev. A **64**(5), 052306 (2001).
- [24] J. Wrachtrup and F. Jelezko, *Processing quantum information in diamond*, J. Phys.: Condens. Matter **18**(21), S807 (2006).
- [25] W. Paul, *Electromagnetic traps for charged and neutral particles*, Rev. Mod. Phys. **62**, 531 (1999).
- [26] J. P. Home, D. Hanneke, J. D. Jost, J. M. Amini, D. Leibfried, and D. J. Wineland, *Complete Methods Set for Scalable Ion Trap Quantum Information Processing*, Science **325**(5945), 1227 (2009).
- [27] D. Stick, W. K. Hensinger, S. Olmschenk, M. J. Madsen, K. Schwab, and C. Monroe, *Ion trap in a semiconductor chip*, Nature Phys. **2**(1), 36 (2006).
- [28] J. M. Amini, H. Uys, J. H. Wesenberg, S. Seidelin, J. Britton, J. J. Bollinger, D. Leibfried, C. Ospelkaus, A. P. VanDevender, and D. J. Wineland, *Scalable ion traps for quantum information processing*, arXiv:0909.2464 (2009).

- [29] N. A. Gershenfeld and I. L. Chuang, *Bulk Spin-Resonance Quantum Computation*, Science **275**(5298), 350 (1997).
- [30] L. Ciobanu, D. A. Seeber, and C. H. Pennington, *3D MR microscopy with resolution 3.7 μm by 3.3 μm by 3.3 μm* , J. Magn. Reson. **158**(1-2), 178 (2002).
- [31] L. M. K. Vandersypen, M. Steffen, G. Breyta, C. S. Yannoni, M. H. Sherwood, and I. L. Chuang, *Experimental realization of Shor's quantum factoring algorithm using nuclear magnetic resonance*, Nature **414**(6866), 883 (2001).
- [32] O. Guise, J. Ahner, J. Yates, and J. Levy, *Formation and thermal stability of sub-10-nm carbon templates on Si(100)*, App. Phys. Lett. **85**(12), 2352 (2004).
- [33] O. G. Schmidt, C. Lange, K. Eberl, O. Kienzle, and F. Ernst, *Influence of pre-grown carbon on the formation of germanium dots*, Thin Solid Films **321**(1-2), 70 (1998).
- [34] O. Guise, J. John Yates, J. Levy, J. Ahner, V. Vaithyanathan, and D. G. Schlom, *Patterning of sub-10-nm Ge islands on Si(100) by directed self-assembly*, App. Phys. Lett. **87**(17), 171902 (2005).
- [35] J. P. Gordon and K. D. Bowers, *Microwave Spin Echoes from Donor Electrons in Silicon*, Phys. Rev. Lett. **1**, 368 (1958).
- [36] T. Takagahara and K. Takeda, *Theory of the quantum confinement effect on excitons in quantum dots of indirect-gap materials*, Phys. Rev. B **46**(23), 15578 (1992).
- [37] M. P. Warusawithana, C. Cen, C. R. Slesman, J. C. Woicik, Y. Li, L. F. Kourkoutis, J. A. Klug, H. Li, P. Ryan, L. Wang, M. Bedzyk, D. A. Muller, *et al.*, *A Ferroelectric Oxide Made Directly on Silicon*, Science **324**(5925), 367 (2009).
- [38] V. Vaithyanathan, J. Lettieri, W. Tian, A. Sharan, A. Vasudevarao, Y. L. Li, A. Kochhar, H. Ma, J. Levy, P. Zschack, J. C. Woicik, L. Q. Chen, *et al.*, *c-axis oriented epitaxial BaTiO₃ films on (001) Si*, J. App. Phys. **100**(2), 024108 (2006).
- [39] J. Berezovsky, M. H. Mikkelsen, O. Gywat, N. G. Stoltz, L. A. Coldren, and D. D. Awschalom, *Nondestructive Optical Measurements of a Single Electron Spin in a Quantum Dot*, Science **314**(5807), 1916 (2006).
- [40] R. H. Lyddane, R. G. Sachs, and E. Teller, *On the Polar Vibrations of Alkali Halides*, Phys. Rev. **59**(8), 673 (1941).
- [41] N. W. Ashcroft and N. D. Mermin, *Solid State Physics* (Saunders College Publishing, Fort Worth, TX, 1976).
- [42] J. T. Last, *Infrared-Absorption Studies on Barium Titanate and Related Materials*, Phys. Rev. **105**(6), 1740 (1957).

- [43] E. Fatuzzo and W. J. Merz, *Ferroelectricity*, vol. 7 of *Selected Topics in Solid State Physics* (John Wiley & Sons Inc., 1967).
- [44] M. E. Lines and A. M. Glass, *Principles and Applications of Ferroelectrics and Related Materials* (Oxford University Press Inc., New York, NY, 1996).
- [45] R. D. Parks, *Superconductivity* (CRC, 1969), 1st ed.
- [46] K. A. Müller and H. Burkard, *SrTiO₃: An intrinsic quantum paraelectric below 4 K*, Phys. Rev. B **19**(7), 3593 (1979).
- [47] J. H. Haeni, P. Irvin, W. Chang, R. Uecker, P. Reiche, Y. L. Li, S. Choudhury, W. Tian, M. E. Hawley, B. Craigo, A. K. Tagantsev, X. Q. Pan, *et al.*, *Room-temperature ferroelectricity in strained SrTiO₃*, Nature **430**(7001), 758 (2004).
- [48] A. Ohtomo and H. Y. Hwang, *A high-mobility electron gas at the LaAlO₃/SrTiO₃ heterointerface*, Nature **427**(6973), 423 (2004).
- [49] M. Basletic, J. Maurice, C. Carretero, G. Herranz, O. Copie, M. Bibes, E. Jacquet, K. Bouzouane, S. Fusil, and A. Barthelemy, *Mapping the spatial distribution of charge carriers in LaAlO₃/SrTiO₃ heterostructures*, Nature Mater. **7**(8), 621 (2008).
- [50] S. Thiel, G. Hammerl, A. Schmehl, C. W. Schneider, and J. Mannhart, *Tunable Quasi-Two-Dimensional Electron Gases in Oxide Heterostructures*, Science **313**(5795), 1942 (2006).
- [51] C. W. Schneider, S. Thiel, G. Hammerl, C. Richter, and J. Mannhart, *Microolithography of electron gases formed at interfaces in oxide heterostructures*, App. Phys. Lett. **89**(12), 122101 (2006).
- [52] C. Cen, S. Thiel, G. Hammerl, C. W. Schneider, K. E. Andersen, C. S. Hellberg, J. Mannhart, and J. Levy, *Nanoscale control of an interfacial metal-insulator transition at room temperature*, Nature Mater. **7**(4), 298 (2008).
- [53] C. Cen, S. Thiel, J. Mannhart, and J. Levy, *Oxide Nanoelectronics on Demand*, Science **323**(5917), 1026 (2009).
- [54] S. M. Reimann and M. Manninen, *Electronic structure of quantum dots*, Rev. Mod. Phys. **74**(4), 1283 (2002).
- [55] A. P. Alivisatos, *Semiconductor Clusters, Nanocrystals, and Quantum Dots*, Science **271**(5251), 933 (1996).
- [56] L. P. Kouwenhoven, D. G. Austing, and S. Tarucha, *Few-electron quantum dots*, Rep. Prog. Phys. **64**(6), 701 (2001).
- [57] L. P. Kouwenhoven, C. M. Markus, P. L. McEuen, S. Tarucha, R. M. Westervelt, and N. S. Wingreen, *Electron transport in quantum dots*, in *Mesoscopic Electron Transport*, edited by

- L. L. Sohn, L. P. Kouwenhoven, and G. Schön (Kluwer Academic Publishers, 1997), vol. 345 of *E: Applied Sciences*, pp. 105–214.
- [58] J. M. Elzerman, R. Hanson, L. H. W. van Beveren, B. Witkamp, L. M. K. Vandersypen, and L. P. Kouwenhoven, *Single-shot read-out of an individual electron spin in a quantum dot*, Nature **430**(6998), 431 (2004).
- [59] A. Zrenner, L. V. Butov, M. Hagn, G. Abstreiter, G. Bimberg, and G. Weimann, *Quantum dots formed by interface fluctuations in AlAs/GaAs coupled quantum well structures*, Phys. Rev. Lett. **72**(21), 3382 (1994).
- [60] D. Gammon, E. S. Snow, B. V. Shanabrook, D. S. Katzer, and D. Park, *Fine Structure Splitting in the Optical Spectra of Single GaAs Quantum Dots*, Phys. Rev. Lett. **76**(16), 3005 (1996).
- [61] M. Friesen, P. Rugheimer, D. E. Savage, M. G. Lagally, D. W. van der Weide, R. Joynt, and M. A. Eriksson, *Practical design and simulation of silicon-based quantum-dot qubits*, Phys. Rev. B **67**(12), 121301 (2003).
- [62] A. Y. Kitaev, *Fault-tolerant quantum computation by anyons*, arXiv:quant-ph/9707021v1 (1997), Annals Phys. **303**, 2 (2003).
- [63] J. Preskill, *Fault-tolerant quantum computation*, arXiv:quant-ph/9712048v1 (1997).
- [64] B. E. A. Saleh and M. C. Teich, *Fundamentals of Photonics*, Wiley series in pure and applied optics (Wiley, New York, 1991).
- [65] C. Hubert, J. Levy, E. J. Cukauskas, and S. W. Kirchoefer, *Mesosopic Microwave Dispersion in Ferroelectric Thin Films*, Phys. Rev. Lett. **85**, 1998 (2000).
- [66] H. Ma and J. Levy, *GHz Apertureless Near-Field Scanning Optical Microscopy of Ferroelectric Nanodomain Dynamics*, Nano Lett. **6**(3), 341 (2006).
- [67] P. A. Franken, A. E. Hill, C. W. Peters, and G. Weinreich, *Generation of Optical Harmonics*, Phys. Rev. Lett. **7**(4), 118 (1961).
- [68] F. Meier and B. P. Zakharchenya, eds., *Optical Orientation*, vol. 8 of *Modern Problems in Condensed Matter Sciences* (Elsevier Science Ltd, Amsterdam, 1984).
- [69] J. J. Sakuri, *Modern Quantum Mechanics* (Addison Wesley Longman, 1994).
- [70] M. Faraday, *Experimental Researches in Electricity*, Philos. Trans. R. Soc. London **136**, 1 (1846).
- [71] C. Liu and S. D. Bader, *Two-dimensional magnetic phase transition of ultrathin iron films on Pd(100)*, J. App. Phys. **67**(9), 5758 (1990).

- [72] Y. K. Kato, R. C. Myers, A. C. Gossard, and D. D. Awschalom, *Observation of the Spin Hall Effect in Semiconductors*, Science **306**(5703), 1910 (2004).
- [73] S. A. Crooker, *Ultrafast Optical Studies of Coherent Spin Dynamics in Magnetic Quantum Structures*, Ph.D. thesis, University of California, Santa Barbara (1997).
- [74] Y. Ma and J. Levy, *Intrinsic quantum noise in Faraday-rotation measurements of a single-electron spin*, Phys. Rev. A **79**(2), 023830 (2009).
- [75] M. Bayer, O. Stern, P. Hawrylak, S. Fafard, and A. Forchel, *Hidden symmetries in the energy levels of excitonic ‘artificial atoms’*, Nature **405**, 923 (2000).
- [76] R. J. Warburton, C. Schafflein, D. Haft, F. Bickel, A. Lorke, K. Karrai, J. M. Garcia, W. Schoenfeld, and P. M. Petroff, *Optical emission from a charge-tunable quantum ring*, Nature **405**, 926 (2000).
- [77] H. J. Krenner, E. C. Clark, T. Nakaoka, M. Bichler, C. Scheurer, G. Abstreiter, and J. J. Finley, *Optically Probing Spin and Charge Interactions in a Tunable Artificial Molecule*, Phys. Rev. Lett. **97**(7), 076403 (2006).
- [78] E. A. Stinaff, M. Scheibner, A. S. Bracker, I. V. Ponomarev, V. L. Korenev, M. E. Ware, M. F. Doty, T. L. Reinecke, and D. Gammon, *Optical Signatures of Coupled Quantum Dots*, Science **311**(5761), 636 (2006).
- [79] N. V. Joshi, *Photoconductivity: art, science, and technology*, Optical Engineering (Marcell Dekker, Inc, 270 Madison Ave., New York, New York 10016, 1990).
- [80] W. Smith, *Selenium*, Nature **7**, 361 (1873).
- [81] Y. Ahn, J. Dunning, and J. Park, *Scanning Photocurrent Imaging and Electronic Band Studies in Silicon Nanowire Field Effect Transistors*, Nano Lett. **5**(7), 1367 (2005).
- [82] Y. H. Ahn and J. Park, *Efficient visible light detection using individual germanium nanowire field effect transistors*, App. Phys. Lett. **91**(16), 162102 (2007).
- [83] Y. Gu, E. Kwak, J. L. Lensch, J. E. Allen, T. W. Odom, and L. J. Lauhon, *Near-field scanning photocurrent microscopy of a nanowire photodetector*, App. Phys. Lett. **87**(4), 043111 (2005).
- [84] O. G. Vendik, *Ferroelectrics for Microwave Applications* (Soviet Radio, Moscow, 1979).
- [85] M. J. Lancaster, J. Powell, and A. Porch, *Thin-film ferroelectric microwave devices*, Supercond. Sci. Technol. **11**, 1323 (1998).
- [86] C. Hubert, J. Levy, A. C. Carter, W. Chang, S. W. Kiechoefer, J. S. Horwitz, and D. B. Chrisey, *Confocal scanning optical microscopy of $Ba_xSr_{1-x}TiO_3$ thin films*, App. Phys. Lett. **71**, 3353 (1997).

- [87] A. F. Devonshire, *Theory of ferroelectrics*, Adv. Phys. **3**(10), 85 (1954).
- [88] H. Uwe and T. Sakudo, *Stress-induced ferroelectricity and soft phonon modes in SrTiO₃*, Phys. Rev. B **13**, 271 (1976).
- [89] N. A. Pertsev, A. G. Zembilgotov, and A. K. Tagantsev, *Effect of Mechanical Boundary Conditions on Phase Diagrams of Epitaxial Ferroelectric Thin Films*, Phys. Rev. Lett. **80**, 1988 (1998).
- [90] K. Abe, N. Yanase, K. Sano, M. Izuha, N. Fukushima, and T. Kawakubo, *Modification of ferroelectricity in heteroepitaxial (Ba,Sr)TiO₃ films for non-volatile memory applications*, Integr. Ferroelectr. **21**, 197 (1998).
- [91] S. K. Streiffer, J. A. Eastman, D. D. Fong, C. Thompson, A. Munkholm, M. V. R. Murty, O. Auciello, G. R. Bai, and G. B. Stephenson, *Observation of Nanoscale 180° Stripe Domains in Ferroelectric PbTiO₃ Thin Films*, Phys. Rev. Lett. **89**, 067601 (2002).
- [92] R. S. Beach, J. A. Borchers, A. Matheny, R. W. Erwin, M. B. Salamon, B. Everitt, K. Pettit, J. J. Rhyne, and C. P. Flynn, *Enhanced Curie temperatures and magnetoelastic domains in Dy/Lu superlattices and films*, Phys. Rev. Lett. **70**, 3502 (1993).
- [93] Q. Gan, R. A. Rao, C. B. Eom, J. L. Garrett, and M. Lee, *Direct measurement of strain effects on magnetic and electrical properties of epitaxial SrRuO₃ thin films*, App. Phys. Lett. **72**, 978 (1998).
- [94] J. M. Lock, *Penetration of Magnetic Fields into Superconductors III. Measurements on Thin Films of Tin, Lead and Indium*, Proc. R. Soc. A **208**, 391 (1951).
- [95] H. Sato and M. Naito, *Increase in the superconducting transition temperature by anisotropic strain effect in (001) La_{1.85}Sr_{0.15}CuO₄ thin films on LaSrAlO₄ substrates*, Physica C **274**, 221 (1997).
- [96] I. Bozovic, G. Logvenov, I. Belca, B. Narimbetov, and I. Sveklo, *Epitaxial Strain and Superconductivity in La_{2-x}Sr_xCuO₄ Thin Films*, Phys. Rev. Lett. **89**, 107001 (2002).
- [97] J. G. Bednorz and K. A. Müller, *Sr_{1-x}Ca_xTiO₃: An XY Quantum Ferroelectric with Transition to Randomness*, Phys. Rev. Lett. **52**, 2289 (1984).
- [98] A. Chen, Z. Yu, J. Scott, A. Loidl, R. Guo, A. S. Bhalla, and L. E. Cross, *Dielectric polarization processes in Bi:SrTiO₃*, J. Phys. Chem. Solids **61**, 191 (2000).
- [99] M. Itoh, R. Wang, Y. Inaguma, T. Yamaguchi, Y.-J. Shan, and T. Nakamura, *Ferroelectricity Induced by Oxygen Isotope Exchange in Strontium Titanate Perovskite*, Phys. Rev. Lett. **82**, 3540 (1999).
- [100] N. A. Pertsev, A. K. Tagantsev, and N. Setter, *Phase transitions and strain-induced ferroelectricity in SrTiO₃ epitaxial thin films*, Phys. Rev. B **61**, R825 (2000).

- [101] K.-H. Hellwege and A. M. Hellwege, eds., *Landolt-Börnstein: Numerical Data and Functional Relationships in Science and Technology New Series, Group III*, vol. 16a (Springer, Berlin, 1981).
- [102] K.-H. Hellwege and A. M. Hellwege, eds., *Landolt-Börnstein: Numerical Data and Functional Relationships in Science and Technology New Series, Group III*, vol. 11 (Springer, Berlin, 1979).
- [103] C. L. Canedy, H. Li, S. P. Alpay, L. Salamanca-Riba, A. L. Roytburd, and R. Ramesh, *Dielectric properties in heteroepitaxial $Ba_{0.6}Sr_{0.4}TiO_3$ thin films: Effect of internal stresses and dislocation-type defects*, *App. Phys. Lett.* **77**, 1695 (2000).
- [104] K.-H. Hellwege and A. M. Hellwege, eds., *Landolt-Börnstein: Numerical Data and Functional Relationships in Science and Technology New Series, Group III*, vol. 7b (Springer, Berlin, 1976).
- [105] K.-H. Hellwege and A. M. Hellwege, eds., *Landolt-Börnstein: Numerical Data and Functional Relationships in Science and Technology New Series, Group III*, vol. 7e (Springer, Berlin, 1976).
- [106] *JCPDS Powder Diffraction File: Sets 27 to 28 72* (1986).
- [107] B. C. Chakoumakos, D. G. Schlom, M. Urbanik, and J. Luine, *Thermal expansion of $LaAlO_3$ and $(La,Sr)(Al,Ta)O_3$, substrate materials for superconducting thin-film device applications*, *J. App. Phys.* **83**, 1979 (1998).
- [108] S. Tidrow, A. Tauber, W. Wilber, R. Lareau, C. Brandle, G. Berkstresser, A. V. Graitis, D. Potrepka, J. Budnick, and J. A. W. Wu, *New substrates for HTSC microwave devices*, *IEEE Trans. Appl. Supercond.* **7**, 1766 (1997).
- [109] S. Gevorgian, T. Martinsson, P. Linner, and E. Kollberg, *CAD models for multilayered substrate interdigital capacitors*, *IEEE Trans. Microwave Theory Tech.* **44**, 896 (1996).
- [110] J. Haeni, C. Theis, and D. Schlom, *RHEED Intensity Oscillations for the Stoichiometric Growth of $SrTiO_3$ Thin Films by Reactive Molecular Beam Epitaxy*, *J. Electroceram.* **4**, 385 (2000).
- [111] H. M. Christen, L. A. Knauss, and K. S. Harshavardhan, *Field-dependent dielectric permittivity of paraelectric superlattice structures*, *Mat. Sci. Eng. B* **56**, 200 (1998).
- [112] V. Lemanov, A. Sotnikov, E. Smirnova, and M. Weihnacht, *Giant dielectric relaxation in $SrTiO_3$ - $SrMg_{1/3}Nb_{2/3}O_3$ and $SrTiO_3$ - $SrSc_{1/2}Ta_{1/2}O_3$ solid solutions*, *Fiz. Tverd. Tela (St Petersburg)* **44**, 1948 (2002).
- [113] C. Hubert and J. Levy, *New optical probe of GHz polarization dynamics in ferroelectric thin films*, *Rev. Sci. Instrum.* **70**, 3684 (1999).

- [114] P. Irvin, J. Levy, J. H. Haeni, and D. G. Schlom, *Localized microwave resonances in strained SrTiO₃ thin films*, App. Phys. Lett. **88**(4), 042902 (2006).
- [115] G. Arlt, U. Böttger, and S. Witte, *Dielectric dispersion of ferroelectric ceramics and single crystals at microwave frequencies*, Ann. Phys. (Leipzig) **506**, 578 (1994).
- [116] D. Viehland, S. J. Jang, L. E. Cross, and M. Wuttig, *Deviation from Curie-Weiss behavior in relaxor ferroelectrics*, Phys. Rev. B **46**, 8003 (1992).
- [117] S. Wakimoto, C. Stock, Z.-G. Ye, W. Chen, P. M. Gehring, and G. Shirane, *Mode coupling and polar nanoregions in the relaxor ferroelectric Pb(Mg_{1/3}Nb_{2/3})O₃*, Phys. Rev. B **66**, 224102 (2002).
- [118] M. P. McNeal, S.-J. Jang, and R. E. Newnham, *The effect of grain and particle size on the microwave properties of barium titanate (BaTiO₃)*, J. App. Phys. **83**, 3288 (1998).
- [119] Y. Drezner and S. Berger, *Nanoferroelectric domains in ultrathin BaTiO₃ films*, J. App. Phys. **94**, 6774 (2003).
- [120] R. Pattnaik and J. Toulouse, *New Dielectric Resonances in Mesoscopic Ferroelectrics*, Phys. Rev. Lett. **79**, 4677 (1997).
- [121] S. Dunn, *Strain behavior of thin film PbZr_{0.3}Ti_{0.7}O₃ (30/70) examined through piezoforce microscopy*, J. App. Phys. **94**, 5964 (2003).
- [122] A. Vorobiev, P. Rundqvist, K. Khamchane, and S. Gevorgian, *Microwave loss mechanisms in Ba_{0.25}Sr_{0.75}TiO₃ thin film varactors*, J. App. Phys. **96**, 4642 (2004).
- [123] C. M. Carlson, T. V. Rivkin, P. A. Parilla, J. D. Perkins, D. S. Ginley, A. B. Kozyrev, V. N. Oshadchy, and A. S. Pavlov, *Large dielectric constant ($\epsilon/\epsilon_0 > 6000$) Ba_{0.4}Sr_{0.6}TiO₃ thin films for high-performance microwave phase shifters*, App. Phys. Lett. **76**, 1920 (2000).
- [124] C. Mueller, R. Romanofsky, and F. Miranda, *Ferroelectric thin film and broadband satellite systems*, IEEE Potentials **20**(2), 36 (2001).
- [125] A. T. Findikoglu, Q. X. Jia, X. D. Wu, G. J. Chen, T. Venkatesan, and D. W. Reagor, *Tunable and adaptive bandpass filter using a nonlinear dielectric thin film of SrTiO₃*, App. Phys. Lett. **68**, 1651 (1996).
- [126] W. Chang, S. W. Kirchoefer, J. M. Pond, J. A. Bellotti, S. B. Qadri, J. H. Haeni, and D. G. Schlom, *Room-temperature tunable microwave properties of strained SrTiO₃ films*, J. App. Phys. **96**, 6629 (2004).
- [127] G. Arlt, U. Bottger, and S. Witte, *Emission of GHz shear waves by ferroelastic domain walls in ferroelectrics*, App. Phys. Lett. **63**, 602 (1993).
- [128] M. Biegalski, D. Schlom, S. Trolier-MckInstry, S. K. Streiffer, W. Chang, S. W. Kirchoefer, R. Uecker, and P. Reiche (unpublished).

- [129] P. Irvin, J. Levy, R. Guo, and A. Bhalla, *Three-dimensional polarization imaging of (Ba,Sr)TiO₃:MgO composites*, App. Phys. Lett. **86**(4), 042903 (2005).
- [130] L. A. Knauss, J. M. Pond, J. S. Horwitz, D. B. Chrisey, C. H. Mueller, and R. Treece, *The effect of annealing on the structure and dielectric properties of Ba_xSr_{1-x}TiO₃ ferroelectric thin films*, App. Phys. Lett. **69**, 25 (1996).
- [131] J. Im, O. Auciello, P. K. Baumann, S. K. Streiffer, D. Y. Kaufman, and A. R. Krauss, *Composition-control of magnetron-sputter-deposited (Ba_xSr_{1-x})Ti_{1+y}O_{3+z} thin films for voltage tunable devices*, App. Phys. Lett. **76**, 625 (2000).
- [132] L. C. Sengupta, J. Synowczynski, and L. H. Chiu, *Investigation of the effect of particle size on the optical and electronic properties of Ba_{1-x}Sr_xTiO₃ composite ceramics*, Integr. Ferroelectr. **17**, 287 (1997).
- [133] D. Garcia, R. Guo, and A. S. Bhalla, *Growth and properties of Ba_{0.9}Sr_{0.1}TiO₃ single crystal fibers*, Mater. Lett. **42**, 136 (2000).
- [134] W. J. Merz, *Domain Properties in BaTiO₃*, Phys. Rev. **88**, 421 (1952).
- [135] R. Guo, A. S. Bhalla, and L. E. Cross, *Ba(Mg_{1/3}Ta_{2/3})O₃ single crystal fiber grown by the laser heated pedestal growth technique*, J. App. Phys. **75**, 4704 (1994).
- [136] A. S. Bhalla, D. Garcia, and R. Guo (unpublished).
- [137] P. Franken and J. Ward, *Optical Harmonics and Nonlinear Phenomena*, Rev. Mod. Phys. **35**, 23 (1963).
- [138] P. J. Campagnola, M. de Wei, A. Lewis, and L. M. Loew, *High-Resolution Nonlinear Optical Imaging of Live Cells by Second Harmonic Generation*, Biophys. J. **77**, 3341 (1999).
- [139] B. Vohnsen, S. I. Bozhevolnyi, K. Pedersen, J. Erland, J. R. Jensen, and J. M. Hvam, *Second-harmonic scanning optical microscopy of semiconductor quantum dots*, Opt. Commun. **189**, 305 (2001).
- [140] S. I. Bozhevolnyi, J. M. Hvam, K. Pedersen, F. Laurell, H. Karlsson, T. Skettrup, and M. Belmonte, *Second-harmonic imaging of ferroelectric domain walls*, App. Phys. Lett. **73**, 1814 (1998).
- [141] Y. Uesu, S. Kurimura, and Y. Yamamoto, *Optical second harmonic images of 90° domain structure in BaTiO₃ and periodically inverted antiparallel domains in LiTaO₃*, App. Phys. Lett. **66**, 2165 (1995).
- [142] E. D. Mishina, T. V. Misuryaev, N. E. Sherstyuk, V. V. Lemanov, A. I. Morozov, A. S. Sigov, and T. Rasing, *Observation of a Near-Surface Structural Phase Transition in SrTiO₃ by Optical Second Harmonic Generation*, Phys. Rev. Lett. **85**, 3664 (2000).

- [143] R. Gauderon, P. B. Lukins, and C. J. R. Sheppard, *Three-dimensional second-harmonic generation imaging with femtosecond laser pulses*, Opt. Lett. **23**, 1209 (1998).
- [144] M. Abramoff and M. Viergever, *Computation and visualization of three-dimensional soft tissue motion in the orbit*, IEEE Trans. Med. Imag. **21**, 296 (2002).
- [145] P. Irvin, P. S. Fodor, and J. Levy, *Gigahertz optical spin transceiver*, Opt. Express **15**(18), 11756 (2007).
- [146] S. A. Wolf, D. D. Awschalom, R. A. Buhrman, J. M. Daughton, S. von Molnár, M. L. Roukes, A. Y. Chtchelkanova, and D. M. Treger, *Spintronics: A Spin-Based Electronics Vision for the Future*, Science **294**, 1488 (2001).
- [147] S. A. Crooker and D. L. Smith, *Imaging Spin Flows in Semiconductors Subject to Electric, Magnetic, and Strain Fields*, Phys. Rev. Lett. **94**, 236601 (2005).
- [148] R. J. Epstein, D. T. Fuchs, W. V. Schoenfeld, P. M. Petroff, and D. D. Awschalom, *Hanle effect measurements of spin lifetimes in InAs self-assembled quantum dots*, App. Phys. Lett. **78**, 733 (2001).
- [149] X. Lou, C. Adelman, S. A. Crooker, E. S. Garlid, J. Zhang, K. S. M. Reddy, S. D. Flexner, C. J. Palmstrom, and P. A. Crowell, *Electrical detection of spin transport in lateral ferromagnet-semiconductor devices*, Nature Phys. **3**, 197 (2007).
- [150] M. Oestreich, M. Romer, R. J. Haug, and D. Hagele, *Spin Noise Spectroscopy in GaAs*, Phys. Rev. Lett. **95**, 216603 (2005).
- [151] J. M. Kikkawa and D. D. Awschalom, *Resonant Spin Amplification in n-Type GaAs*, Phys. Rev. Lett. **80**, 4313 (1998).
- [152] F. T. Charnock, R. Lopusnik, and T. J. Silva, *Pump-probe Faraday rotation magnetometer using two diode lasers*, Rev. Sci. Instrum. **76**, 056105 (2005).
- [153] D. Magde, E. Elson, and W. W. Webb, *Thermodynamic Fluctuations in a Reacting System—Measurement by Fluorescence Correlation Spectroscopy*, Phys. Rev. Lett. **29**(11), 705 (1972).
- [154] R. J. Kneisler, F. E. Lytle, G. J. Fiechtner, Y. Jiang, G. B. King, and N. M. Laurendeau, *Asynchronous optical sampling: a new combustion diagnostic for potential use in turbulent, high-pressure flames*, Opt. Lett. **14**(5), 260 (1989).
- [155] J. J. Baumberg, S. A. Crooker, D. D. Awschalom, N. Samarth, H. Luo, and J. K. Furdyna, *Ultrafast Faraday spectroscopy in magnetic semiconductor quantum structures*, Phys. Rev. B **50**, 7689 (1994).
- [156] M. H. Mikkelsen, J. Berezovsky, N. G. Stoltz, L. A. Coldren, and D. D. Awschalom, *Optically detected coherent spin dynamics of a single electron in a quantum dot*, Nature Phys. **3**, 770 (2007).

- [157] J. Berezovsky, *Optical control and detection of spin coherence in semiconductor nanostructures*, Ph.D. thesis, University of California, Santa Barbara (2007).
- [158] G. Medeiros-Ribeiro, M. V. B. Pinheiro, V. L. Pimentel, and E. Marega, *Spin splitting of the electron ground states of InAs quantum dots*, App. Phys. Lett. **80**(22), 4229 (2002).
- [159] G. Medeiros-Ribeiro, E. Ribeiro, and H. Westfahl Jr., *g-factor engineering and control in self-assembled quantum dots*, Appl. Phys. A: Mater. **77**(6), 725 (2003).
- [160] P. S. Fodor, S. Rothenberger, and J. Jevy, *320-channel dual phase lock-in optical spectrometer*, Rev. Sci. Instrum. **76**(1), 013103 (2005).
- [161] G. Salis and M. Moser, *Faraday-rotation spectrum of electron spins in microcavity-embedded GaAs quantum wells*, Phys. Rev. B **72**(11), 115325 (2005).
- [162] Y. Q. Li, D. W. Steuerman, J. Berezovsky, D. S. Seferos, G. C. Bazan, and D. D. Awschalom, *Cavity enhanced Faraday rotation of semiconductor quantum dots*, App. Phys. Lett. **88**(19), 193126 (2006).
- [163] D. I. Lubyshev, P. P. González-Borrero, J. Marega, E. Petitprez, J. L. Scala, and P. Basmaji, *Exciton localization and temperature stability in self-organized InAs quantum dots*, App. Phys. Lett. **68**(2), 205 (1996).
- [164] D. P. Popescu, P. G. Eliseev, A. Stintz, and K. J. Malloy, *Temperature dependence of the photoluminescence emission from InAs quantum dots in a strained Ga_{0.85}In_{0.15}As quantum well*, Semicond. Sci. Technol. **19**(1), 33 (2004).
- [165] S. Malik, C. Roberts, R. Murray, and M. Pate, *Tuning self-assembled InAs quantum dots by rapid thermal annealing*, App. Phys. Lett. **71**(14), 1987 (1997).
- [166] S. J. Xu, X. C. Wang, S. J. Chua, C. H. Wang, W. J. Fan, J. Jiang, and X. G. Xie, *Effects of rapid thermal annealing on structure and luminescence of self-assembled InAs/GaAs quantum dots*, App. Phys. Lett. **72**(25), 3335 (1998).
- [167] T. M. Hsu, Y. S. Lan, W. Chang, N. T. Yeh, and J. Chyi, *Tuning the energy levels of self-assembled InAs quantum dots by rapid thermal annealing*, App. Phys. Lett. **76**(6), 691 (2000).
- [168] J. Berezovsky, M. H. Mikkelsen, N. G. Stoltz, L. A. Coldren, and D. D. Awschalom, *Picosecond Coherent Optical Manipulation of a Single Electron Spin in a Quantum Dot*, Science **320**(5874), 349 (2008).
- [169] B. Alén, F. Bickel, K. Karrai, R. J. Warburton, and P. M. Petroff, *Stark-shift modulation absorption spectroscopy of single quantum dots*, App. Phys. Lett. **83**, 2235 (2003).
- [170] S. M. Mansfield and G. S. Kino, *Solid immersion microscope*, App. Phys. Lett. **57**, 2615 (1990).

- [171] S. B. Ippolito, B. B. Goldberg, and M. S. Ünlü, *High spatial resolution subsurface microscopy*, App. Phys. Lett. **78**, 4071 (2001).
- [172] A. Vamivakas, M. Atatüre, J. Dreiser, S. Yilmaz, A. Badolato, A. Swan, B. Goldberg, A. Imamoglu, and M. Ünlü, *Strong Extinction of a Far-Field Laser Beam by a Single Quantum Dot*, Nano Lett. **7**, 2892 (2007).
- [173] X. Duan, Y. Huang, Y. Cui, J. Wang, and C. M. Lieber, *Indium phosphide nanowires as building blocks for nanoscale electronic and optoelectronic devices*, Nature **409**(6816), 66 (2001).
- [174] J. Wang, M. S. Gudiksen, X. Duan, Y. Cui, and C. M. Lieber, *Highly Polarized Photoluminescence and Photodetection from Single Indium Phosphide Nanowires*, Science **293**(5534), 1455 (2001).
- [175] Y. Huang, X. Duan, and C. Lieber, *Nanowires for Integrated Multicolor Nanophotonics*, Small **1**(1), 142 (2005).
- [176] D. J. Sirbulu, M. Law, H. Yan, and P. Yang, *Semiconductor Nanowires for Subwavelength Photonics Integration*, J. Phys. Chem. B **109**(32), 15190 (2005).
- [177] R. Agarwal and C. Lieber, *Semiconductor nanowires: optics and optoelectronics*, Appl. Phys. A: Mater. **85**(3), 209 (2006).
- [178] O. Hayden, R. Agarwal, and C. M. Lieber, *Nanoscale avalanche photodiodes for highly sensitive and spatially resolved photon detection*, Nature Mater. **5**(5), 352 (2006).
- [179] M. Freitag, J. C. Tsang, J. Kirtley, A. Carlsen, J. Chen, A. Troeman, H. Hilgenkamp, and P. Avouris, *Electrically Excited, Localized Infrared Emission from Single Carbon Nanotubes*, Nano Lett. **6**(7), 1425 (2006).
- [180] B. Tian, X. Zheng, T. J. Kempa, Y. Fang, N. Yu, G. Yu, J. Huang, and C. M. Lieber, *Coaxial silicon nanowires as solar cells and nanoelectronic power sources*, Nature **449**(7164), 885 (2007).
- [181] L. Jiao, X. Xian, Z. Wu, J. Zhang, and Z. Liu, *Selective Positioning and Integration of Individual Single-Walled Carbon Nanotubes*, Nano Lett. **9**(1), 205 (2009).
- [182] Z. Fan, J. C. Ho, Z. A. Jacobson, H. Razavi, and A. Javey, *Large-scale, heterogeneous integration of nanowire arrays for image sensor circuitry*, P. Nat. Acad. Sci. USA **105**(32), 11066 (2008).
- [183] D. F. Bogorin, C. Cen, C. B. Eom, and J. Levy (unpublished).
- [184] M. Hegg and L. Y. Lin, *Near-field photodetection with high spatial resolution by nanocrystal quantum dots*, Opt. Express **15**(25), 17163 (2007).

- [185] K. van Benthem, C. Elsasser, and R. H. French, *Bulk electronic structure of SrTiO₃: Experiment and theory*, J. App. Phys. **90**(12), 6156 (2001).
- [186] L. Grabner, *Photoluminescence in SrTiO₃*, Phys. Rev. **177**(3), 1315 (1969).
- [187] H. Katsu, H. Tanaka, and T. Kawai, *Anomalous Photoconductivity in SrTiO₃*, Jpn. J. Appl. Phys. **39**, 2657 (2000).
- [188] T. Feng, *Anomalous photoelectronic processes in SrTiO₃*, Phys. Rev. B **25**(2), 627 (1982).
- [189] F. Rossella, P. Galinetto, G. Samoggia, V. Trepakov, and L. Jastrabik, *Photoconductivity and the structural phase transition in SrTiO₃*, Solid State Communications **141**, 95 (2007).
- [190] K. Peters (private communication).
- [191] D. Kan, T. Terashima, R. Kanda, A. Masuno, K. Tanaka, S. Chu, H. Kan, A. Ishizumi, Y. Kanemitsu, Y. Shimakawa, and M. Takano, *Blue-light emission at room temperature from Ar⁺-irradiated SrTiO₃*, Nat Mater **4**(11), 816 (2005).
- [192] D. Kan, R. Kanda, Y. Kanemitsu, Y. Shimakawa, M. Takano, T. Terashima, and A. Ishizumi, *Blue luminescence from electron-doped SrTiO₃*, App. Phys. Lett. **88**(19), 191916 (2006).
- [193] T. Hasegawa and K. Tanaka, *Photo-induced polaron states in strontium titanate*, J. Lumin. **94-95**, 15 (2001).
- [194] H. Okamura, M. Matsubara, K. Tanaka, K. Fukui, M. Terakami, H. Nakagawa, Y. Ikemoto, T. Moriwaki, H. Kimura, and T. Nanba, *Photogenerated Carriers in SrTiO₃ Probed by Mid-Infrared Absorption*, J. Phys. Soc. Jpn. **75**, 023703 (2006).
- [195] R. Leonelli and J. L. Brebner, *Time-resolved spectroscopy of the visible emission band in strontium titanate*, Phys. Rev. B **33**(12), 8649 (1986).
- [196] K. Shibuya, T. Ohnishi, T. Sato, and M. Lippmaa, *Metal-insulator transition in SrTiO₃ induced by field effect*, J. App. Phys. **102**(8), 083713 (2007).
- [197] G. Cheng, C. Cen, M. Warusawithana, D. Schlom, and J. Levy, *Ferroelectric field effect transistors on silicon* (unpublished).
- [198] P. S. Fodor, O. Guise, J. Yates, and J. Levy (unpublished).
- [199] J.-W. Park, D. F. Bogorin, C. Cen, C. T. Nelson, Y. Zhang, C. M. Folkman, D. Felker, M. Rzechowski, X. Pan, J. Levy, and C.-B. Eom, *Two-dimensional electron gas at LaAlO₃/SrTiO₃ heterointerfaces grown on silicon* (unpublished).
- [200] *ImageJ*, <http://rsb.info.nih.gov/ij/>.